

UNIVERSITY OF IOANNINA

SCHOOL OF NATURAL SCIENCES

PHYSICS DEPARTMENT

PhD Thesis

Study of the ${}^6\text{Li}+p$ system in inverse
kinematics with the MAGNEX
spectrometer

Author:

Vasileios Soukeras

Supervisor:

Prof. Athina Pakou



May 2017

Three-members committee:

1. **Athina Pakou** (Supervisor)

Emeritus Professor, Physics Department, University of Ioannina

2. **Nicolas Alamanos**

Professor, Deputy Director of IRFU, Research Director at CEA Saclay

3. **Efstathios Stiliaris**

Associate Professor, Physics Department, University of Athens

Review committee:

1. **Athina Pakou** - Emeritus Professor, Physics Department, University of Ioannina

2. **Nicolas Alamanos** - Professor, Deputy Director of IRFU, Research Director at CEA Saclay

3. **Efstathios Stiliaris** - Associate Professor, Physics Department, University of Athens

4. **Krzysztof Rusek** - Professor, Director of HIL, University of Warsaw

5. **Francesco Cappuzzello** - Professor, University of Catania and INFN-LNS

6. **Xenofon Aslanoglou** - Associate Professor, Physics Department, University of Ioannina

7. **George Souliotis** - Associate Professor, Chemistry Department, University of Athens

ΠΡΑΚΤΙΚΟ ΠΑΡΟΥΣΙΑΣΗΣ, ΕΞΕΤΑΣΗΣ ΚΑΙ ΑΞΙΟΛΟΓΗΣΗΣ ΔΙΔΑΚΤΟΡΙΚΗΣ ΔΙΑΤΡΙΒΗΣ

Σήμερα Πέμπτη 4 Μαΐου 2017, ώρα 10:30, στην αίθουσα σεμιναρίων του Τμήματος Φυσικής του Πανεπιστημίου Ιωαννίνων, πραγματοποιήθηκε σύμφωνα με το άρθρο 12, παρ. 5 του Ν.2083/92 η διαδικασία της δημόσιας παρουσίασης, εξέτασης και αξιολόγησης της διδακτορικής διατριβής του υποψηφίου διδάκτορα κ. Βασιλείου Σούκερα

Την Επταμελή Εξεταστική Επιτροπή, που συγκροτήθηκε με απόφαση της Γενικής Συνέλευσης Ειδικής Σύμβασης του Τμήματος Φυσικής (συν. 477/10-2-2017) αποτελούν τα κάτωθι μέλη :

1. Αθηνά Πάκου-Ομότιμη Καθηγήτρια - Τμήμα Φυσικής, Πανεπιστήμιο Ιωαννίνων (Επιβλέπουσα Καθηγήτρια)
2. Nicolas Alamanos-Professor-Deputy Director of IRFU-Research Director at CEA -SACLAY-France
3. Ευστάθιος Στυλιάρης-Αναπληρωτής Καθηγητής-Τμήμα Φυσικής -ΕΚΠΙΑ
4. Krzysztof Rusek -Professor- Director of HIL, University of Warsaw- Poland
5. Francesco Cappuzzello-Professor-University of Catania and INFN LNS-Italy
6. Ξενοφών Ασλάνογλου- Αναπληρωτής Καθηγητής- Τμήμα Φυσικής- Πανεπιστήμιο Ιωαννίνων
7. Γεώργιος Σουλιώτης-Αναπληρωτής Καθηγητής - Τμήμα Χημείας - ΕΚΠΙΑ

Παρόντα ήταν και τα 7 μέλη της εξεταστικής επιτροπής. Το θέμα της διδακτορικής διατριβής που εκπόνησε ο κ. Σούκερας και παρουσίασε σήμερα είναι : ‘Μελέτη του συστήματος ${}^6\text{Li} + p$ σε αντίστροφη κινηματική με το φασματομέτρο MAGNEX ‘

Ο Υποψήφιος αφού παρουσίασε διεξοδικά το θέμα, απάντησε σε ερωτήσεις των μελών της επιτροπής και του ακροατηρίου. Στη συνέχεια η επιτροπή αποσύρθηκε και μετά από εκτεταμένη συζήτηση στην οποία εκφράστηκαν από όλα τα μέλη εξαιρετικοί έπαινοι τόσο για τη διατριβή όσο και για τον υποψήφιο κατέληξε στα ακόλουθα

1. Το περιεχόμενο της διατριβής είναι πρωτότυπο, υψηλής ποιότητας και αποτελεί ουσιαστική συμβολή στην επιστήμη. Από την εργασία αυτή έχουν προκύψει δύο δημοσιευμένες εργασίες σε έγκριτα περιοδικά που έγιναν από τον υποψήφιο, ενώ υπήρξε ουσιαστική συμμετοχή του και σε άλλες δώδεκα δημοσιευμένες εργασίες.
2. Η παρουσίαση και ανάπτυξη του θέματος της διατριβής από τον υποψήφιο και οι απαντήσεις στις ερωτήσεις που του τέθηκαν έδειξαν την ωριμότητα του υποψηφίου και την εξαιρετική κατάρτιση του τόσο στα σχετικά πειραματικά θέματα όσο και στη θεωρία.

Με βάση τα ανωτέρω η επιτροπή εγκρίνει ομόφωνα την εργασία και εισηγείται θερμά και ανεπιφύλακτα την απονομή Διδακτορικού Διπλώματος στον κ. **Βασίλειο Σούκερα** με βαθμό **Άριστα**

Το πρακτικό αυτό συντάχθηκε την ίδια μέρα και υπογράφεται από τα μέλη της Εξεταστικής Επιτροπής.

1. Αθηνά Πάκου (Επιβλέπουσα)

2. Nicolas Alamanos

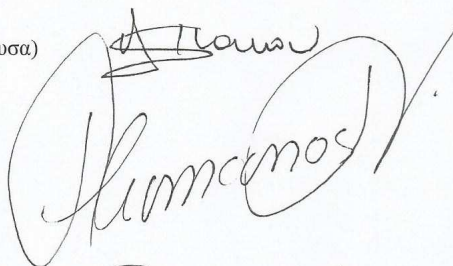
3. Ευστάθιος Στυλιάρης

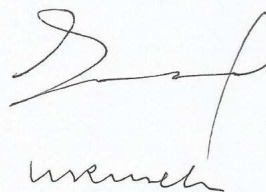
4. Krzysztof Rusek

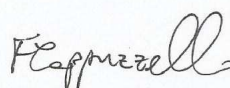
5. Francesco Cappuzzello

6. Ξενοφών Ασλάνογλου

7. Γεώργιος Σουλιάτης











Στους γονείς μου
Σπύρο και Κατερίνα

To my parents
Spiros and Katerina

Contents

Acknowledgements	1
Abstract	3
Introduction	7
1 Theory	11
1.1 Elastic Scattering	11
1.1.1 Scattering Theory	12
1.1.2 Optical Potential	14
1.2 Breakup process	18
1.3 Continuum Discretized Coupled Channel (CDCC) calculations	20
2 Experimental Details	23
2.1 Experimental setup and procedure	23
2.2 The MAGNEX Spectrometer	26
2.2.1 The Focal Plane Detector	29
2.2.2 Trajectory Reconstruction	33
2.3 The Silicon detector at 5 degrees	37
2.4 Electronics of the experiment	39
2.5 Target details	39

3	Data Reduction	43
3.1	Calibration procedure	43
3.1.1	MAGNEX calibration	43
3.1.2	Silicon detector calibration	44
3.2	Particle identification	46
3.2.1	Identification of the elastic channel	47
3.2.2	Identification of the breakup channel	50
3.3	Determination of the elastic scattering cross section	59
3.4	Determination of the breakup cross section	65
3.4.1	Determination of the efficiency	66
3.4.2	Deduction of the breakup angular distributions in the center of mass frame	67
4	Theoretical analysis	71
4.1	JLM Calculations	71
4.2	Continuum Discretized Coupled Channel Calculations (CDCC)	74
4.2.1	Elastic Scattering	75
4.2.2	Breakup	83
5	Conclusions	89
	References	93
A	Determination of the effective beam energy	107
B	Error calculation	109
B.1	Error calculation for elastic scattering data	109
B.2	Error calculation for breakup data	110
C	Computer codes	113
C.1	Routines in C language: C.M. to Lab converter	113

C.2	Routines in C language: Lab to C.M. converter	121
D	Tabulated cross sections	131
D.1	Elastic scattering data	131
D.2	Breakup data	136

Acknowledgements

At this point, I would like to thank all of those who have supported and assisted me during my PhD studies.

First of all, I would like to express my deepest appreciation to my supervisor Professor Athina Pakou, for her guidance and help throughout my studies, for proposing the subject of my PhD thesis, introducing me to all the appropriate experimental and theoretical techniques in the Nuclear Physics field and for supporting my efforts during my studies. She was available many hours per day in order to solve together all the emerging problems and she generously provided to me all the appropriate skills and competences useful for this demanding scientific field. I'm really proud for being her student.

Also, I would like to extend my sincere thanks to the other members of the advisory committee, Professor Nicolas Alamanos and Associate Professor Efstathios Stiliaris for their generous assistance and advices.

I would like also to express my warm appreciation to the MAGNEX group but especially to Prof. Francesco Cappuzzello, Dr. Manuela Cavallaro and Dr. Diana Carbone to introduce me in the technique of measurements with MAGNEX, collect data with the spectrometer and the reconstruction of the data as well as their support with analysis problems.

I would like to extend my sincere and warm thanks to Professor Krzysztof Rusek and Associate Professor Nicholas Keeley for the theoretical support but especially, for introducing me to the impressive world of the CDCC calculations which is a powerful theoretical tool for the present kind of analysis. Working with them has been a very profitable experience. Also, I would like to express my appreciation to Professor Krzysztof Rusek for the generous hospitality at the Heavy Ion Laboratory during my staying in Warsaw.

Also, I would like to express my sincere thanks to all the participants from INFN-LNS, Catania University, INFN-Catania, Huelva University, Mexico University, Padova University, INFN-Padova and INFN-Napoli for their unreserved assistance during the performed experi-

ment, and especially to Assoc. Prof. Efstathios Stiliaris and his group for their help with the simulation code GATE.

I would like to express my appreciation to Prof. F. Cappuzzello for introduced me to the MAGNEX analysis as well as to analysis with neutron spectra acquired with the EDEN detectors, during an ERASMUS training period. Working with him and his group helped me to develop further my skills.

In addition, I would like to thank my friends and fellow workers Dr. Onoufrios (Akis) Sgouros, Dr. Konstantina Zerva and Ms. Chrysoula Betsou for their friendly and collaborative spirit. Especially, I would like to point out the importance of the fruitful discussions with my supervisor Prof. Pakou as well as my fellow worker Akis not only in this work but also in all experiments and works we have participated.

Furthermore, I would like to thank the seven members of the review committee for reading extensively the final manuscript and for their useful comments they made.

Last but not least, I would like to thank my beloved parents Spiros and Katerina for their love, encouragement and unreserved support during my studies. I dedicate this work to them.

Abstract

This work refers to the study of the ${}^6\text{Li}+\text{p}$ system in inverse kinematics with the MAGNEX spectrometer. The relevant experiment was visualized at the MAGNEX facility of Istituto Nazionale di Fisica Nucleare - Laboratori Nazionali del Sud (INFN - LNS), in Catania, Italy. Beams of ${}^6\text{Li}^{3+}$ were accelerated by the Tandem accelerator at the energies of 16, 20, 25 and 29 MeV and impinged on a CH_2 target as well as on a ${}^{12}\text{C}$ target for estimating the carbon background. The experiment includes three different parts: the elastic scattering measurement, the breakup measurement, and the measurement of the reaction $\text{p}({}^6\text{Li}, {}^3\text{He}){}^4\text{He}$. The first two are included in the present thesis, while the last performed with a DSSSD module, was the subject of an M.Sc. thesis and was considered only in the discussion of the results.

Regarding the elastic scattering measurement, the elastically scattered lithium ions were momentum analyzed by the MAGNEX spectrometer, spanning the angular range between $\theta_{lab}=2^\circ$ and $\theta_{lab}=10^\circ$, and were detected by its Focal Plane Detector (FPD). During the elastic scattering measurement, MAGNEX worked in an almost full horizontal angular acceptance but with a reduced vertical acceptance for protecting the focal plane detector from the elastic high counting rate. This acceptance defined the solid angle for the elastic scattering measurement and therefore deduced by the geometry of the applied slits. The beam charge was collected by a Faraday cup, set at the entrance of MAGNEX, and its absolute value was cross-checked via the measurement at the very forward angles where the elastic scattering is Rutherford.

The breakup measurement, performed at the energies of 20, 25 and 29 MeV, was an exclusive measurement obtained with the detection of both breakup fragments in coincidence. The alpha fragments were momentum analyzed by the MAGNEX spectrometer, spanning the angular range between -1° and 10° , and were detected by its FPD. In this measurement, MAGNEX worked in a full horizontal angular acceptance, and a rather well open vertical acceptance as the counting rate due to breakup was rather low. The elastic scattered ${}^6\text{Li}$ ions were swept out by the appropriate magnetic fields, allowing the detection of alphas in energy slices of 6.8 to 10.7 MeV, 8.4 to 13.3 MeV and 11.0 to 15.5 MeV, for the 20, 25 and 29 MeV runs,

respectively. The second breakup fragment, deuterons, were detected in a silicon detector, set at $\theta_{lab} = 5^\circ$ ($\Delta\theta_{lab}=4.2^\circ - 5.8^\circ$). This detector was masked, against Rutherford scattering deterioration, by tantalum foils of appropriate thicknesses. These foils absorbed all lithiums but allowed protons and deuterons to go through. Exclusive yields were determined for pairs of angles every 0.5° for alphas detected by MAGNEX in the angular range 0° to 10° , combined with deuterons detected at the fixed angle detector at 5° . The beam current was measured by a Faraday cup, located inside the spectrometer, beside the FPD and the efficiency of the detection system was determined via a Monte Carlo simulation program.

The first step of the data analysis included the energy and position calibration of MAGNEX, as well as the energy calibration of the silicon detector used for the breakup measurement. The next step of the analysis included the reconstruction of the data, as well as the particle identification for both elastic scattering and breakup. Subsequently, the differential cross sections for the elastic scattering were obtained in the laboratory system and were transformed to the center of mass system by calculating the appropriate Jacobians. The present elastic scattering data in inverse kinematics are found in good consistency with previous data obtained in direct kinematics. As the present data extend to more forward angles than the previous ones, where the scattering is Rutherford, they validate (or not) their normalization.

Regarding the breakup data, a Monte Carlo simulation program was adopted for determining the efficiency of the detection system. The program, following the discretization of continuum as in the CDCC approach (Continuum Discretized Coupled Channel), describes very well the experimental energy distributions of the breakup fragments. Taking into account gated simulated spectra under the experimental conditions and ungated ones, the efficiency of the detection system was determined. Subsequently by using the total efficiency of the detection system and the beam flux, double differential breakup cross sections were determined for all the measured α - d pairs. These cross sections were transformed to the center of mass frame by using the appropriate Jacobians assuming the inelastic scattering ${}^6\text{Li} + p \rightarrow {}^6\text{Li}^* + p$ assigning for the excited ${}^6\text{Li}$ nuclei an excitation energy E_x and an angle $\theta_{c.m.}$. The excitation energy E_x for each angle was determined as a weighted mean between the various excitation energies corresponding to the continuum energy bins adopted in the CDCC calculations. Furthermore, for each pair of laboratory angles ($\theta_{\alpha-lab}$, θ_{d-lab}), a center of mass angle $\theta_{c.m.}$ was assigned applying the Ohlsen formulas. In this way, the breakup angular distributions in the center of mass frame were calculated. Our breakup data are limited in the angular range between $\theta_{c.m.} = 10^\circ$ and $\theta_{c.m.} = 90^\circ$ in the center of mass frame since the considered events are associated to energies corresponding to the first solution of the kinematical equations. Events

with energy corresponding to the second kinematical solution were cut out due to the tantalum foils masking the fixed angle silicon detector or/and the selection of the detected energy range by the spectrometer. It should be noted that, breakup experimental angular distributions in the center of mass frame as well as total breakup cross sections were obtained for the first time at the energies of 25 and 29 MeV.

Regarding the theoretical interpretation of the present data, the elastic scattering data were considered in the microscopic approach of the Jeukenne-Lejeune-Mahaux (JLM) potential (without any coupling), which fails to reproduce the data. It should be noted that this is the first time that the JLM potential was tested both for a very light weakly bound projectile as ${}^6\text{Li}$ and at very low energies $E = 2.6 - 4.8$ MeV/u. Before, the JLM potential was found adequate to describe elastic scattering data for a weakly bound radioactive but heavier mass nucleus as ${}^{17}\text{F}$ at similar energies and compatible with elastic scattering for the same light weakly bound nucleus ${}^6\text{Li}$, but at much higher energies.

Further on, a global investigation of all reaction channels was considered in a Continuum Discretized Coupled Channel (CDCC) framework. Into this context, extensive CDCC calculations were performed adopting the $\alpha + d$ cluster model of ${}^6\text{Li}$ with the $p - \alpha$ and $p - d$ interactions obtained by fitting previous experimental data. The calculated angular distributions for both elastic scattering and breakup were compared with experimental data and found to be in very good agreement. According to the CDCC calculations, the sequential breakup via the first 3^+ resonance accounts for $\sim 50\text{-}60\%$ of the total breakup for the highest two energies, $\sim 38\%$ for 20 MeV and $\sim 0.04\%$ for the lowest energy, 16 MeV. It was also found that coupling to the full continuum (direct and resonant) is strong and adequate in order to describe the elastic scattering data in the most effective way. However, the most important coupling at all energies is the coupling to resonant breakup while, the coupling to direct breakup has in principle a small influence, which becomes larger at the higher energies. It should be noted that, at the lower energies, coupling to 3^+ resonance is very strong although, the resonant breakup cross section seems to be very small. Such a striking situation was also reported recently for the elastic scattering of ${}^7\text{Li} + p$. This interesting phenomenon may be an example of a "virtual" coupling to continuum. Last, total breakup cross sections were obtained integrating the differential cross sections by assuming the shape of the CDCC angular distributions for the angular region where experimental breakup data do not exist.

Total breakup cross sections as well as absorption cross sections given as output in our CDCC calculation were compared the first with our experimental breakup data and the second with data of the reaction ${}^6\text{Li} + p \rightarrow {}^4\text{He} + {}^3\text{He}$. This is the only available reaction channel with

significant cross section and was measured simultaneously with breakup, allowing a meaningful comparison in a theoretical framework. Indeed, the agreement between the experimental and theoretical absorption cross section for all energies is excellent, giving further support to the global interpretation of the ${}^6\text{Li} + \text{p}$ data in a CDCC framework and vice versa.

The validity of the present elastic scattering data was also checked into the global CDCC framework proposed by Guo and Matsumoto, using the JLM potential as entrance potential. These calculations were found in fair agreement with the experimental data at lower energies and larger angles and in good agreement with the data at the higher energies.

As a final comment, the technique described here is proved to be well-established both experimentally and theoretically allowing the study of similar systems with stable weakly bound or radioactive projectiles on proton/deuteron targets, with the MAGNEX spectrometer.

Introduction

This work is part of the curriculum of the Postgraduate Program of the Department of Physics, University of Ioannina. The research area belongs to the basic direction of Nuclear Physics and in particular on the subject of Nuclear Reactions involving weakly bound nuclei.

With the advent of radioactive beam facilities, elastic scattering involving exotic nuclei has been proved to be a powerful tool for probing the optical potential as well as for investigating coupling channel mechanisms especially at near barrier energies [1–3]. Radioactive beams in some cases are produced with significantly lower flux than the stable ones. Therefore, a fruitful research was developed the last decade with stable weakly bound nuclei [4], in principle at the same footing with the research based on radioactive nuclei. Such measurements can be performed with a high beam intensity and may be considered as predecessor measurements to the ones with radioactive nuclei. Amongst these, nucleon scattering involving weakly bound stable or radioactive nuclei is the most favorable and simplest tool for probing the potential and/or the structure of a nucleus. The measurements are performed in inverse kinematics even for stable projectile, for the last case not only to "mimic" the same conditions as with radioactive ones but to draw other technical benefits that will be described below.

The last years, several nucleon scattering studies were performed in inverse kinematics with radioactive projectiles, and the halo or skinlike nature of the projectile is probed as long as the potential is known and vice versa. For example for energies well above $E_{proj.} = 10$ MeV/u, the microscopic approach of the Jeukenne - Lejeune - Mahaux (JLM) potential [5] was the basis for several such studies [6–16]. This model was successfully applied in Refs. [17–19] for medium and heavy mass stable nuclei and for energies above 10 MeV/u with slight adjustments only on the imaginary part. The applicability of the method for lower energies ($7 \leq E \leq 24$ MeV/u) was tested in Ref. [20] and for low to high mass numbers in Refs. [18, 21]. Recently, the JLM potential was also validated for the system $^{17}\text{F} + \text{p}$ at a rather low energy ~ 4 MeV/u [22] providing good agreement with the data. Thus, it is very interesting to investigate the applicability of the model for a very light stable weakly bound projectile as ^6Li and at very

low energies.

The ${}^6\text{Li}$ nucleus exhibit a pronounced cluster structure with a low binding energy in the α -d channel and a low density of its excited states up to an excitation energy of about 16 MeV. Under these conditions, the choice of a standard optical potential is inapplicable. Also, it should be noted that, elastic scattering and reactions of nucleons and light nuclei with ${}^6\text{Li}$ are of great practical and theoretical importance, with serious consequences on astrophysical problems [23–26] as well as applications in fusion reactors [27–29]. The determination of low-energy cross sections, which belong to a deep sub-barrier region is a difficult task both from the theoretical and experimental point of view and the possible approach relies on extrapolations. The latter is based on the exact form of the potential barrier, the potential penetrability and the extrapolation of S-factors to zero energy. Therefore, elastic scattering and reaction/breakup measurements at low energies could be very useful for a detailed theoretical approach.

Several articles exist in the literature concerning measurements on elastic scattering of protons from ${}^6\text{Li}$ in direct kinematics and a detailed compilation can be found in [30]. Measurements in a wide energy range ($E = 1.6$ to 12 MeV/u) and a rather wide angular range $\theta_{lab}=30^\circ$ to 165° are found in Refs. [31, 32] while polarization and phase shift measurements in Refs. [33, 34] for $E = 0.5$ to 5.6 MeV/u. It should be mentioned that most of these measurements are relative measurements, and the normalization is obtained via a thick target study [35]. The theoretical analysis of these data is mainly focused on the ${}^7\text{Be}$ structure and not on the potential except Haller et al. [32], where an optical potential is used to fit the data allowing the various parameters to strongly depend on energy. The polarization measurements fail to give a clear picture due to several parameters which have to be determined. Between these parameters we can notice the unknown total reaction cross section needed to fit the absorption. Theoretical approaches to probe the potential, in a folding and Coupled Channels (CC) context are found in Refs. [21, 36, 37], but they deal with data at rather high energies above $E= 25$ MeV/u. Four recent interesting articles [38–41] present Continuum Discretized Coupled Channel (CDCC) calculations and calculations with a microscopic M3Y potential respectively, from rather low to higher energies (~ 5 to 155 MeV/u).

A comprehensive study in the CDCC framework requires not only the measurement of elastic scattering channel but also the measurement of the breakup and the other reaction channels. It is well known that, weakly bound nuclei possess most of the times one bound state, the ground state, and a broad featureless continuum. Due to their cluster structure with small separation energies, they can be easily excited above their particle emission threshold. Hence their breakup reactions induced by the Coulomb and nuclear fields of suitable targets

could be useful tools to investigate their structure as well as coupling channel effects. Into this context, the simplest breakup process can be obtained on a proton target in a complementary mode with elastic scattering.

In our case, due to the pronounced cluster structure of the ${}^6\text{Li}$ nucleus as well as to its very low binding energy in the α -d channel (1.47 MeV), the breakup of this nucleus is expected to be large. It has mainly been investigated in exclusive measurements at near barrier energies on light [42, 43], medium [44–51] and heavy targets [51–61]. Interest was also shown for the effect of resonant and direct breakup on elastic scattering [62–68]. For breakup of ${}^6\text{Li}$ on protons only one comprehensive work was published in Ref. [69] many years ago, but at much higher energies than the Coulomb barrier ($\sim 12 \times V_{C.b.}$). Moreover neither the total breakup cross section nor the angular distributions in the center of mass system are given in Ref. [69].

Considering all the above, it was proposed the investigation of the system ${}^6\text{Li} + p$, including both elastic scattering and breakup measurements, at four near barrier energies, namely 16, 20, 25 and 29 MeV (2.67 - 4.83 MeV/u). The experimental data were collected in Istituto Nazionale di Fisica Nucleare - Laboratori Nazionali del Sud (INFN - LNS) [70], in Catania, Italy while, the analysis of the data was completed at the NPL - Ioannina [71]. This work is part of a project proposed by Prof. A. Pakou including several studies in inverse kinematics [16, 22, 72–79].

In particular, the elastic scattering of protons by ${}^6\text{Li}$ is revisited in inverse kinematics and by using the MAGNEX spectrometer [80–89]. By setting MAGNEX close to zero, and thanks to its large acceptance, we can span almost a full angular range in the center of mass frame all in one go, facilitating our normalization via Rutherford scattering at the most forward angles. This can validate or not the normalization adopted in the previous data, and remove possible systematic uncertainties. Furthermore, this experiment is considered as a predecessor measurement to ones with other weakly bound stable or radioactive projectiles. The final goal is the breakup measurement, which can be easier accessible in inverse kinematics, since all the ejectiles are confined at forward angles and MAGNEX is a powerful tool, capable of detecting them with very good angular and energy resolution. The breakup measurement was performed in its own right and also as complementary measurement to elastic scattering and to the other open reaction channel ${}^6\text{Li} + p \rightarrow {}^4\text{He} + {}^3\text{He}$ reported in [75, 76] and performed simultaneously at the same experiment. A global investigation of all reaction channels will be considered in a Continuum, Discretized, Coupled Channel (CDCC) framework.

Taking into consideration all the above, the present work includes:

- A chapter with the theoretical background, necessary for the data interpretation (Chapter

1).

- The details of the relevant experiment performed at the MAGNEX facility of the INFN - LNS (Chapter 2).
- The data reduction (Chapter 3) and in particular the calibration procedure (3.1), the particle identification (3.2) and the determination of the cross sections for both the elastic scattering (3.3) and the breakup process (3.4).
- The theoretical interpretation (Chapter 4), including calculations using the microscopic Jeukenne-Lejeune-Mahaux potential (4.1) as well as calculations in the Continuum Discretized Coupled Channel framework (4.2)
- The concluding remarks (Chapter 5).

This work also contains appendices with:

- ◇ The determination of the effective beam energy, useful for the ray-reconstruction procedure (Appendix A).
- ◇ The error estimation of the cross section for both elastic scattering and breakup data (Appendix B).
- ◇ Computer programs converting the differential cross sections from the laboratory to the center of mass frame and vice versa (Appendix C).
- ◇ Tabulated values of the experimental data (Appendix D).

Chapter 1

Theory

This chapter includes a brief introduction to the theoretical background, necessary for the data interpretation. The main principles regarding the elastic scattering process will be described in section 1.1 and include an introduction to scattering theory (subsection 1.1.1) as well as to the optical model (subsection 1.1.2). A brief introduction to the breakup process will be presented in section 1.2 and finally, the principles of the Continuum Discretized Coupled Channel (CDCC) calculations will be described in section 1.3.

1.1 Elastic Scattering

Elastic scattering is the simplest and most favorable tool in the basic direction of Nuclear Physics giving important information on the structure of the involved nuclei as well as on the nature of forces between them. Moreover it is well known that several discoveries in Nuclear Physics have been performed via scattering experiments.

The simplest form of a nuclear reaction is a reaction with two outgoing particles:

$$a + X \rightarrow Y + b \tag{1.1}$$

where a and X are the projectile and the target nucleus respectively while, b and Y are the ejectile (the observed particle) and the residual nucleus respectively. Eq. (1.1) can be written equivalently as follows:

$$X(a, b)Y \tag{1.2}$$

In the case of elastic scattering process, the incident and outgoing particles are the same and are found in their ground states. The Q-value of the elastic scattering is equal to zero while the energy, momentum modulus and particle number are conserved.

1.1.1 Scattering Theory

Scattering is characterized by the differential and the total cross section. The differential cross section is given as:

$$\frac{d\sigma}{d\Omega} = |f(\theta, \varphi)|^2 \quad (1.3)$$

where $f(\theta, \varphi)$ is the scattering amplitude. The total cross section is given by the following formula [90]:

$$\sigma = \int \frac{d\sigma}{d\Omega} d\Omega = \int_0^{2\pi} d\varphi \int_0^\pi \frac{d\sigma}{d\Omega} \sin\theta d\theta \quad (1.4)$$

The simplest classical scattering process is the Coulomb scattering. The Schrödinger equation for a Coulomb potential at a radius $r \geq R_c$ is:

$$\left[-\frac{\hbar^2}{2\mu} \nabla^2 + \frac{Z_1 Z_2 q^2}{4\pi\epsilon_0 r} \right] \Psi(r) = E \Psi(r) \quad (1.5)$$

where Z_1, Z_2 are the atomic number of the projectile and the target respectively, q is the charge of the proton and E is the center of mass energy. The wavefunction $\Psi(r)$ at the limit $r \rightarrow \infty$ is:

$$\Psi(r, \theta, \varphi) = e^{ikz} + \frac{f(\theta, \varphi) e^{ik'r}}{r} \quad (1.6)$$

where k, k' are the incident and scattering wavenumbers, Taking into account all the above and by following the prescription described in Ref. [91] it is possible to lead to the Rutherford scattering cross section in the center of mass frame [90, 91]:

$$\frac{d\sigma}{d\Omega} = |f(\theta, \varphi)|^2 = \left[\frac{1}{4\pi\epsilon_0} \frac{Z_1 Z_2 q^2}{4E} \right]^2 \frac{1}{\sin^4(\theta/2)} \quad (1.7)$$

More complicated situation may occur if the interacting potential is not the Coulomb but the nuclear one. Assuming an interaction potential $V = V(r)$ in a partial wave description, one can write the wavefunction as:

$$\Psi(r, \theta) = \sum_{l=0}^{\infty} \alpha_l R_l(r) Y_{l0}(\theta) \quad (1.8)$$

where the coefficient α_l is the amplitude of the l^{th} partial wave. In Eq. (1.8), the wavefunction was written into a product of radial and angular terms. Considering systems independent of the azimuthal angle φ only the spherical harmonics with $m=0$ are involved. So, $Y_{lm}(\theta, \varphi) \rightarrow Y_{l0}(\theta)$ [91].

The spherical harmonic $Y_{l0}(\theta)$ is an eigenfunction of the angular part of the Schrödinger equation with eigenvalue $l(l+1)$. Apart from that, we can define the function:

$$u_l(r) \equiv r R_l(r) \quad (1.9)$$

Then the radial wave function for partial wave l satisfies the following equation [91]:

$$\frac{d^2 u_l(r)}{dr^2} - \left[\frac{l(l+1)}{r^2} + \frac{2\mu}{\hbar^2} V(r) - k^2 \right] u_l(r) = 0 \quad (1.10)$$

For $r \rightarrow \infty$ and by considering short-range potentials, the two first terms of eq. (1.10) are approximately zero. So, in the asymptotic region $r \rightarrow \infty$, the eq. (1.10) may be written as:

$$\frac{d^2 u_l(r)}{dr^2} + k^2 u_l(r) = 0 \quad (1.11)$$

The solutions of the second-order differential equation (1.11) are:

$$u_l(r) \rightarrow A_l \sin(kr - \frac{l\pi}{2}) + B_l \cos(kr - \frac{l\pi}{2}) \quad (1.12)$$

or equivalently:

$$u_l(r) \rightarrow C_l \sin(kr - \frac{l\pi}{2} + \delta_l) \quad (1.13)$$

where δ_l is the phase shift. Also, A_l and B_l or C_l can be determined from the boundary conditions [91].

Then, the wavefunction $\Psi(r, \theta)$ can be written as:

$$\Psi(r, \theta) \rightarrow \sum_{l=0}^{\infty} D_l \frac{Y_{l0}(\theta)}{r} \sin(kr - \frac{l\pi}{2} + \delta_l) \quad (1.14)$$

where D_l can be determined from the boundary conditions. Considering again a scattered wave with a wavefunction similar to the one of eq. (1.6) and by using the spherical Bessel functions, the scattering amplitude may be written as follows [91]:

$$f(\theta) = \frac{\sqrt{4\pi}}{k} \sum_{l=0}^{\infty} \sqrt{2l+1} e^{i\delta_l} \sin\delta_l Y_{l0}(\theta) \quad (1.15)$$

while the differential elastic scattering cross section can be written as:

$$\frac{d\sigma}{d\Omega} = \frac{4\pi}{k^2} \left| \sum_{l=0}^{\infty} \sqrt{2l+1} e^{i\delta_l} \sin\delta_l Y_{l0}(\theta) \right|^2 \quad (1.16)$$

A detailed description of the procedure can be also found in Refs. [90–94].

1.1.2 Optical Potential

In principle, when a nucleon is incident on a nucleus may be elastically scattered or it may create a variety of reactions [95]. In the optical model framework the interaction between two nuclei is represented by a complex potential. The real part is referred to the elastic scattering (analogous to the refraction in optics) while, the imaginary part accounts for the loss of flux going to any other open, non-elastic channels (analogous to the absorption in optics). At low energies the attenuation of the incident wave is predominant near the nuclear surface, due to the fact that the imaginary part of the potential may be large near the surface. As the incident energy increases, this phenomenon may become less important while, the absorption of the incident wave may take place throughout the whole nuclear volume [96, 97]. In general, the optical potential is given by the following formula [90, 98]:

$$V = V_0 + iW_0 \quad (1.17)$$

where V_0 and W_0 are the real and the imaginary part of the potential, respectively.

In this framework, both macroscopic and microscopic potentials can be used.

Macroscopic Potentials

In the macroscopic approach of the optical potential, the interaction between two nuclei is simplified by taking into account the nucleus a whole system. Several potentials have

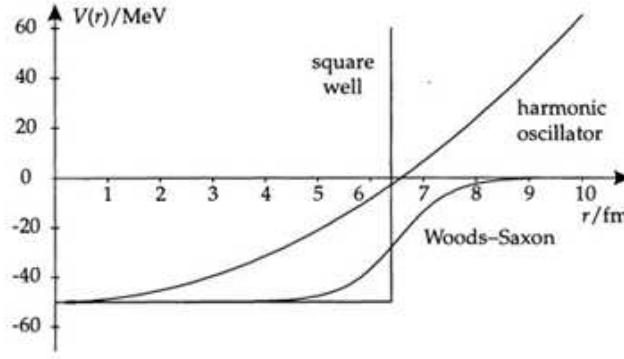


Figure 1.1: A comparison between the Woods - Saxon potential, the harmonic oscillator and the square well.

been proposed in order to describe the nucleus - nucleus interactions in a phenomenological framework. The most common one is the Woods - Saxon potential [95]. This follows closely the density distribution of the nucleons:

$$\rho(r) = \frac{\rho_0}{1 + e^{(r-R)/\alpha}} \quad (1.18)$$

and it is given by the following formula:

$$V(r) = \frac{V_0}{1 + e^{(r-R)/\alpha}} \quad (1.19)$$

where V_0 (MeV) represents the potential depth, $R = r_0 A^{1/3}$ (fm) the nuclear radius and α (fm) the diffuseness.

The Woods - Saxon potential is an attractive potential (increase with distance) and it is approximately flat in the center, for large mass numbers A . A comparison between the Woods - Saxon potential, the harmonic oscillator and the square well is presented in Figure 1.1. Usually, in optical model framework, this potential is used to describe both a real and an imaginary part, according to the following formula:

$$U(r) = \frac{V_0}{1 + e^{(r-R_v)/\alpha_v}} + i \frac{W_0}{1 + e^{(r-R_w)/\alpha_w}} \quad (1.20)$$

Eq. (1.20) is the simplest form of an optical potential based on Woods-Saxon volume terms for both the real and the imaginary part. In fact, a complete optical potential may be consisted of several terms. For example, an imaginary surface term is usually used instead of the imaginary volume term or complementary to that. This surface term is usually taken

to be the radial derivative of Woods - Saxon form factor [95, 99]. Also, especially at nucleon scattering, an additional spin - orbit (s.o.) term of so-called Thomas type is often substantial in order to reproduce the experimental data [90–92, 94, 95, 99, 100]. The radial dependence of such a spin - orbit term is similar to the surface one [99]. Finally, for charged particles scattering, a Coulomb term should be included in the complete optical potential according to the formula [91, 92, 100]:

$$V_c(r) = \begin{cases} \left[\frac{1}{4\pi\epsilon_0} \right] \frac{Z_1 Z_2 q^2}{2R_c} \left(3 - \frac{r^2}{R_c^2} \right) & \text{for } r \leq R_c \\ \left[\frac{1}{4\pi\epsilon_0} \right] \frac{Z_1 Z_2 q^2}{r} & \text{for } r \geq R_c \end{cases} \quad (1.21)$$

where R_c is the Coulomb radius, q the charge of the proton and Z_1 , Z_2 are the atomic number of the projectile and the target respectively. Thus, the complete phenomenological optical potential follow the formula:

$$U_{opt}(r) = V_c(r) + U_{volume}(r) + U_{surface}(r) + U_{s.o.}(r) \quad (1.22)$$

The disadvantage of the macroscopic method is that many different sets of parameters can be found to give good fits to the experimental data. This raises the question which physical content is correct. However, several methods have been developed to anticipate this problem [97, 101–106].

Microscopic Potentials

In the microscopic approach in principle the potential is obtained by assuming a nucleon-nucleon effective interaction. The method includes two different categories [107]. In the first category ground state and transition densities are folded with an effective nucleon - nucleon interaction in order to generate the ground state and transition potentials. In the second category the calculation starts from an infinite nuclear matter optical potential and the elastic scattering and the transition optical potential of finite nuclei are deduced by using the relevant ground state and transition densities [107]. Several microscopic approaches of both categories have been proposed [5, 14, 108, 109].

Regarding the first category of microscopic calculations, the potential is obtained by using an effective nucleon - nucleon interaction folded over matter densities of the interacting nuclei [14]. Such a so called double folding potential may be written as:

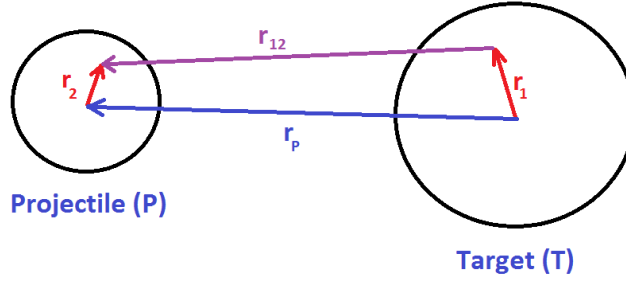


Figure 1.2: The coordinates for the double folding integral of Eq. (1.23).

$$U(\mathbf{r}_P) = \iint \rho_T(\mathbf{r}_1) \rho_P(\mathbf{r}_2) u(\mathbf{r}_{12}) d\mathbf{r}_1 d\mathbf{r}_2 \quad (1.23)$$

where ρ_P and ρ_T are the density distributions of the projectile and the target respectively while, $u(\mathbf{r}_{12})$ is the effective interaction and it has the form:

$$u(r_{12}) = u_{00} + u_{01} \boldsymbol{\tau}_1 \cdot \boldsymbol{\tau}_2 + u_{10} \boldsymbol{\sigma}_1 \cdot \boldsymbol{\sigma}_2 + u_{11} \boldsymbol{\tau}_1 \cdot \boldsymbol{\tau}_2 \boldsymbol{\sigma}_1 \cdot \boldsymbol{\sigma}_2 \quad (1.24)$$

with $\boldsymbol{\sigma}$ and $\boldsymbol{\tau}$ the Pauli and Isospin matrices, respectively [14,94,108]. The coordinates used in double folding calculations are presented in Figure 1.2. It should be noted that, if only one of the integrations in Eq. (1.23) is done, the result is a single folding nucleon - nucleon potential. Such a simpler approach is more useful in nucleon scattering.

In the present work the microscopic potential derived by Jeukenne, Lejeune and Mahaux (JLM) was used [5]. This potential was the basis for several nucleon - nucleus studies (e.g. [6–13, 15, 107]) and belongs to the second category of the microscopic calculations described above [107]. It should be noted that, both the real and the imaginary part of a nucleon - nucleus optical potential may be obtained in the framework of the JLM model. The starting point for a calculation based on the JLM potential is the Brueckner - Hartree - Fock approximation and the Reid's hard core nucleon - nucleon interaction which provide the energy and density dependence of the isoscalar, isovector and Coulomb components of the complex optical model potential in infinite nuclear matter [5, 14, 107]. Then, applying the local density approximation (LDA), the spherical optical potential of a finite nucleus can be obtained. Starting from the infinite nuclear matter density and by using this approximation, one can extract the density distribution of a finite nucleus. In the LDA framework, the real and the imaginary part of the optical potential are determined as a function of energy E and density distribution of the (finite) nucleus $\rho(r)$. A number of coefficients necessary for the calculations are tabulated in Ref. [5] while a normalization factor $\lambda_W \sim 0.8$ of the imaginary part may be applied. It should

be noted that in the JLM model, numerical results for the real and imaginary part of the potential were parameterized in order to obtain analytical forms, taking into account data of medium and heavy mass stable nuclei at the energy interval $10 \leq E \leq 160$ MeV/u. The model was successfully applied to stable nuclei inside that energy region in Refs. [17–19]. However, the application of this approach outside the mass and energy interval, where the model was validated, constitutes a severe test to it. A comprehensive discussion of these points can be found in Ref. [14]. The applicability of the JLM method at lower energies ($7 \text{ MeV/u} \leq E \leq 24 \text{ MeV/u}$) was tested in Ref. [20] and for low to high mass numbers in Refs. [18, 21]. Also, the applicability of the JLM potential was checked for medium and heavy mass targets but, at high energies ($E \sim 200 \text{ MeV/u}$) in Ref. [110]. Recently, the JLM potential was also validated for the weakly bound radioactive projectile ^{17}F scattered from protons at a rather low energy $\sim 4 \text{ MeV/u}$ [22], providing good agreement with the data.

1.2 Breakup process

The investigation of the reaction mechanisms involved in collisions of weakly bound nuclei considers various processes. Amongst them the breakup is of great importance. In a pure breakup reaction, the projectile nucleus, which is usually a weakly bound one and thus is characterized by low binding energy, breaks into two or more fragments due to the nuclear and Coulomb interactions with the target [1, 111]. Breakup reactions may be distinguished in sequential and direct processes [111].

In **sequential breakup** the ejectile is produced in a particle unstable state which will subsequently decay. In this case the properties of the breakup fragments are determined by the populated state of the ejectile. Information on the reaction mechanism may be lost, to a large extent, due to the relatively long life-time of those states [111]. In general, a sequential breakup reaction with three particles in the final state can be written as:

$$a + X \rightarrow a^* + X \rightarrow c + d + X \quad (1.25)$$

where a and X are the projectile and the target nucleus respectively while, a^* is the unbound ejectile in an excited state, which decays into particles c and d .

On the other hand, in **direct breakup** process, the particles in the final state are produced simultaneously, without forming the intermediate particle unbound state [111]. In case of direct breakup with three particles in the final state, the reaction can be written as:

$$a + X \rightarrow c + d + X \quad (1.26)$$

where a and X are the projectile and the target nucleus respectively while, c and d are the breakup fragments. The fragments c and d are related to the projectile a and hence exhibit its properties [111]. The ground state - ground state Q-value can be written as a function of the involved masses as:

$$Q_{gg} = m_a - (m_c + m_d) = -E_b \quad (1.27)$$

where E_b is the binding energy.

Breakup processes may be also classified as follows (without including processes of compound nucleus modes):

- **Elastic breakup:** All the particles in the final state are emitted in their ground state and thus, the reaction can be written as: $a + X \rightarrow c_{g.s} + d_{g.s} + X_{g.s}$.
- **Inelastic breakup:** The breakup is accompanied by the excitation of some of the reaction products. This process may include target excitations ($a + X \rightarrow c + d + X^*$) or core excitations ($a + X \rightarrow c^* + d + X$) [112].
- **Breakup after transfer:** Breakup process follows a transfer reaction. In this case Eq. (1.25) may be written as: $a + X \rightarrow b + Y \rightarrow c + d + Y$.

In the present work, we deal mainly with elastic projectile breakup in the sequential as well as the direct mode:

$$\begin{aligned} \text{sequential : } & {}^6\text{Li} + {}^1\text{H} \rightarrow {}^6\text{Li}^* + {}^1\text{H} \rightarrow {}^4\text{He} + {}^2\text{H} + {}^1\text{H} \\ \text{direct : } & {}^6\text{Li} + {}^1\text{H} \rightarrow {}^4\text{He} + {}^2\text{H} + {}^1\text{H} \end{aligned} \quad (1.28)$$

A schematic representation of sequential breakup via the 3^+ resonance state ($E_x = 2.186$ MeV) and direct breakup to the non - resonant continuum for the ${}^6\text{Li} + \text{p}$ system is illustrated in Figure 1.3.

It should be noted that the contribution of the reaction ${}^6\text{Li} + {}^1\text{H} \rightarrow {}^5\text{Li} + {}^2\text{H} \rightarrow {}^4\text{He} + {}^1\text{H} + {}^2\text{H}$ (breakup after transfer) in our spectra, was evaluated via our simulation analysis and it was found not to affect our data.

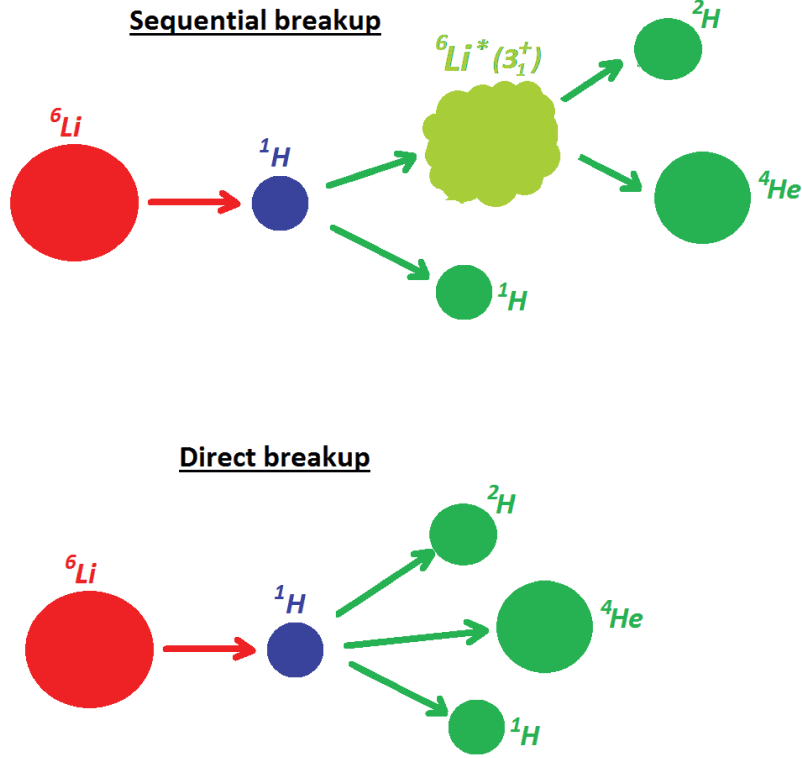


Figure 1.3: Schematic representation of sequential and direct breakup for the ${}^6\text{Li} + p$ system.

1.3 Continuum Discretized Coupled Channel (CDCC) calculations

The Continuum Discretized Coupled Channel (CDCC) method is used in order to describe elastic scattering and breakup processes taking into account couplings to the resonant and non-resonant continuum states of the weakly bound nucleus. The CDCC method was originally developed inside the framework proposed by Johnson, Soper and Rawitscher in Refs. [113, 114] in order to describe the effect of breakup in deuteron scattering by Nickel and Calcium targets. The last decades the method was refined and became increasingly popular. This method is based on the discretization of the continuum space above the breakup threshold and the goal of such calculation is the determination of the cross sections for the elastic scattering and the breakup channels [115]. Except the angular distributions of elastic and breakup channels, the output of a CDCC calculation includes also absorption as well as total reaction cross sections. These information allow for a global investigation of all reaction channels in a comprehensive way. One of the most widespread tools that is used to perform such calculations is the FRESKO code [116].

In the CDCC approach, the weakly bound nucleus is assumed to have an internal cluster structure of a core and a valence nucleus. The weakly bound nucleus is usually the projectile one. Thus, in a relevant calculation the (core + target) and (valence + target) potentials are involved. It should be noted that these potentials are of great importance with a significant effect in the results of the calculation. In particular, the central potential in the entrance channel as well as the coupling potential were derived from the (core + target) and (valence + target) potentials by means of a single folding method [38, 64]:

$$U_{i \rightarrow f}^{SF}(R) = \left\langle \Psi_f(r) \left| U_{v-t} \left(\left| \vec{R} + \frac{2}{3} \vec{r} \right| \right) + U_{c-t} \left(\left| \vec{R} - \frac{1}{3} \vec{r} \right| \right) \right| \Psi_i(r) \right\rangle \quad (1.29)$$

where \vec{R} connects the centers of mass of the projectile (core + valence system) and the target, \vec{r} is the vector which connects the center of mass of core and valence while, U_{c-t} and U_{v-t} are the (core + target) and (valence + target) potentials, respectively. In our case, these potentials were obtained from an optical model analysis of elastic scattering data of the ($\alpha + p$) and ($d + p$) systems.

Regarding the discretization procedure, it should be noted that, the three-body wave function of the system is expanded in terms of the eigenstates of projectile Hamiltonian, including the existing bound and unbound states. To make the expansion finite, the continuum above the breakup threshold is approximated by a discrete representation in terms of square-integrable functions (continuum discretization) [115]. In our case, the non-resonant continuum above the ${}^6\text{Li} \rightarrow {}^4\text{He} + {}^2\text{H}$ breakup threshold was discretized into a finite number of momentum bins of equal widths Δk while, the only resonance involved in our calculation (3^+ , $E_x = 2.186$ MeV) was treated as a momentum bin, corresponding to a width of 100 keV. It should be noted that, the momentum k of the ${}^4\text{He} + {}^2\text{H}$ relative motion is given as [63, 64]:

$$k = \sqrt{\frac{2\mu}{\hbar^2} E_x} \quad (1.30)$$

where E_x is the ${}^6\text{Li}$ excitation energy above the ${}^4\text{He} + {}^2\text{H}$ breakup threshold while μ is the reduced mass. The wave functions for the bins are calculated as [38]:

$$\Psi(r) = \frac{1}{\sqrt{\Delta k}} \int_{\Delta k} \phi(r, k) dk \quad (1.31)$$

For the calculation of $\phi(r, k)$ the (core + valence) potential is necessary. In our case, the potential binding the deuteron to the α particle core was assumed to have a Woods - Saxon shape as described in Ref. [64].

Besides the discretization and truncation of the momentum space, the continuum is also truncated in L , the relative orbital angular momentum between the valence and the core nucleus. The maximum value of L is usually adjusted empirically by checking the convergence of the calculation. For the ${}^6\text{Li} + p$ study, the relative orbital angular momentum between the alpha particle and the deuteron was limited to the values $L = 0, 1, 2$. The discretization procedure is depicted in Figure 1.4.

The general principles of the CDCC method are described in details in Refs. [115]. Representative works involving the weakly bound nucleus ${}^6\text{Li}$ with a detailed description of the CDCC calculation procedure are reported in Refs. [38, 63, 64]. Finally, the overall procedure and the results of the CDCC calculations, performed in the present study, are presented in Chapter 4 as well as in Refs. [73, 74].

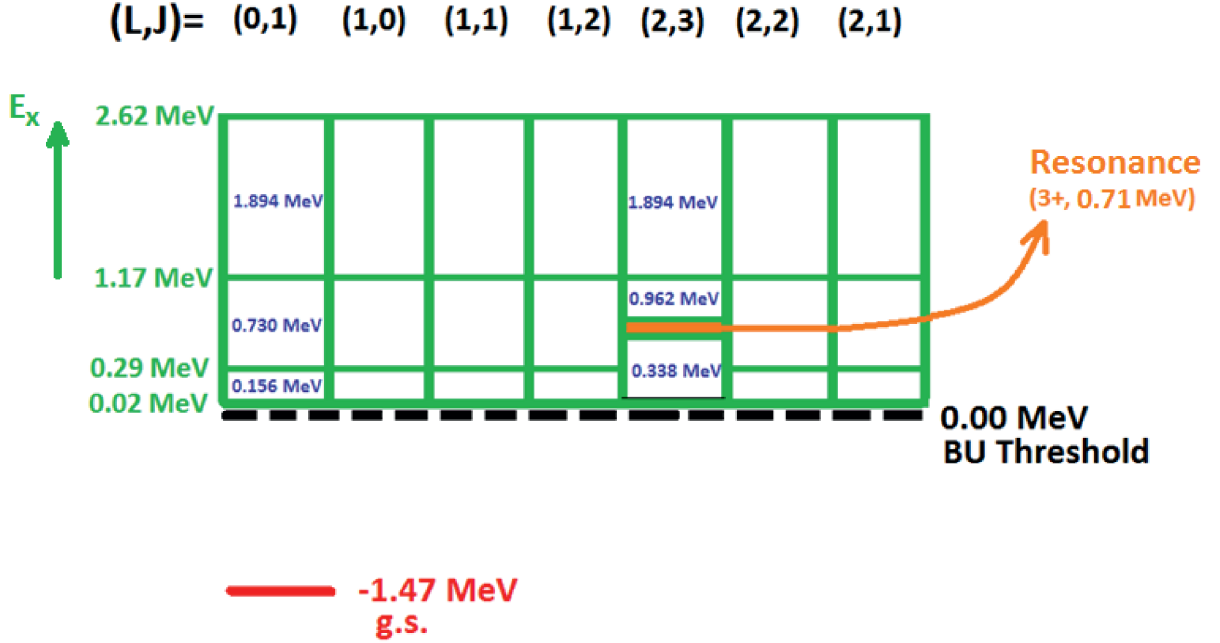


Figure 1.4: Discretization of the continuum phase space as it was considered in the CDCC calculations for the ${}^6\text{Li} + p$ system at 29 MeV (4.83 MeV/u). The values of the mean excitation energy of each bin with respect to the breakup threshold are indicated with the blue color while, the bin which is designated with the orange box correspond to the 3^+ resonance.

Chapter 2

Experimental Details

The goal of the present work is the study of the ${}^6\text{Li}+\text{p}$ system in inverse kinematics at near barrier energies ($3 \leq E/V_{C.b} \leq 6$). The relevant experiment includes three different parts: the elastic scattering measurement, the breakup measurement, obtained with the MAGNEX spectrometer [80–89], and the measurement of the reaction $\text{p}({}^6\text{Li}, {}^3\text{He}){}^4\text{He}$. The last, performed with a module of the GLORIA/DINEX array [117], was the subject of the M.Sc. thesis of Ch. Betsou [75, 76] and will be considered only in the discussion of the results. The experimental setup for the elastic scattering and the breakup measurements, the topics studied in this thesis, are described in section 2.1. Information regarding the MAGNEX spectrometer are presented in section 2.2. Details about the silicon detector used in coincidence with MAGNEX for the breakup measurement as well as some information about the electronics are presented in section 2.3 and 2.4, respectively. Finally, some information regarding the targets used in the present experiment are presented in section 2.5.

2.1 Experimental setup and procedure

The experimental setup was visualized at the MAGNEX facility [80–89] at the Istituto Nazionale di Fisica Nucleare - Laboratori Nazionali del Sud (INFN-LNS) in Catania, Italy [70]. A view of the experimental hall where the experiment took place is presented in Figure 2.1. Beams of ${}^6\text{Li}^{3+}$ were accelerated by the Tandem accelerator at the energies of 16, 20, 25 and 29 MeV and impinged on CH_2 targets of appropriate thicknesses. Measurements were repeated with ${}^{12}\text{C}$ targets of similar thicknesses, for estimating the background in the data due to the ${}^{12}\text{C}$ presence in the CH_2 targets. The acceptance of the spectrometer is defined by four slits,

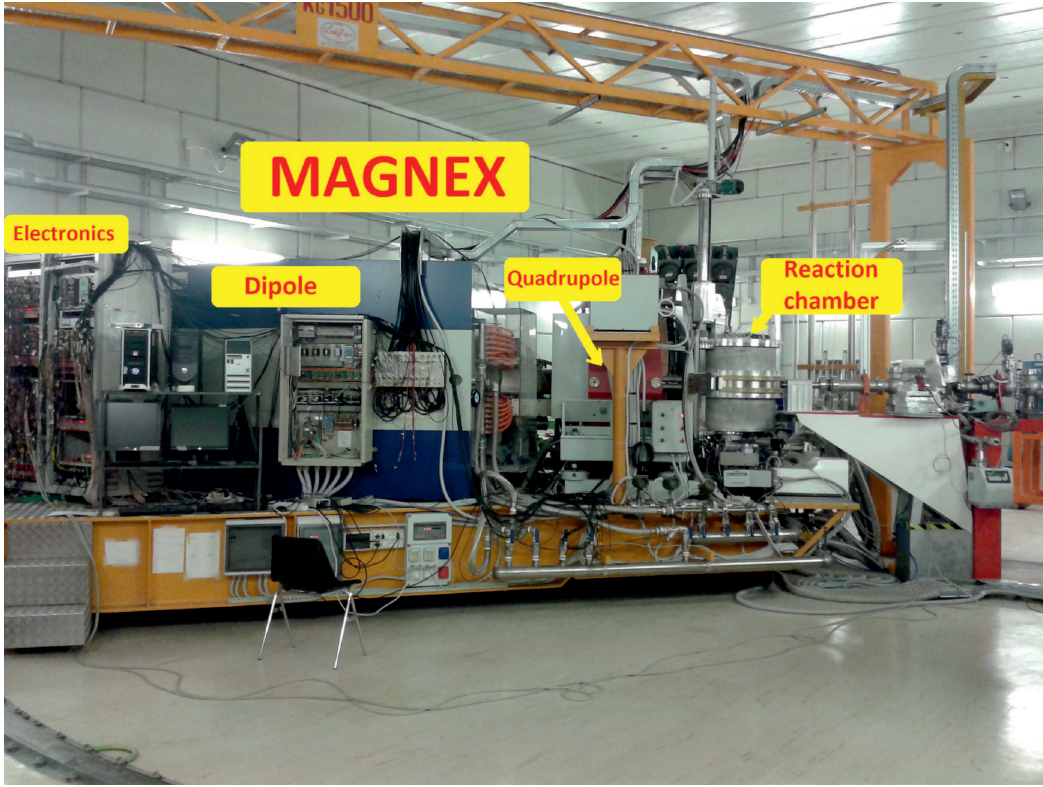


Figure 2.1: A view of the experimental hall where the experiment took place.

two for the horizontal and two for the vertical position located at the entrance of MAGNEX (no. 5 in figure 2.3). A schematic representation of the experimental setup is illustrated in Figure 2.2 while, views of the reaction chamber are presented in Figure 2.3.

Regarding the elastic scattering measurement, the elastically scattered lithium ions were momentum analyzed by the MAGNEX spectrometer [80–82, 86–89], whose optical axis was set at $\theta_{opt}=4^\circ$ and were detected by its Focal Plane Detection system (FPD) [84, 85]. During the elastic scattering measurement, MAGNEX worked in an almost full horizontal angular acceptance (2° - 10°) but with a reduced vertical acceptance for protecting the focal plane detector from the elastic high counting rate. Finally, the beam charge was collected by a Faraday cup, set at the entrance of MAGNEX (no. 3 in figure 2.3), and its absolute value was cross-checked via the measurement at the very forward angles where the elastic scattering is Rutherford.

The breakup measurement was an exclusive measurement obtained by the detection of both breakup fragments in coincidence. The alpha fragments were momentum analyzed by the MAGNEX spectrometer [80–82, 86–89], whose optical axis was also set at $\theta_{opt}=4^\circ$, and were detected by its FPD [84, 85]. In this measurement, MAGNEX worked in a full horizontal

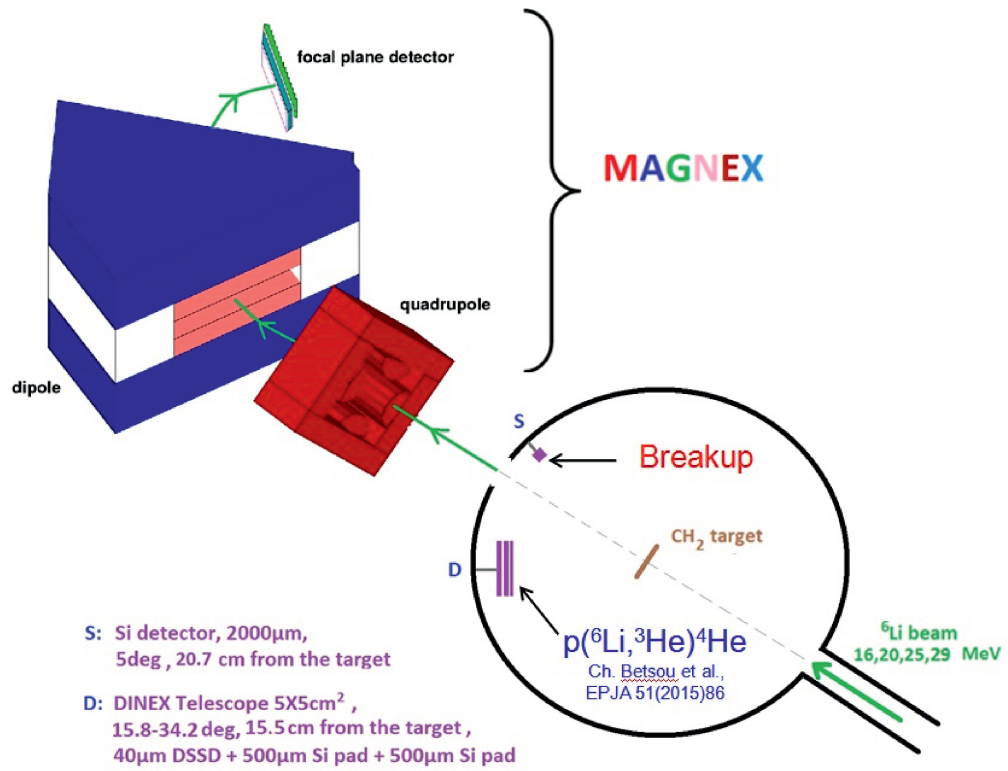
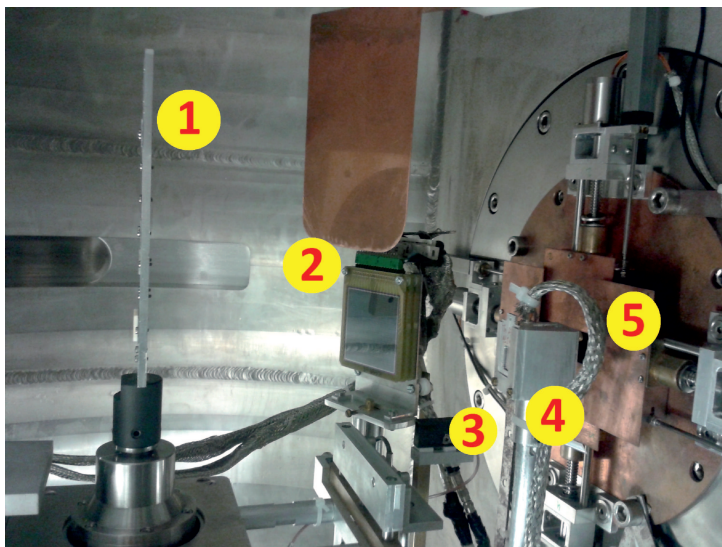


Figure 2.2: Schematic setup of the experiment.



- 1 Target ladder
- 2 DINEX/GLORIA
- 3 Faraday cup
- 4 Silicon detector at 5°
- 5 Slits



Figure 2.3: Views of the reaction chamber.

angular acceptance ($-1^\circ - 10^\circ$), and a rather well open vertical acceptance as the counting rate due to breakup was rather low. The elastic scattered ${}^6\text{Li}$ ions were swept out by the appropriate magnetic fields, allowing the detection of alphas in energy slices of 11.0 to 15.5 MeV, 8.4 to 13.3 MeV and 6.8 to 10.7 MeV for the 29, 25 and 20 MeV run, respectively. The second breakup fragment, deuterons, were detected by a silicon detector, set at $\theta_{lab} = 5^\circ$. This detector was masked, against Rutherford scattering deterioration, with 43.6, 30.8 and 25.9 μm tantalum foils respectively for the 29, 25 and 20 MeV measurements. These foils absorbed all lithiums but allowed protons and deuterons to go through. Exclusive yields were determined for pair of angles every 0.5° for alphas detected by MAGNEX in the angular range 0° to 10° , combined with deuterons detected by the fixed angle detector at 5° . The beam current was measured by a Faraday cup, located inside the spectrometer, beside the FPD.

2.2 The MAGNEX Spectrometer

The study of the motion of charged particles through a magnetic field is a standard technique in order to explore the structure of the matter. One of the most important applications of this technique is the development of the magnetic spectrometers for nuclear reaction studies. The first magnetic spectrometer used for nuclear reaction measurements was designed by R. J. Van de Graaf and his team [118, 119] at MIT, and it follows closely the dimensions of the one designed by Cockcroft [120] and used by Rutherford for alpha-decay studies [119, 121]. The reactions under investigation by R. J. Van de Graaff and his team were ${}^6\text{Li}(\text{d}, \text{p}){}^7\text{Li}$ and ${}^9\text{Be}(\text{d}, \alpha){}^7\text{Li}$ [119]. Other representative instruments at the early ages of the spectrometers were developed at CalTech [122, 123], MIT [124], Oak Ridge [123, 125], Pittsburgh [123, 126] and Berkeley [123, 127]. The last one was among the first instruments especially designed for heavy ions experiments. The last decades several high - performance devices were developed like VAMOS [128] at GANIL (France), SHARAQ [129] and SAMURAI [130] at RIKEN (Japan), PRISMA [131] at INFN-LNL (Italy) and MAGNEX [80–82] at INFN-LNS (Italy).

MAGNEX is a high - performance magnetic spectrometer installed at the Istituto Nazionale di Fisica Nucleare - Laboratori Nazionali del Sud (INFN-LNS) and operated by the MAGNEX group - head Prof. F. Cappuzzello. It is a large acceptance (50 msr) and momentum (-14% , $+10.3\%$) detection system, composed of a quadrupole and a dipole magnet as well as a Focal Plane Detector (FPD). The last decade several experiments have been performed at the MAGNEX facility in a wide energy range with beams delivered by the Tandem as well as the Cyclotron accelerator of the laboratory, by the MAGNEX group as well as by external users.



Figure 2.4: *A view of the experimental hall with the dipole (center) and the Focal Plane Detector (right).*

The facility is shown in Figures 2.1 and 2.2. The quadrupole [132], manufactured by Danfysik A/S, focuses the particles in the vertical (non-dispersive) direction. The 55° dipole [133] (also manufactured by Danfysik A/S) provides the suitable dispersion and the focusing strength in the horizontal (dispersive) direction. The accepted magnetic rigidities vary from ~ 0.2 Tm to ~ 1.8 Tm, corresponding to an energy regime of the detected ions between $E \sim 0.2$ MeV/u to $E \sim 40$ MeV/u depending on their charge and mass [80]. Finally, the Focal Plane Detector (FPD) is the detection system as well as the most important part of the spectrometer. The MAGNEX FPD together with the dipole are presented in Figure 2.4, while the main features of the MAGNEX spectrometer are given in Table 2.1.

This work is a part of a project proposed by Prof. A. Pakou including several experiments in inverse kinematics [73, 74, 77–79]. The inverse kinematics measurements in spectrometers, require excellent energy and angular resolution as well as the possibility for a zero-degree measurement. MAGNEX is a powerful tool combining all these features. It should be noted that, the zero-degree measurement technique was also used in other experimental campaigns such as NUMEN (spokespersons: F. Cappuzzello, C. Agodi) [134–136] in relation to double charge-exchange reactions.

Table 2.1: Main characteristics of the MAGNEX spectrometer [80].

Parameters of the quadrupole and dipole	
Maximum field strength of the quadrupole	5 Tm ⁻¹
Radius of the quadrupole aperture	20 cm
Effective length of the quadrupole	20 cm
Maximum field of the dipole	1.15 T
Bending angle of the dipole	55°
Bending radius of the dipole ρ	1.60 m
Minimum bending radius of the dipole ρ_{min}	0.95 m
Maximum bending radius of the dipole ρ_{max}	2.35 m
Main characteristics of the MAGNEX spectrometer	
Maximum magnetic rigidity	1.80 Tm
Horizontal angular acceptance	-5.2°, +6.3°
Vertical angular acceptance	-7.2°, +7.2°
Maximum solid angle	50 msr
Momentum acceptance	-14.0%, +10.3%
Momentum dispersion	3.68 cm/%
Central path length	5.96 m
Focal Plane rotation angle	59.2°
Focal Plane height	20 cm
Focal Plane length	92 cm
Position resolution of the FPD (FWHM)	0.6 mm
Angular resolution of the FPD (FWHM)	0.3°
Mass resolution	0.6%
Energy loss resolution of the Focal Plane	6.3%

The magnetic field values of the MAGNEX dipole and quadrupole used in our experiment were calculated using the COSYSetup program [137]. In particular, putting as an input the reaction parameters: mass and energies, and the relative momentum δ , the program searches for the appropriate settings of the magnetic fields among a set of tabulated values, calculated for several configurations [89]. The quadrupole and dipole field intensities were measured by probes inserted in the central region of the facility. In case of the elastic scattering measurements three different magnetic settings (EL1, EL2, EL3) were applied at each energy in order to measure

the complete energy (angular) range of the elastically scattered lithium ions. Overlapping regions among sets EL1-EL3 ensured the consistency between different sets. The magnetic settings for elastic scattering as well as the breakup runs are presented in Table 2.2.

Table 2.2: Magnetic settings for each run of the experiment. In the fourth and fifth column appear magnetic fields B_Q and B_D for the quadrupole and dipole magnets, respectively. Last, in the sixth column we give the magnetic rigidity $B\rho$.

Measurement	E (MeV)	Set	B_Q (T)	B_D (T)	$B\rho$ (Tm)
Elastic Scatt.	29	EL1	0.35205	0.378030	0.604848
Elastic Scatt.	29	EL2	0.31204	0.335420	0.536672
Elastic Scatt.	29	EL3	0.28307	0.301480	0.482368
Elastic Scatt.	25	EL1	0.31676	0.340510	0.544816
Elastic Scatt.	25	EL2	0.29148	0.311140	0.497824
Elastic Scatt.	25	EL3	0.26282	0.277660	0.444256
Elastic Scatt.	20	EL1	0.29346	0.313560	0.501696
Elastic Scatt.	20	EL2	0.26255	0.277090	0.443344
Elastic Scatt.	20	EL3	0.24026	0.251260	0.402016
Elastic Scatt.	16	EL1	0.26576	0.280780	0.449248
Elastic Scatt.	16	EL2	0.23624	0.246730	0.394768
Elastic Scatt.	16	EL3	0.21440	0.221940	0.355104
Breakup	29	BU	0.29875	0.322060	0.515296
Breakup	25	BU	0.28138	0.297345	0.475752
Breakup	20	BU	0.25465	0.267932	0.428691

2.2.1 The Focal Plane Detector

As it was already mentioned, the Focal Plane Detector (FPD) [80, 84, 85] is a key element of the spectrometer. The FPD of MAGNEX was developed in collaboration with GANIL [138] and consists of a proportional drift chamber and a wall of 60 stopping silicon detectors. The drift chamber includes five sections, with five proportional counters, four of which are position sensitive. The FPD drift chamber is confined by a stainless steel vessel without intermediate foils but, with a thin entrance Mylar window. Thus, the detection threshold for heavy ions is limited to about 0.5 MeV/u. The Mylar window is 92 cm wide and 22 cm high with a typical thickness of some microns (1.5 μm for the present experiment). Twenty metallic wires each

one with a diameter of 0.5 mm support the entrance window. The space between two metallic wires is 10 mm. It should be noted that the entrance surface of the FPD is installed at an angle of 59.2° in respect to the central trajectory. This offers a reduction to the chromatic aberrations [80, 86].

Regarding the drift chamber of the FPD, the gas active volume is $(136 \times 20 \times 9.6)\text{cm}^3$ with a cathode plate below and a Frisch grid above. The last one consists of ten gold-plated tungsten wires, $50\text{ }\mu\text{m}$ thick, spaced 5 mm between centers. According to calculations, the shielding efficiency of the grid, with respect to anode wires installed 2 cm above, is $\sim 89\%$. The uniformity of the electric field between the Frisch grid, connected to the ground, and the cathode, is guaranteed by a partition grid consisted of several rectangular rings parallel to the cathode. The efficiency of the detector due to the presence of these rings is about 98.6%. The gas normally used is isobutane while the gas pressure at the present experiment was ~ 14.8 mbar. The pure isobutane gas (99.95% purity) ensures the stability of the gain, the good localization of the avalanche, and the fast drift velocity [80].

The FPD proportional drift chamber is a single unit, divided in five sections without intermediate foils. The five sections are: four Drift Chambers (DC1, DC2, DC3, DC4) and one proportional counter (PC). Each of the DC counters is made of a unique amplifying wire, while for the PC eight wires are connected in common. Both DCs and PCs are gold-plated tungsten wires located 2 cm above the Frisch grid. The DC wires have diameters of $20\text{ }\mu\text{m}$ while the PC ones $100\text{ }\mu\text{m}$. The high-voltage applied to the wires ($\sim 800\text{ V}$ in our case) is provided by a unique power supply. For each of the DC counters, a set of 224 independent induction pads is located 0.5 cm above. The entire strip patterned electrode is printed on a circuit board. Each strip is 0.8 cm long and 0.59 cm wide and separated by $100\text{ }\mu\text{m}$ from its neighbor. The use of these position-sensitive DC counters is a very good solution to the determination of the coordinates inside the Focal Plane Detector and thus useful for the ray-reconstruction. A schematic representation of the focal plane detector with the DC and PC wires is presented in Figure 2.5 while a view of these wires as well as a part of the induction pads are presented in Figure 2.6.

The last part of the Focal Plane Detector is the wall of 60 silicon pads. These silicon detectors are arranged in 3 rows and 20 columns (Figure 2.6). The silicon columns are mounted orthogonally to the MAGNEX optical axis. The edges of the detectors are vertically overlapped by 1 mm in order to minimize the dead spaces between them. Each detector has a thickness of $500\text{ }\mu\text{m}$. The height of each detector is 7 cm while the width is 5 cm, creating an active area of 35 cm^2 . The total active area of the wall is about 0.2 m^2 . It should be noted that

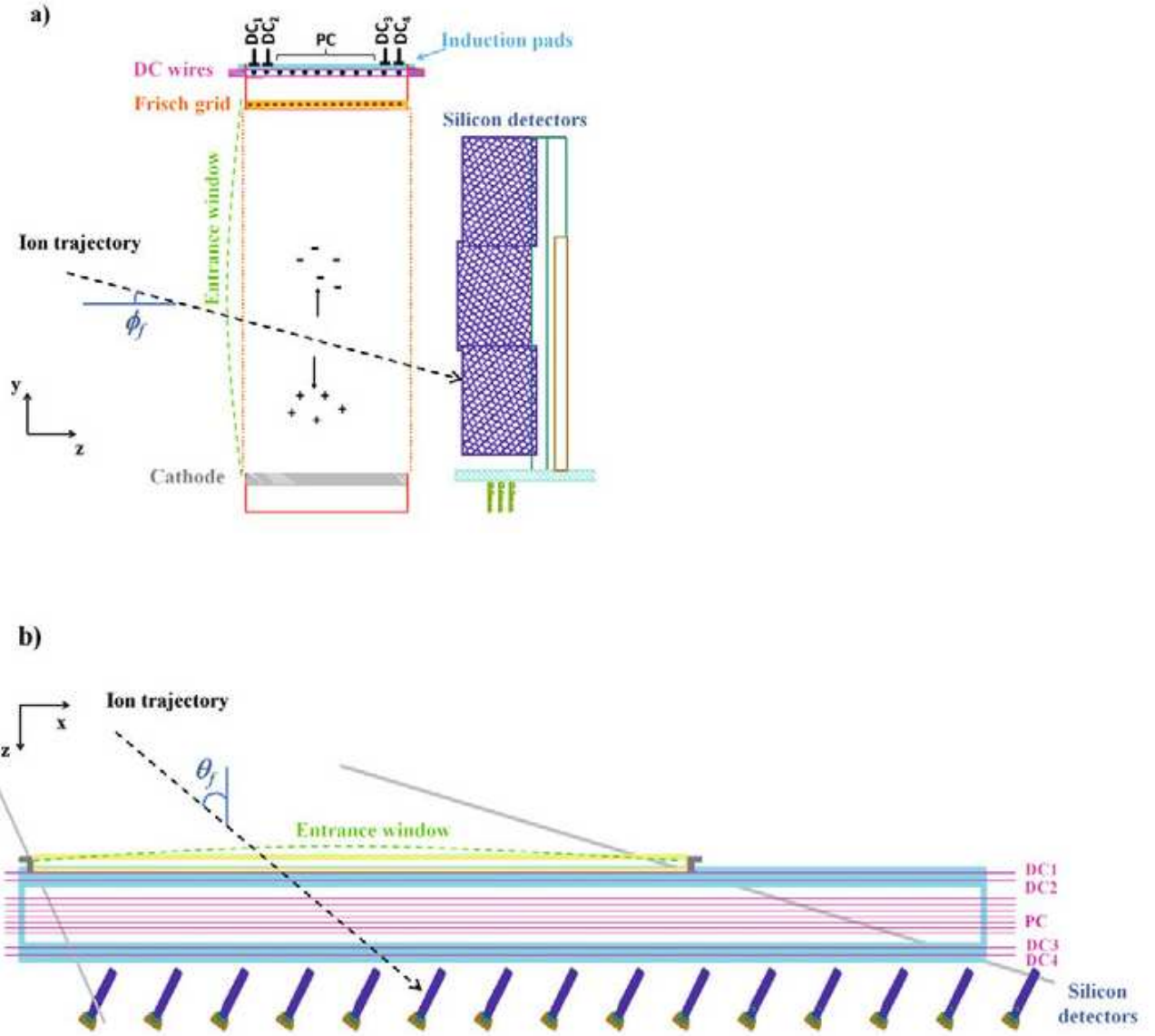


Figure 2.5: A schematic representation of the focal plane detector: a) side view, b) top view. Figure from ref. [84]

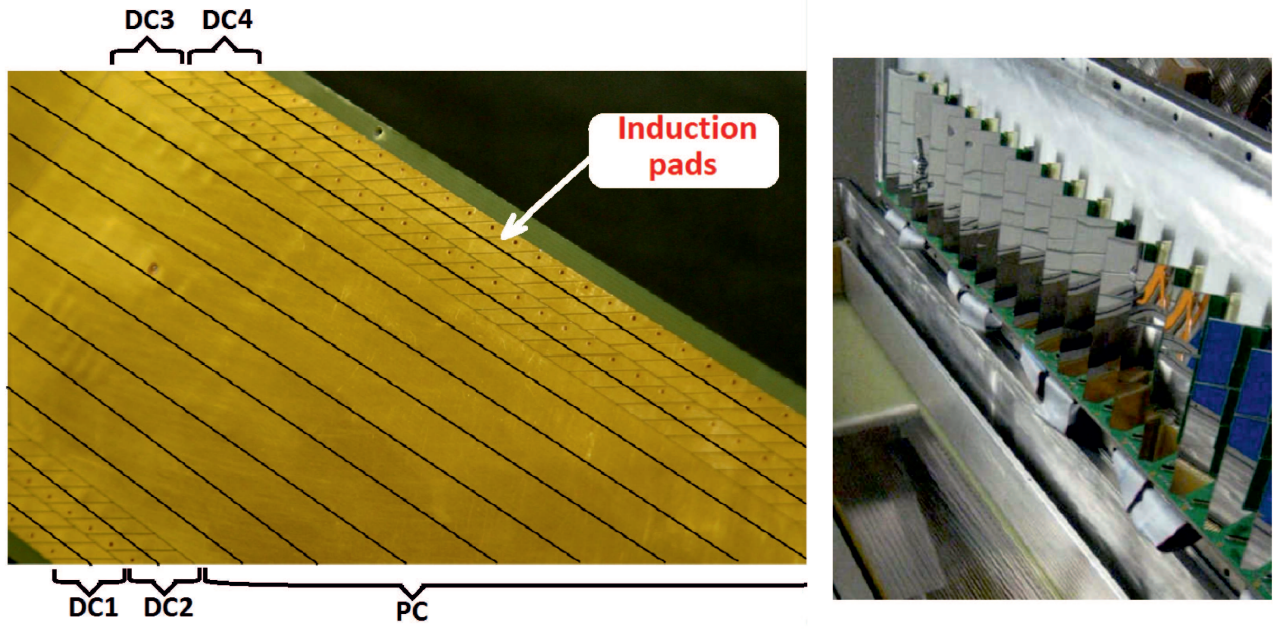


Figure 2.6: *Left panel: A view of the DC and PC wires as well as a part of the induction pads (figure from ref. [81]). Right panel: A part of the silicon detectors wall (photo from ref. [81]).*

the silicon wall is 1.5 cm away from the last DC (DC4). This distance was selected after the appropriate electrostatic calculations in order to minimize problems of the uniformity of the drift field [80, 88].

The various ejectiles passing through the MAGNEX quadrupole and dipole, are directed into the Focal Plane gas chamber, forming ionized atoms and electrons along their track. Under the influence of a uniform electric field, the electrons drift towards the Frisch grid with constant velocities. In the present experimental conditions, these velocities are about $5 \text{ cm}/\mu\text{s}$. Beyond the Frisch grid the electrons are accelerated in the presence of an electric field. This field becomes much stronger approaching the DC or PC wires leading to secondary ionizations. Thus, the number of electrons is increased by a factor of about 150 in the present conditions. The avalanche produces a signal proportional to the energy loss by the ions in each section of the FPD, providing the measurements of ΔE_{DC1} , ΔE_{DC2} , ΔE_{PC} , ΔE_{DC3} and ΔE_{DC4} for each event. These signals are shaped and amplified by the appropriate charge-sensitive pre-amplifiers. The logic outputs, extracted only for the DC wires, are used for the measurement of the horizontal position as follows. The electron avalanche around each DC wire induces a charge on the nearest induction pad. The signals collected by these pads are shaped and pre-amplified by an analog multiplexed read-out system based on 16-channels GASSIPLEX chips which is mounted on the upper part of the FPD. The multiplexed signals from each

DC are readout and digitally converted by the appropriate modules. The center of gravity of the charge distribution at each DC section is then extracted. By exploiting the available information of the position sensitive DCs, the measured centroid is converted to the horizontal position X_{DC1} , X_{DC2} , X_{DC3} , X_{DC4} in meter units [85]. These four independent measurements allow the determination of the horizontal position (χ_f) and the horizontal angle (θ_f) of the ion track at the spectrometer focal plane (Figure 2.5(b)).

The vertical position and angle are measured by a drift time method. In particular, when the charged particles reach the silicon wall a START timing signal is created (we assume that the drift time of the ion inside the FPD is negligible). On the other hand, the electrons detected at DCs give the STOP signal. Since the velocity of the electrons inside the gas is constant, the time interval between the START and STOP signals is used for determining the vertical positions Y_{DC1} , Y_{DC2} , Y_{DC3} , Y_{DC4} initially in arbitrary units and finally via a calibration to meters. For this purpose four standard TAC + ADC read-out electronics chains are used (see Figure 2.7). Thus, the vertical position (y_f) and vertical angle (φ_f) of the ion track at the focal plane are determined (Figure 2.5(a)). In this respect, taking into consideration the horizontal and vertical position, measured using the technique mentioned above, the ion track for each event is completely mapped. The operating principle of the MAGNEX FPD is also presented in Figure 2.5.

Finally, the residual energy (E_r) of the ions after crossing the gas is measured by the 60 silicon detectors. After the charge pre-amplifiers, the signals are sent to 16-channel shaping amplifiers, which provide the useful spectroscopic and timing outputs (see Figure 2.7). The information of both the energy loss (ΔE) inside the gas and the residual energy (E_r) allow the particle identification via the standard ΔE - E (or similar) technique. The performance of the FPD was studied in details in refs. [80, 82, 84].

2.2.2 Trajectory Reconstruction

A very important step for an accurate analysis of the data acquired at the MAGNEX facility is the trajectory reconstruction technique. In particular, it is necessary to find a relation between the initial coordinates of the particles and those measured at the focal plane (final coordinates). By calculating the transport matrices and thus the inverted transport matrices, one can reconstruct the initial particle coordinates from the measurement of the final ones by the FPD. In this context, the MAGNEX group has developed the appropriate ray reconstruction algorithms in order to accomplish this goal with sufficient precision even

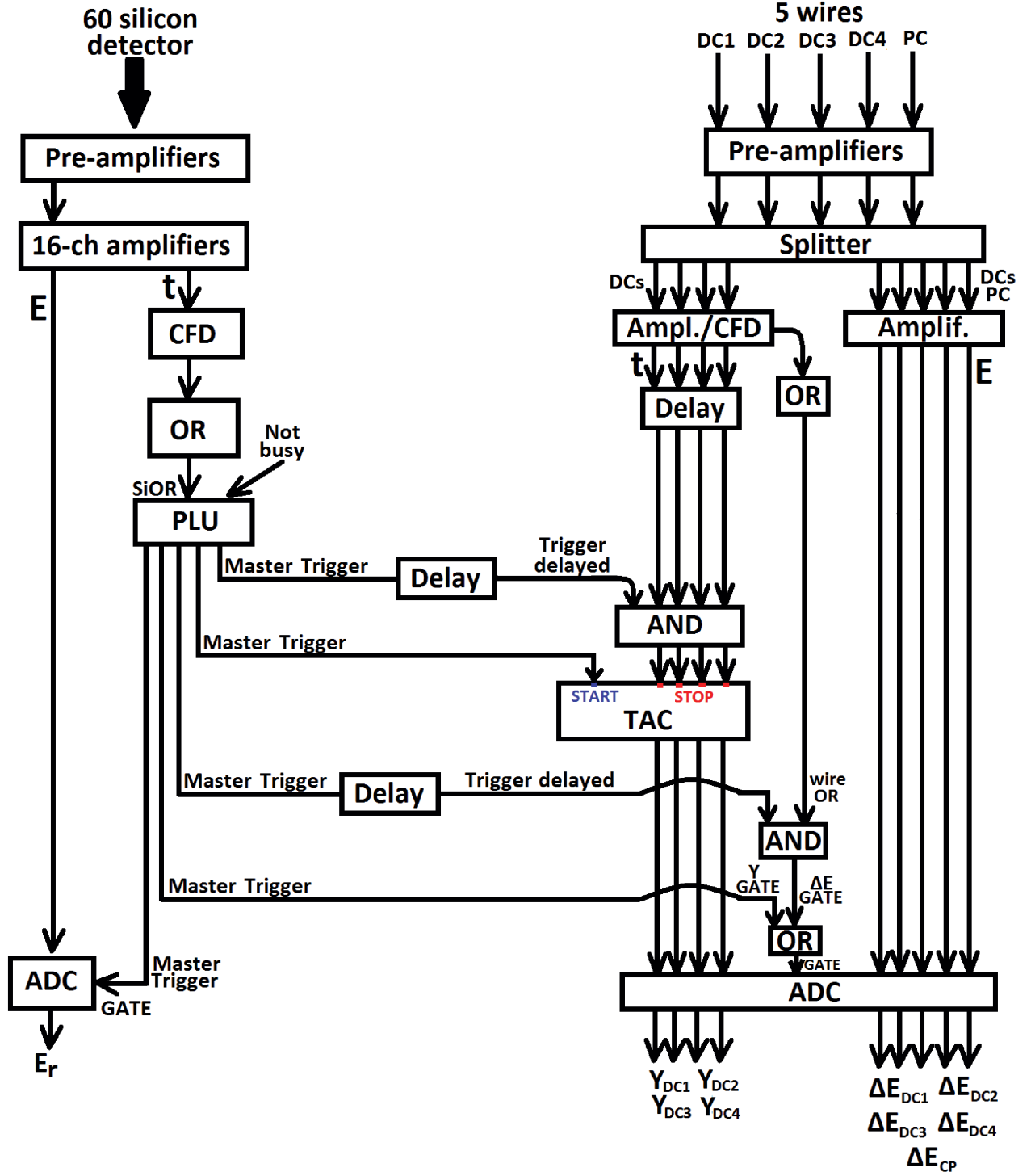


Figure 2.7: Schematic diagram of the read-out electronic chain of the residual energy (E_r), the energy loss (ΔE) as well as the Y position measurements [89, 139].

for a large acceptance spectrometer like MAGNEX. The main features of these algorithms are given below.

Following the prescription described in Ref. [80, 140], the motion of an ion beam under the action of a magnetic force can be represented as a general phase space mapping, which connects the final position P_f to the initial one P_i as follows:

$$F : P_i(\chi_i, \theta_i, y_i, \varphi_i, l_i, \delta_i) \rightarrow P_f(\chi_f, \theta_f, y_f, \varphi_f, l_f, \delta_f) \quad (2.1)$$

In this equation, l is the trajectory length, χ and y are the horizontal and vertical coordinates while, θ and φ are the horizontal and vertical angles respectively. The parameter $\delta=(p-p_0)/p_0$, is referred to the fractional momentum, where p and p_0 are the actual and reference momentum respectively. The mapping F , is represented as a matrix and it depends on the general spatial distribution of the magnetic fields. The Eq. (2.1) could be written in a less compact form as follows:

$$\begin{aligned} \chi_f &= F_1(\chi_i, \theta_i, y_i, \varphi_i, l_i, \delta_i) \\ \theta_f &= F_2(\chi_i, \theta_i, y_i, \varphi_i, l_i, \delta_i) \\ y_f &= F_3(\chi_i, \theta_i, y_i, \varphi_i, l_i, \delta_i) \\ \varphi_f &= F_4(\chi_i, \theta_i, y_i, \varphi_i, l_i, \delta_i) \\ l_f &= F_5(\chi_i, \theta_i, y_i, \varphi_i, l_i, \delta_i) \\ \delta_f &= \delta_i \end{aligned} \quad (2.2)$$

It should be noted that, due to the conservation of the momentum modulus for static magnetic fields in the absence of energy degrading materials, the δ parameter is invariant. Also, the l_i parameter is consider as constant for thin targets. In addition, inverting the Eq. (2.1) or equivalently, Eq. (2.2), with respect to the initial parameters, we can obtain the momentum vector at the target position. This inversion gives:

$$F^{-1} : P_f \rightarrow P_i \quad (2.3)$$

The most convenient way to solve the problem of the trajectory reconstruction is to formulate it in terms of the measured parameters. As it was already mentioned, $\delta_f=\delta_i=\delta$ and also, l_i is a constant variable. Thus, the total number of parameters involved in the above equations is 10 ($\chi_i, \chi_f, \theta_i, \theta_f, y_i, y_f, \varphi_i, \varphi_f, l_f, \delta$). Five of them are the measured quantities while the rest are the reconstructed quantities. The set of the measured parameters could be written as: $Q_f=(\chi_f, \chi_i, \theta_f, y_f, \varphi_f)$ while the set of the reconstructed one as: $Q_i=(\theta_i, y_i, \varphi_i, l_f, \delta)$. The χ_i parameter is the initial horizontal position (target) and can be neglected assuming an ion

beam horizontally focused on the target. Finally, the quantities χ_f , θ_f , y_f , φ_f are measured by the focal plane detection array. Thus, Eq. (2.3) becomes:

$$G^{-1} : Q_f \rightarrow Q_i \quad (2.4)$$

Other commonly used parameters such as energy or scattering angle can be expressed in terms of the experimental or reconstructed parameters. As an example, the scattering angle in the laboratory frame can be reconstructed by the horizontal and vertical angle according to basic geometrical relations.

Unfortunately, due to the large acceptance of MAGNEX, high order Taylor expansions are required for an accurate solution of (2.4). In order to solve this equation, a precise technique was developed at the Michigan State University for another spectrometer (S800) [141]. The technique is based on the differential algebra formalism and allows a reliable calculation of the high-order transport matrices, avoiding long ray-tracing processes. The technique was incorporated in a computer program called COSY INFINITY [142]. This program allows the user to insert some specific information of the experiments. It should be noted that the inclusion of the magnetic fields should be represented by regular functions of the position coordinates in order to avoid problems at the calculation of high-order derivatives. In order to determine the appropriate magnetic field functions, mathematical interpolations may be required. Thus, special attention is required especially at the magnet fringes where the magnetic field may change rapidly [132, 133, 143, 144]. The interpolated magnetic field function, apparently, has to be compatible with Maxwell equations.

The members of the MAGNEX group have developed a simulation code in order to check the accuracy of the reconstruction. This simulation is based on the 2-body reaction kinematics while it takes into account the MAGNEX geometry. Comparing the experimental data for an identified reaction process with the simulated ones we can verify the reliability of the reconstruction. In case of unsatisfactory results, small adjustments at the magnetic field values or the geometry parameters may be applied in order to improve the reconstruction. The next step is the calculation of the appropriate matrices by the COSY program taking into account the magnetic fields [132, 133, 143, 144] as well as the geometry of the quadrupole [132], the dipole [133] and the FPD [80, 84, 85]. These matrices and other experimental details, together with the relevant algorithms developed by the MAGNEX group, are fed to the CHIMERACQ program in order to generate the reconstructed data. The last ones include both the measured and the reconstructed parameters. The analysis of these data can be performed either with PAW [145] or ROOT [146, 147] analysis packages.

It is obvious that the trajectory reconstruction in a large acceptance spectrometer, such as MAGNEX, is a complicated procedure. The reliable description of the magnetic fields, the accurate knowledge of the MAGNEX geometry and finally the precise measurement of the Q_f vector by the focal plane detector are required for an accurate trajectory reconstruction. Thanks to the relevant algorithms and simulations developed by the MAGNEX group, the data analysis is feasible by using commonly used parameters.

2.3 The Silicon detector at 5 degrees

A surface barrier silicon detector (semiconductor detector) is based on a p-n junction. This junction is the border between a p-type zone, doped with electron-acceptor impurities and an n-type zone, doped with electron-donor impurities. Both sides are electrically neutral but, n-type zone has excess of electrons while p-type zone has excess of holes. In this respect, the free electrons from the n-type material begin to diffuse across the p-n junction between the two materials and fill some of the holes in the p-type material. This procedure stop when the system equilibrates and that leads to the formation of a charge-free depletion region between the p and n type zone. When an incident radiation passes through the depletion region, pairs of holes and electrons are created. Under the influence of the electric field, electrons and holes move towards the electrodes creating a pulse proportional to the total number of electrons - holes pairs. So, this pulse is proportional to the energy loss of the incident particle inside the detector. The most common type of silicon detectors used for measuring the energy of charged particles is the "surface barrier silicon detectors". These detectors are based on crystalline semiconductor (silicon) and they have a high resolution as well as the advantage to be operated in room temperature [97, 148–150].

As it was already mentioned, at the breakup measurement, the alpha particles were detected by the spectrometer while, the second breakup fragment, deuterons, were detected in a surface barrier silicon detector, set at $\theta_{lab} = 5^\circ$, spanning the angular range between 4.17° and 5.83° . The main characteristics of the detector are presented in Table 2.3.

A circular collimator with a diameter of 6 mm was placed in front of the detector defining an experimental active area of 28.3 mm^2 . Also, the silicon detector was masked, against elastic scattering deterioration, with 43.6, 30.8 and $25.9 \text{ }\mu\text{m}$ thick tantalum foils respectively for the 29, 25 and 20 MeV measurements. These foils absorbed the heavy particles but allowed protons and deuterons to go through. The energy loss of deuterons and protons inside the Tantalum foils was calculated via the LISE++ [151, 152] program and the results are presented in Figure

2.8.

Table 2.3: Main characteristics of the 5° surface barrier silicon detector as well as information about its setup.

Serial No.	47-128 A
Model No.	EA-017-050-2000-S
Sensitive Thickness	$\geq 2000 \mu\text{m}$
Operating Bias	300 V
Active area	50 mm^2
Diameter of the active area	$\sim 8 \text{ mm}$
Diameter of the collimator	6 mm
Distance from the target	20.7 mm
Angular range	4.17° - 5.83°

2.4 Electronics of the experiment

The read-out electronic chain used in the elastic scattering measurement was already described in Section 2.2.1, while a relevant schematic diagram is illustrated in Figure 2.7. In this diagram we can see the path of the signals from each detection device to the Analog to Digital Converter (ADC) for the parameters of the residual energy (E_r), the energy loss (ΔE_{DC1} , ΔE_{DC2} , ΔE_{DC3} , ΔE_{DC4} , ΔE_{PC}) as well as the vertical position (Y_{DC1} , Y_{DC2} , Y_{DC3} , Y_{DC4}). The master trigger is also presented in Figure 2.7. As an example, the master trigger for the measurement of the ΔE was provided by a logical AND between the output of a logical OR among the 60 silicon detectors (SiOR) and a logical OR among the DC wires (wireOR) [139].

Regarding the breakup measurement, the signal of the 5° detector was sent to an ORTEC pre-amplifier, where its output was fed as an input to an ORTEC amplifier providing the energy signal. The amplified signal was also fed to a CAEN Fast Discriminator providing the logical signal. The master trigger for the hardware coincidence was provided by an AND between the output of a logical OR among the 60 silicon detectors (SiOR) and the logical signal of the silicon detector at 5° .

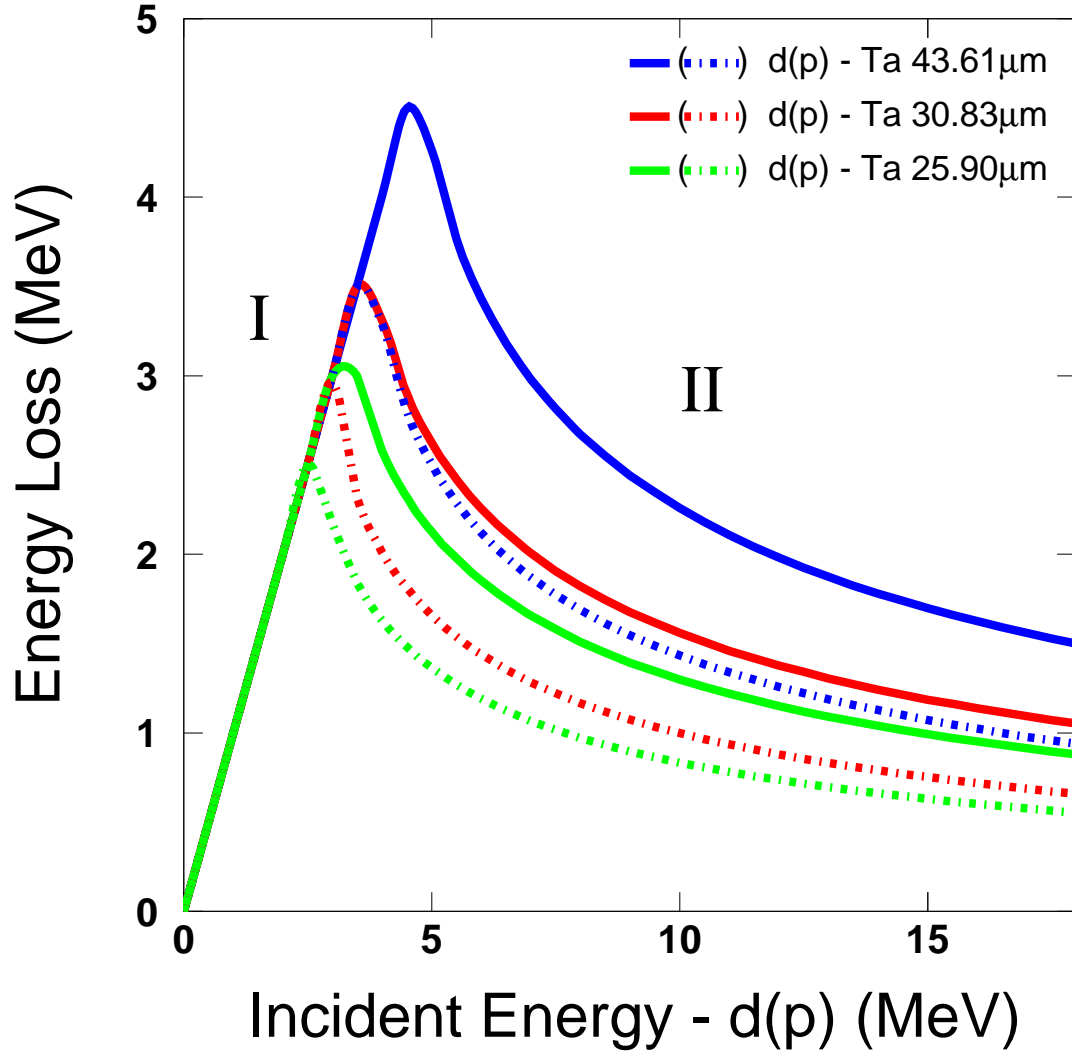


Figure 2.8: Energy loss inside the Tantalum foils used in the present experiment as a function of the deuterons and protons incident energy. The energy loss for deuterons and protons was calculated via the LISE++ program [151, 152] and the results are denoted with the solid and dotted-dashed curves, respectively. At region **I**, the Tantalum foil absorbs all the particle energy, while at region **II** the particles are allowed to go through the foil.

2.5 Target details

The targets were mounted on a target ladder, PC controlled, installed inside the chamber. Two different target ladders were used in the experiment. The target ladder L1 was used at the measurements of 29 and 25 MeV while, the ladder L2 was used at the measurements of 20 and 16 MeV. L1 and L2 are shown in Figure 2.9 with all the details of the targets. By changing the height of the ladder, any one of the targets could be positioned in the beam. At Figure 2.9 we can see CH₂ targets of different thicknesses for the main measurements and ¹²C targets useful for estimating the background due to carbon contamination at the CH₂ targets. Also, the Quartz, the Allumina and the empty frame were used for the alignment of the beam while, the ¹⁹⁷Au target was used for the solid angle determination as well as for energy calibration purposes related with the GLORIA telescope [75]. The targets used for the elastic scattering as well as the breakup measurements are listed in Table 2.4.

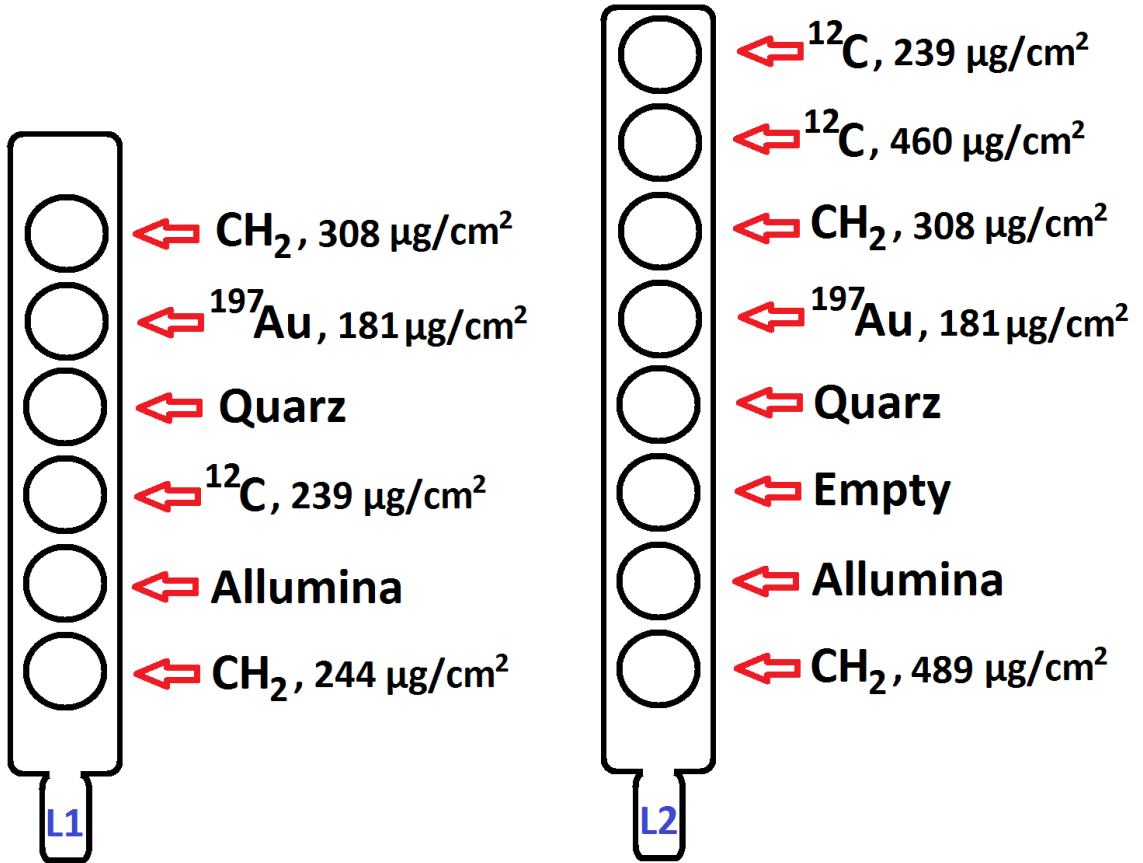


Figure 2.9: Schematic representation of the target ladders L1 and L2.

Table 2.4: Thicknesses of the CH₂ and Carbon targets used for the elastic scattering and the breakup measurements

Measurement	E (MeV)	Ladder	CH ₂ ($\mu\text{g}/\text{cm}^2$)	¹² C ($\mu\text{g}/\text{cm}^2$)
Elastic Scatt.	29	L1	244	239
Elastic Scatt.	25	L1	244	239
Elastic Scatt.	20	L2	308	239
Elastic Scatt.	16	L2	308	239
Breakup	29	L1	308	239
Breakup	25	L1	308	239
Breakup	20	L2	489	460

Chapter 3

Data Reduction

This chapter includes the data reduction procedure for both the elastic scattering and breakup data. The first step of the analysis, to be described in section 3.1, includes the calibration of the horizontal and vertical positions of the spectrometer, as well as the energy calibration of the silicon detector used for the breakup measurement. The next step includes the particle identification for both elastic scattering and breakup, by using the reconstructed data, to be described in section 3.2. Finally, the deduction of the differential cross sections for the elastic scattering and the breakup data is described in sections 3.3 and 3.4 respectively. The data analysis was performed using the program PAW [\[145\]](#).

3.1 Calibration procedure

This section includes the calibration procedures which leads to the energy calibration of both MAGNEX and the 5 degree silicon detector, as well as to the (θ, φ) determination for MAGNEX. The calibration procedure for the MAGNEX spectrometer concerns the horizontal and vertical positions X and Y (subsection 3.1.1). X leads to the kinetic energy calibration, while X and Y to the (θ, φ) determination. The energy calibration of the detector at 5° will be given in subsection 3.1.2.

3.1.1 MAGNEX calibration

Horizontal position calibration

As it was already mentioned in the previous chapter, the horizontal positions X_{DC1} , X_{DC2} ,

X_{DC3} , X_{DC4} can be obtained as a response of four sets of 224 induction pads, located 5 mm above the DC wires. This is the result of an avalanche of electrons creating a distribution, the center of which is defined by using an algorithm, developed previously by the MAGNEX group [80, 85, 89]. The relative calibration of the pads was obtained by sending four negative pulses via a pulser to the wires, with amplitudes of 1.0 V, 1.5 V, 2.0 V and 3.0 V and the response of each pad was plotted as a function of a reference pad (relative calibration). A linear correlation was obtained. The next step was the determination of the position of the avalanche of an event along a DC wire, which was obtained by using the calibration results, it was possible to convert the measured position from the pad number variable to the horizontal positions X_{DC1} , X_{DC2} , X_{DC3} and X_{DC4} in meter units. Since the Z coordinate is accurately defined for each DC wire by the construction of the focal plane detector, the ion track in the **x-z** plane can be obtained (see Figure 2.5(b)) and therefore the extraction of the horizontal position (χ_f) at the spectrometer focal plane. Subsequently, the horizontal angle (θ_f) can be determined by the slope of the ion trajectory in the **x-z** plane.

Vertical position calibration

The vertical position calibration was based on the Y spectra obtained by the different DC wires. A typical Y spectrum for the DC2 wire is shown in Figure 3.1. The observed minima in this spectrum, are due to the shadows of the horizontal wires which support the entrance Mylar window. A calibration of the vertical position was feasible by plotting the known positions of the wires in meter units as a function of the channel of each minimum, assuming a linear correlation. Thus, an absolute calibration of the Y_{DC1} , Y_{DC2} , Y_{DC3} and Y_{DC4} parameters was obtained. Since the Z coordinates for the four different DC wires are known, the linear ion track in the **y-z** plane was defined (see Figure 2.5(a)). Therefore, the vertical position (y_f) and vertical angle (φ_f) of the ion track at the focal plane were determined.

3.1.2 Silicon detector calibration

The energy calibration of the silicon detector set at 5° was performed via a triple alpha source (^{239}Pu , ^{241}Am , ^{244}Cm) and a pulser generator. In particular, the pulser was calibrated through the alpha source and the detector was calibrated via the pulser in a large energy range assuming the following formula:

$$Energy = A * (channel) + B \quad (3.1)$$

where A and B are parameters which are obtained by the fit.

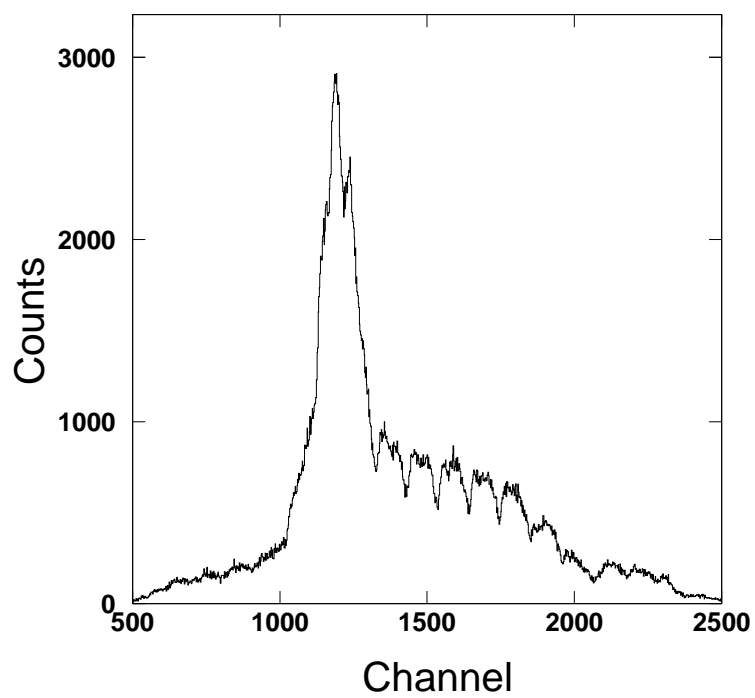


Figure 3.1: *A typical Y spectrum for the DC2 wire. The minima are due to the horizontal metallic wires which support the entrance window of the MAGNEX FPD.*

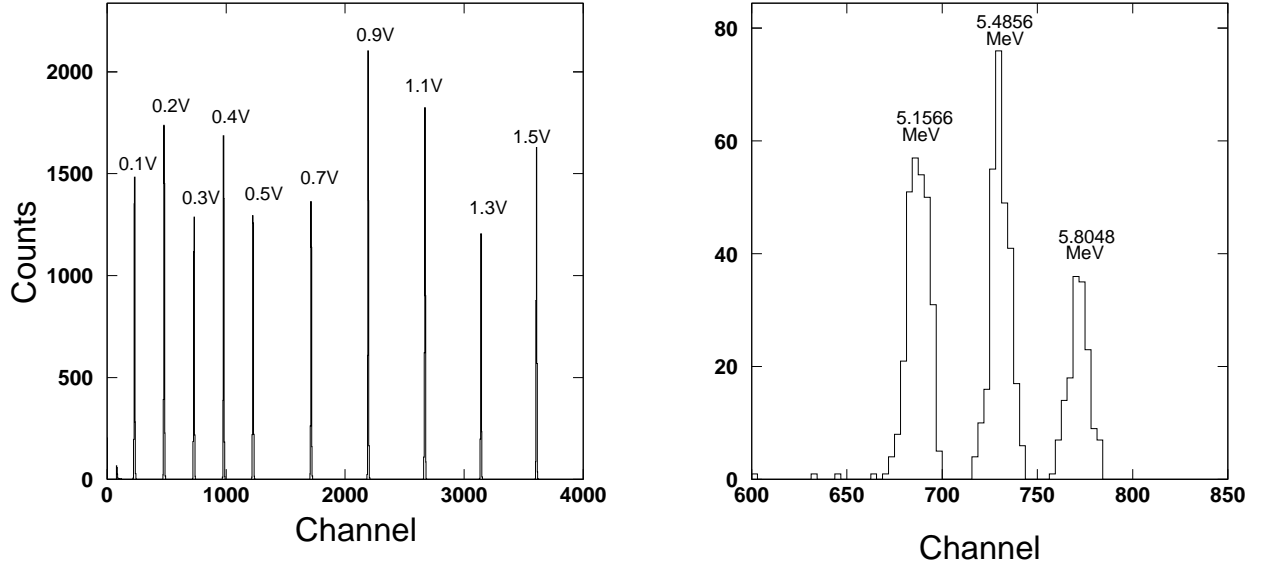


Figure 3.2: Calibration spectra collected with the silicon detector at 5° . Spectra with a pulser walkthrough and a triple alpha source are presented in left and right panel respectively. The amplitudes of the pulser as well as the energies of the alpha peaks are denoted in the figure.

It should be noted that, the triple alpha source energies are: 5.1566, 5.4856 and 5.8048 MeV for the alpha decay of the ^{239}Pu , ^{241}Am and ^{244}Cm , respectively. The amplitudes of the pulses, sent by the pulser generator, were: 0.1 V, 0.2 V, 0.3 V, 0.4 V, 0.5 V, 0.7 V, 0.9 V, 1.1 V, 1.3 V and 1.5 V spanning a large energy range between ~ 200 and ~ 3600 channels or equivalently, ~ 1.5 to 27.3 MeV. The calibration spectra with the pulser as well as the triple alpha source are illustrated in Figure 3.2.

3.2 Particle identification

The second step of the data analysis is an accurate particle identification. For both the elastic scattering and the breakup measurements the ion identification for recoils detected in the spectrometer, was based on the standard ΔE -E (or similar) technique.

Since the MAGNEX is a detection system with several measured quantities, the ΔE parameter can be deduced either from the DC wires or the PC ones. In our case, the ΔE measurement was obtained by the PC wires, since this measurement was of better quality than the ones obtained by the DC wires. A correction at the measurement of ΔE should be

applied due to the inclination of the focal plane as well as the large angular acceptance of the spectrometer [84]. The event by event correction follows the formula (3.2) [88, 89, 153].

$$\Delta E_{corr} = \Delta E \frac{\cos \theta_{tilt}}{\cos \theta_f} = \Delta E \frac{\cos(59.2^\circ)}{\cos \theta_f} \quad (3.2)$$

Further on, the residual energy (E_r) was measured by the 60 silicon detectors at the end of the ion track. Subsequently the particle identification was performed by two-dimension plots ΔE - E_{res} or/and ΔE - χ_f , χ_f - E_{res} . Below we will show the reason that we can use also the last plots for particle identification.

The motion of an ion, with charge q and mass m , moving with velocity u perpendicular to a uniform magnetic field B , follows the equation below:

$$\begin{aligned} q\vec{u} \times \vec{B} &= \frac{m\vec{u}^2}{\rho} \\ quB &= \frac{mu^2}{\rho} \rightarrow B\rho = \frac{p}{q} \end{aligned} \quad (3.3)$$

where p is the momentum modulus of the ion, ρ is the radius of the ion trajectory and $B\rho$ is the magnetic rigidity. The momentum modulus can be written as:

$$p = (2mE)^{1/2} \quad (3.4)$$

where E is the kinetic energy of the particle. Furthermore, the radius ρ is related to the horizontal position χ_f . So, taking into consideration all the above, χ_f is connected to the energy by the following formula:

$$\chi_f^2 \propto \frac{m}{q^2} E \rightarrow \chi_f^2 \propto \frac{m}{Z^2} E \quad (3.5)$$

where Z is the atomic number of the detected particle. Since the energy loss inside the FPD is small, Eq. (3.5) can be approximately written as:

$$\chi_f^2 \propto \frac{m}{Z^2} E_r \quad (3.6)$$

Thus, the identification of the various ejectiles is also feasible via the $\Delta E_{corr} \% \chi_f$ or/and the $\chi_f \% E_r$ spectra which give supplementary constraints to the ΔE - E_{res} technique, fundamental to get a high mass resolution. This technique is also described in Refs. [83, 88, 89, 153].

3.2.1 Identification of the elastic channel

As it was already stated in Chapter 2, the elastic scattering measurement was performed in three different runs for each energy (EL1, EL2, EL3), in order to measure the complete

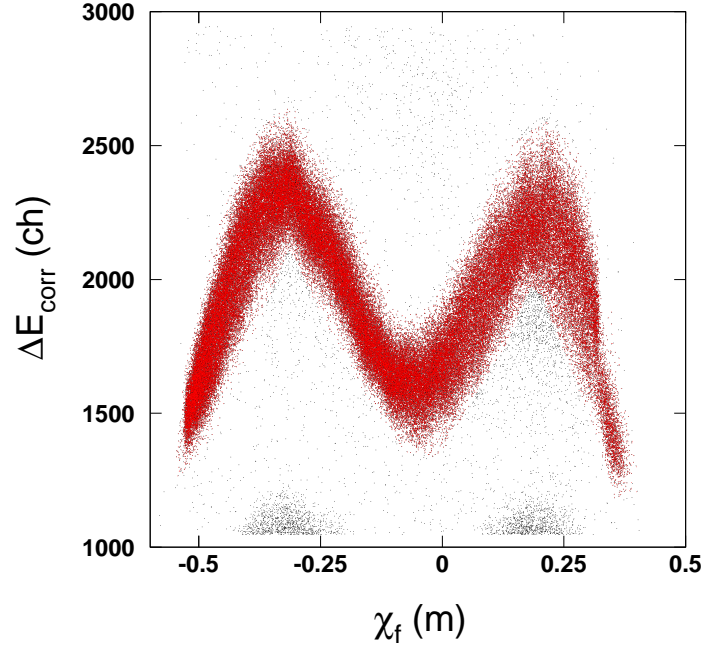


Figure 3.3: A typical two dimensional $\Delta E_{corr} \% \chi_f$ correlation plot. The spectrum refers to an elastic scattering run at the projectile energy of 29 MeV, using the EL2 set of magnetic fields (see Table 2.2). The lithium ions are denoted with the red dots.

energy and therefore angular range of the elastically scattered lithium ions. The identification of these ions was performed by a graphical selection of the lithium contour in the $\Delta E_{corr} \% \chi_f$ spectra (see Figure 3.3). The next step was the calculation of the matrices useful for the reconstruction of each run as well as the quality control of the procedure via the simulation programs developed by the MAGNEX group. The extraction of the reconstructed data was performed by applying the method described in 2.2.2. Since the reconstruction procedure does not take into account the energy loss inside the target, an effective beam energy was used to account for this effect (see Appendix A for details).

A typical reconstructed E- θ correlation plot for ${}^6\text{Li}+\text{p}$ at the projectile energy of 29 MeV is presented in Figure 3.4. In this figure, the reconstructed kinematical plot was obtained with the superposition of the three different runs (EL1, EL2, EL3), which are designated with different colors. A kinematical prediction, obtained by the NRV program [154], is also illustrated indicating the excellent agreement between the experimental data and the theoretical prediction. This agreement validates the accuracy of the reconstruction. It is also obvious the excellent energy and angular resolution. Furthermore, the lithium ions due to the car-

bon contamination at the CH₂ target (top flat line in Fig. 3.4) are well-separated from the ⁶Li+p elastic scattering data. Despite that, the evaluation of the carbon contamination and its subtraction from the yield obtained with the CH₂ target, was obtained by repeating the measurement with a carbon target. This correction, together with a noise background was of the order of 10-20% with main contributor the noise.

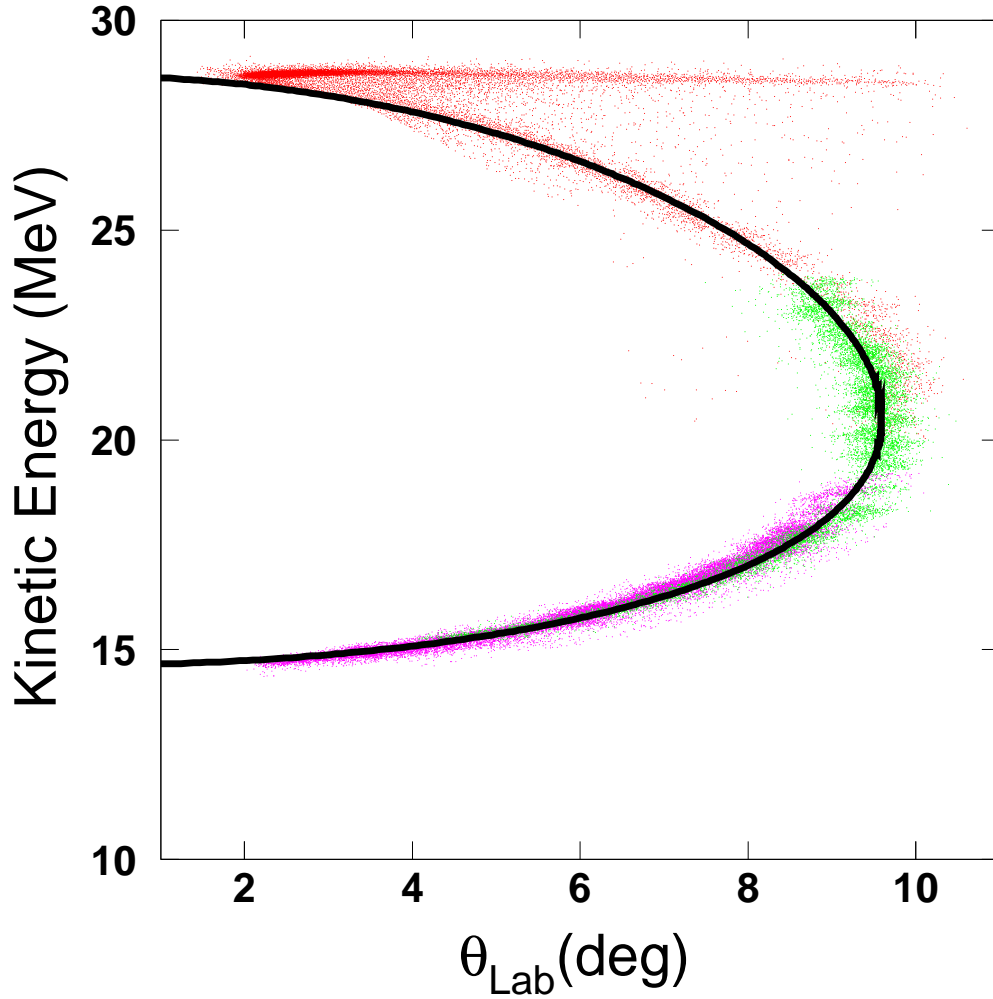


Figure 3.4: A reconstructed E - θ spectrum at the projectile energy of 29 MeV. The two kinematical solutions of the reaction, were obtained in 3 different runs with 3 sets of magnetic fields. The plot shows the superposition of these runs, designated with different colors. The black solid line represents the kinematical prediction.

3.2.2 Identification of the breakup channel

The identification of the breakup process was a more complicated procedure than in the case of elastic scattering. Exclusive yields were determined for alphas observed in the spectrometer FPD, well identified via the ΔE -E technique, combined with deuterons observed at the silicon detector at 5° . Deuterons were not resolved from protons as the detector was not a telescope and our exclusive yield spectra included both α - d and α - p coincidences. However as it will be shown below, the α - p coincidences were well resolved from α - d coincidences via kinematics.

The ^4He ions in MAGNEX were selected using the $\Delta E_{corr} \% \chi_f$ spectra (see Figure 3.5). The majority of elastic scattering events were swept out by applying the appropriate magnetic fields, allowing the detection of alphas in energy slices of 11.0 to 15.5 MeV, 8.4 to 13.3 MeV and 6.8 to 10.7 MeV for the 29, 25 and 20 MeV run, respectively. A small leftover of the lithium events was rejected by the appropriate graphical selections in the $\chi_f \% E_r$ spectra (see Figure 3.6). Applying these conditions, the ^4He ions in MAGNEX were precisely identified. The deuterons were detected in the silicon detector, set at 5° . As it was mentioned before, this detector was masked, against elastic scattering deterioration, with tantalum foils. These foils absorbed all lithiums but allowed light particles to go through. The reaction mechanisms leading to ^4He particles production, detected in MAGNEX in coincidence with light particles ($Z \leq 2$) in the detector set at 5° are the following ones:

1. $^6\text{Li} + ^1\text{H} \rightarrow ^4\text{He} + ^2\text{H} + ^1\text{H}$
2. $^6\text{Li} + ^{12}\text{C} \rightarrow ^4\text{He} + ^2\text{H} + ^{12}\text{C}$
3. $^6\text{Li} + ^1\text{H} \rightarrow ^4\text{He} + ^3\text{He}$
4. $^6\text{Li} + ^1\text{H} \rightarrow ^5\text{Li} + ^2\text{H} \rightarrow ^4\text{He} + ^1\text{H} + ^2\text{H}$

The first one is the reaction under study (projectile breakup on proton target). The presence of the second reaction (projectile breakup on carbon target) is due to carbon contamination at the CH_2 target. This contribution was of the order of 11-15% for the higher energies and affected very little the main measurement. However, the background from such events was estimated via a run with a pure carbon target (see Figure 3.7). Unfortunately, the contribution due to carbon contamination was much larger at the energy of 20 MeV, where a problem with the normalization of the data did not allowed the deduction of breakup cross sections. The reaction $^1\text{H}(^6\text{Li}, ^4\text{He})^3\text{He}$ was cut out by the magnetic fields selection. Finally, the n-stripping reaction $^6\text{Li} + ^1\text{H} \rightarrow ^5\text{Li} + ^2\text{H} \rightarrow ^4\text{He} + ^1\text{H} + ^2\text{H}$ ($Q_{value} = -3.44$ MeV) is expected to have very low probability.

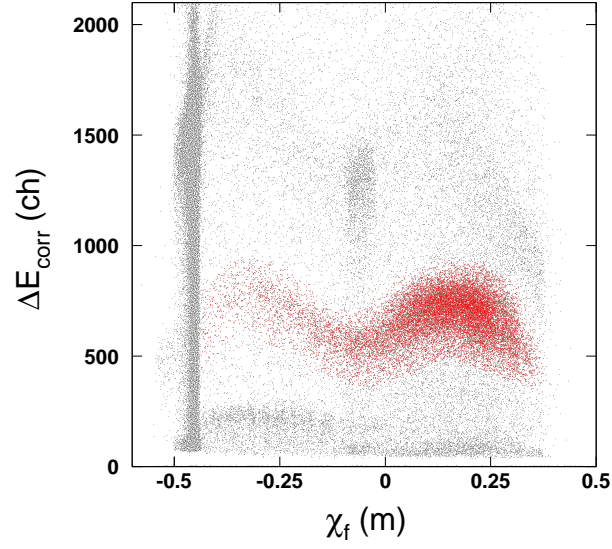


Figure 3.5: A typical two dimensional $\Delta E_{\text{corr}}-\chi_f$ correlation plot for the breakup measurement at 29 MeV. The helium ions are denoted with the red dots.

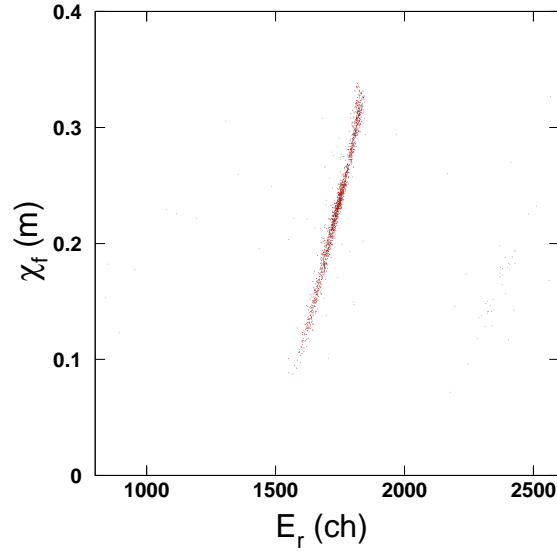


Figure 3.6: A typical two dimensional $\chi_f\%E_r$ correlation plot for a single silicon detector of the FPD wall ($S_{\text{inum}}=11$) at the energy of 29 MeV. The spectrum was obtained by applying the appropriate graphical condition of Figure 3.5. The clear ${}^4\text{He}$ ions are denoted with the red dots.

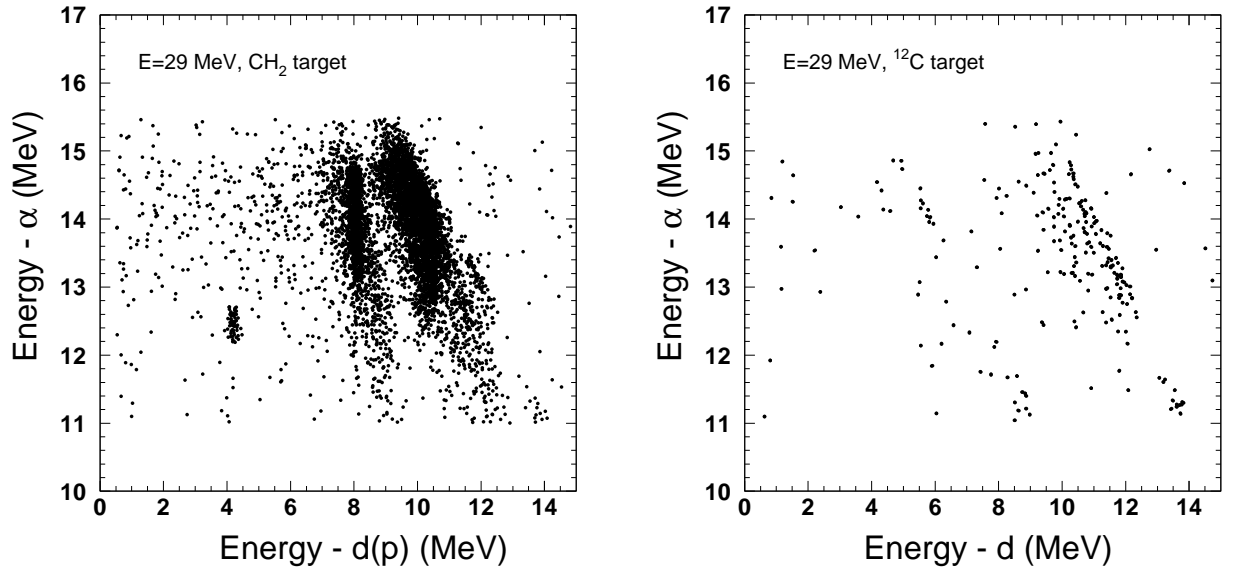


Figure 3.7: Representative two dimensional plots of the measured energy of alpha particles ($\text{Energy} - \alpha$) versus the measured energy of deuterons or protons ($\text{Energy} - d(p)$) at the beam energy of 29 MeV (4.83 MeV/u). Alphas were recorded in the MAGNEX spectrometer at an angular range of $\theta_{lab} = 0$ to 10° , while deuterons and the recoiling protons in a silicon detector set at $\theta_{lab} = 5^\circ$. The plot in relation with the CH₂ target measurement is presented at the left panel while the plot from the ¹²C run is presented at the right panel.

A Monte Carlo three-body simulation code was used to estimate the total efficiency of the exclusive breakup measurement [155, 156]. Details of this will be given below (section 3.4.1). Here we will refer to simulation spectra will be given here in comparison with experimental data for confirming the kinematics used in the program and for identification of the resonant and non-resonant part of breakup, unresolved in the experimental data. The program takes into account the energy loss at the tantalum foils (see Figure 2.8) as well as the angular and energy thresholds of the detectors. The results of the simulation for the first kinematical solution are compared with the two-dimensional experimental energy spectra ($E_\alpha\%E_{d(p)}$) in Figures 3.8, 3.9 and 3.10 for the 29, 25 and 20 MeV measurement, respectively. Particles associated with energies of the second kinematical solution were cut out by the tantalum foils and the magnetic fields of the spectrometer. It should be noted the good simulation of the experimental data and the discrimination of the resonant breakup denoted with the red dots and the continuum breakup denoted with the green dots. The observed loci at the extreme right region of the spectra (black line) are due to carbon contamination. (see also Figure 3.7 right). Further on, one-dimensional experimental coincidence spectra from the 5° detector are compared with the simulated ones in Figures 3.11, 3.12 and 3.13 for 29, 25 and 20 MeV, respectively. Superimposed to these spectra are shown in green, spectra obtained with the carbon target, appropriately normalized to the flux and scattering centers of the CH_2 measurement. It comes out that the carbon contamination is very low for the two highest energies, but not for the lower one, for which however we have not proceed with final breakup cross sections as the determination of the beam flux did not look correct. Furthermore, it can be seen that the α - p coincidence events are well-discriminated from α - d coincidences. Finally, a simulation was also performed for the ${}^6\text{Li} + {}^1\text{H} \rightarrow {}^5\text{Li} + {}^2\text{H} \rightarrow {}^4\text{He} + {}^1\text{H} + {}^2\text{H}$ reaction, which however is expected to have very low cross section. The results of this simulation are given in Figures 3.11-3.13 with the dashed blue line and it is clear that its contribution can not affect greatly the breakup data.

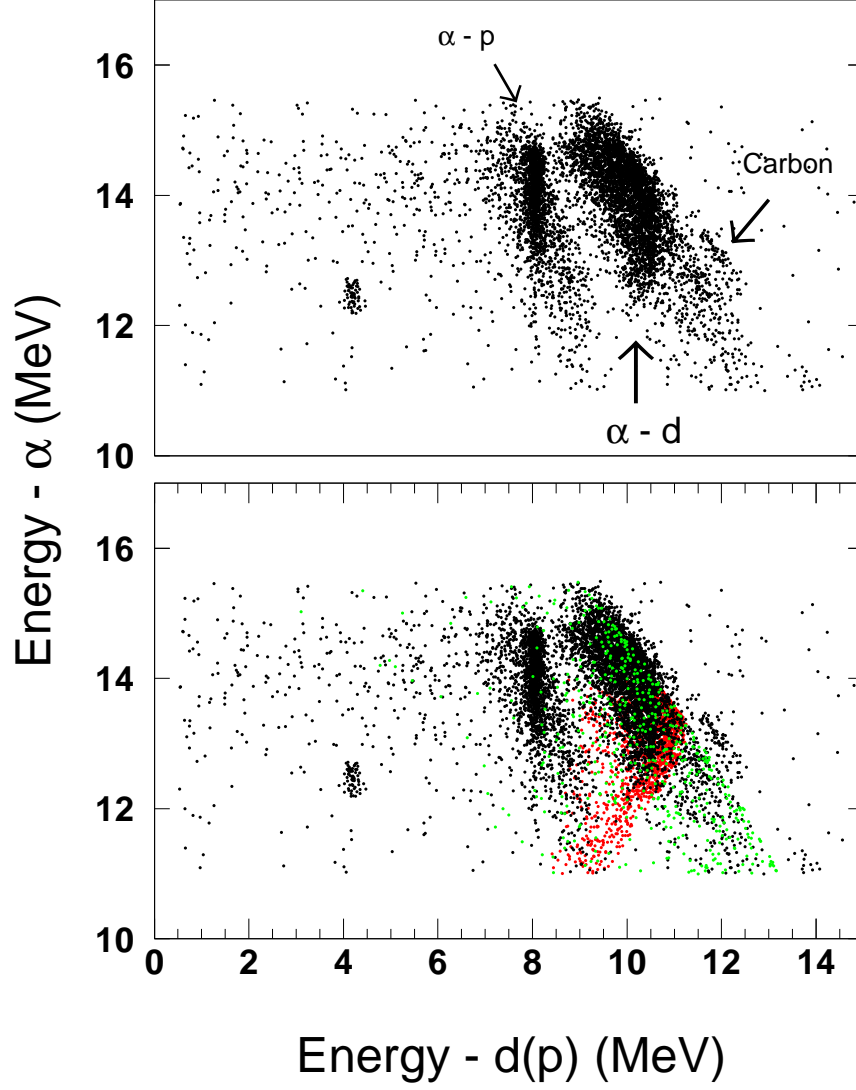


Figure 3.8: *Top Figure: Two dimensional plot of the measured energy of alpha particles (Energy - α) versus measured energy of deuterons or protons (Energy - d(p)) at the beam energy of 29 MeV (4.83 MeV/u). The observed loci for α - p coincidences, α - d coincidences due to breakup of ${}^6\text{Li}$ on hydrogen and α - d coincidences due to breakup on carbon are indicated in this Figure. Bottom Figure: Superimposed on the experimental top spectrum, designed in black, simulated events of the first kinematical solution for the resonant and direct breakup can be observed, designated with red and green dots respectively.*

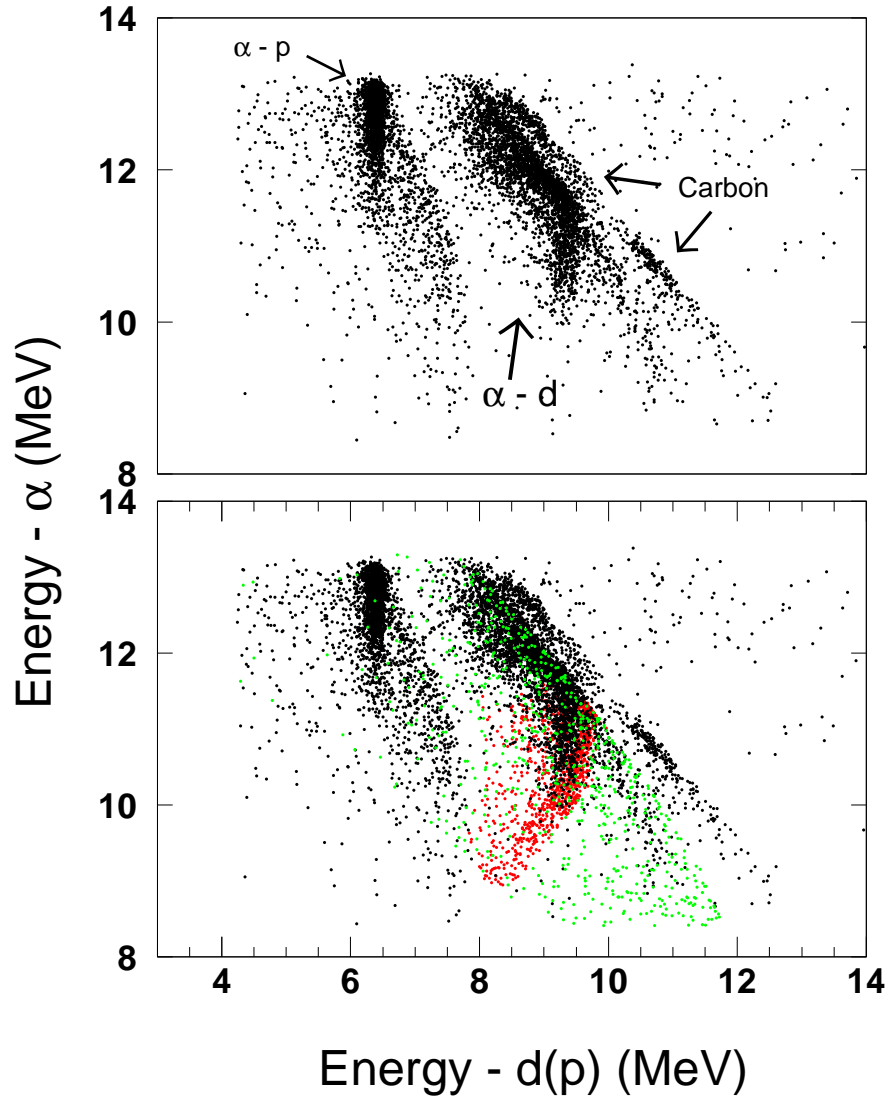


Figure 3.9: Same as in Figure 3.8 but for the energy of 25 MeV (4.17 MeV/u).

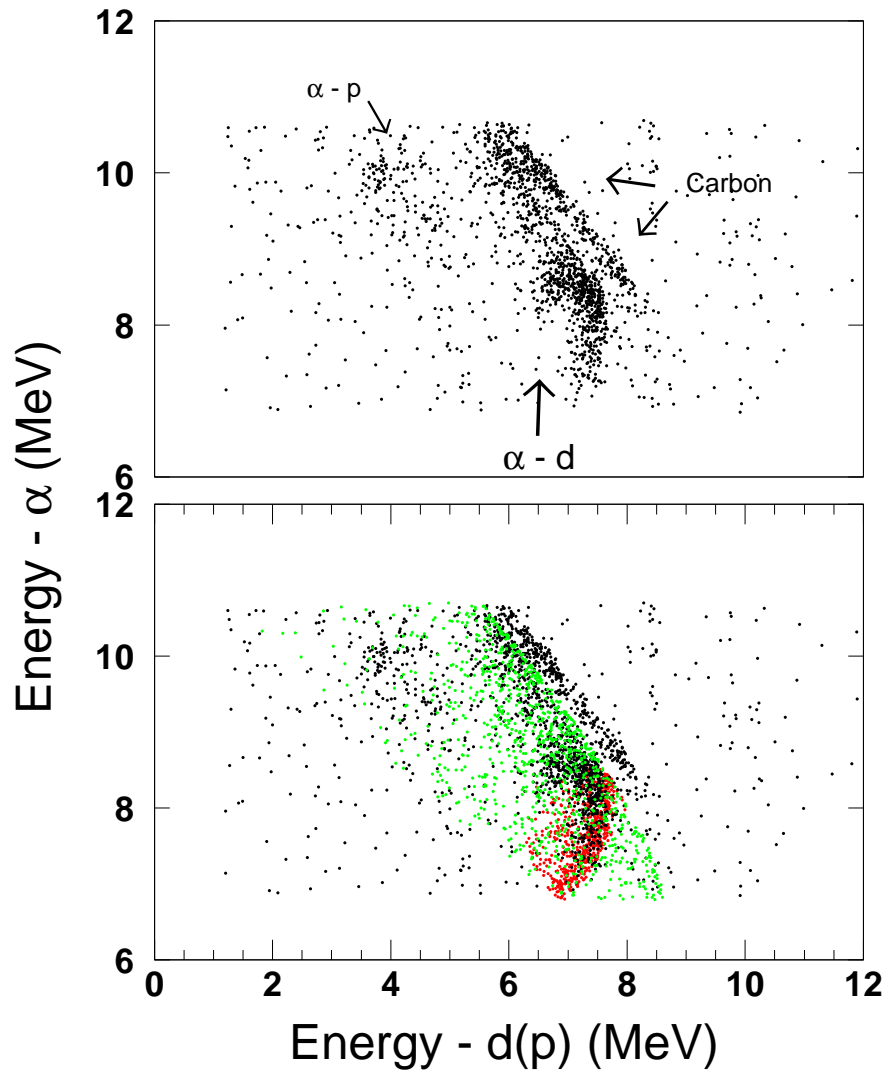


Figure 3.10: *Same as in Figure 3.8 but for the energy of 20 MeV (3.33 MeV/u).*

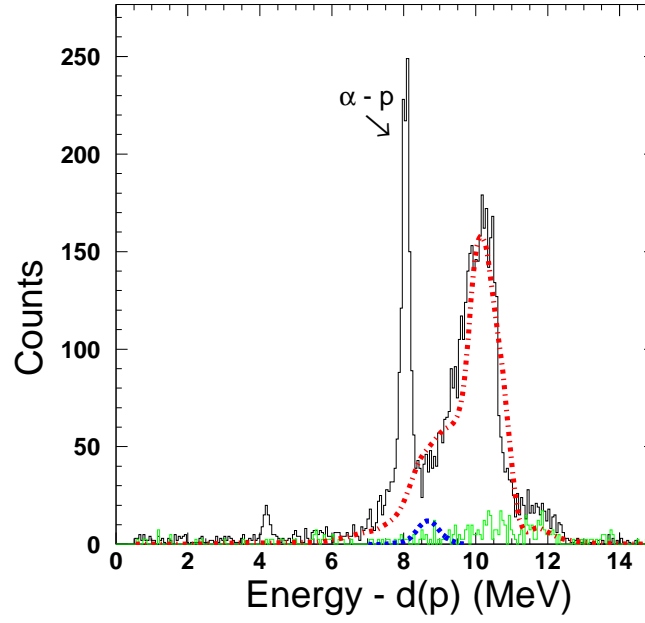


Figure 3.11: *Exclusive breakup spectrum, acquired in the 5° silicon detector with the CH_2 target at 29 MeV (α -d or α -p coincidences). Simulations for the first kinematical solution for α - d coincidences, are given with the red dotted-dashed line. The peak at the left corresponds to α coincidences with the recoiling protons. The spectrum in green, represents an exclusive spectrum acquired with the carbon target, appropriately normalized. Last, the peak designated with a blue dashed line, represents a simulation for the reaction ${}^6\text{Li} + p \rightarrow {}^5\text{Li} + d \rightarrow \alpha + p + d$ arbitrarily normalized (see text for details).*

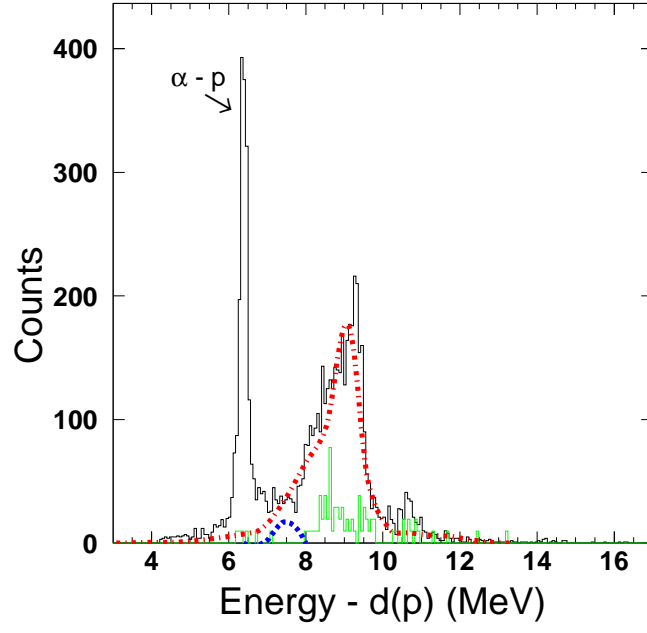


Figure 3.12: Same as in Figure 3.11 but for the energy of 25 MeV (4.17 MeV/u).

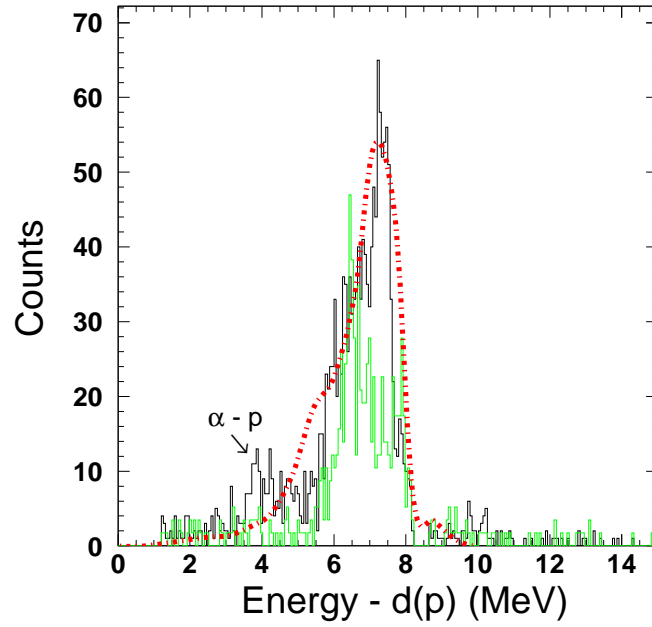


Figure 3.13: Same as in Figure 3.11 but for the energy of 20 MeV (3.33 MeV/u).

3.3 Determination of the elastic scattering cross section

The next step, after the identification of the elastic channel, is the extraction of the differential cross sections. Using the reconstructed E - θ correlation plots (e.g. Figure 3.4) the data were divided in bins with an angular step of 0.5° , and subsequently counts were integrated for every bin. The solid angle, defined by four slits located 25 cm from the target, was determined geometrically ($\Omega = \Delta\theta * \Delta\varphi$) with an uncertainty of $\sim 2\%$ while the beam charge, collected by a Faraday cup set at the entrance of MAGNEX was determined with an uncertainty of $\sim 5\%$. A 5% error was adopted also for the scattering centers. Taking into account all the above, the differential cross sections in the laboratory frame were determined by formula (3.7) while the normalization of the data was cross-checked via the measurement at the very forward angles where the elastic scattering is Rutherford.

$$\left(\frac{d\sigma_{el}}{d\Omega}\right)_{lab} = \frac{N_{el-net}}{T_{el}\Phi_{el}\Omega_{el}\epsilon} \quad (3.7)$$

where N_{el-net} is the number of counts for a specific laboratory angle after subtracting the background counts $N_{el-backg}$ from the total counts N_{el-tot} , T_{el} and Φ_{el} are the scattering centers and the beam flux respectively, Ω_{el} is the solid angle of the elastic scattering measurement and ϵ is the efficiency of the FPD ($\sim 89\%$). The uncertainty Σ_{el} related to the differential cross section was estimated via the following formula:

$$\Sigma_{el} = \pm \left(\frac{d\sigma_{el}}{d\Omega}\right)_{lab} \sqrt{\frac{N_{el-tot} + N_{el-backg}}{(N_{el-net})^2} + \left(\frac{\Sigma_{T_{el}}}{T_{el}}\right)^2 + \left(\frac{\Sigma_{\Phi_{el}}}{\Phi_{el}}\right)^2 + \left(\frac{\Sigma_{\Omega_{el}}}{\Omega_{el}}\right)^2} \quad (3.8)$$

where $\Sigma_{T_{el}}$, $\Sigma_{\Phi_{el}}$ and $\Sigma_{\Omega_{el}}$ are the uncertainties related with the scattering centers, the flux of the beam and the solid angle respectively. It should be noted that the background is negligible and affects only a few data points. In general, the error in the determination of the elastic scattering differential cross section is less than 10%. This error includes the statistical error, the error due to the (small) background subtraction, errors due to the target thickness as well as the uncertainty at the beam flux measurement and the solid angle determination. Details regarding the deduction of the uncertainty Σ_{el} are given in the Appendix B.1.

Looking at the correlation plot shown at Figure 3.4, we may see that the angular step of 0.5° is not the appropriate one for the region of $\theta_{lab} \geq 8.5^\circ$. In particular, due to inverse kinematics, such an angular step would lead to huge angular uncertainties in the center of mass frame. As an example, the angular range 9.0 - 9.5° in the laboratory frame corresponds to an angular range 78.8° - 91.7° (1st solution) or 107.0° - 119.2° (2nd solution) in the center of mass frame. Thus, to overcome this problem, a different procedure was followed for this region.

First of all, the energy range corresponding to $\theta_{lab} \geq 8.5^\circ$ was discretized into equal energy bins. For each energy an angle in the center of mass frame was attributed, which finally was transformed to the laboratory via a (cm to lab) program (see Appendix C.1). The solid angle for each bin was determined geometrically as before ($\Omega = \Delta\theta * \Delta\phi$) but with $\Delta\theta$ corresponding to the appropriate angular range (angular range for each energy step). Finally, the differential cross sections and their uncertainties were determined applying the procedure described above.

The experimental data points were transformed to the center of mass frame by calculating the appropriate Jacobians (program in Appendix C.2). The data are presented in Figures 3.14-3.17 while, in the majority of the data points, the error bars are included within the data point size. The present data are also reported in Refs. [73, 74] while tabulated values of them are given in the Appendix D.

For reasons of completeness, the present elastic scattering data, obtained via inverse kinematics, were compared with previous data obtained via direct kinematics measurements at similar energies [31, 32]. As an example, a comparison between present and previous data at 29 MeV (4.83 MeV/u) is illustrated in Figure 3.18. As it can be seen, the agreement between themselves is good for the angular range where previous data exist. Taking into account that our data extend to smaller angles than the previously measured ones, where the scattering is Rutherford, we can conclude that the present data validate (or not) the normalization of the previous data. Similar conclusions can be drawn for the lower-energy data, which are presented in Figures 3.19-3.21.

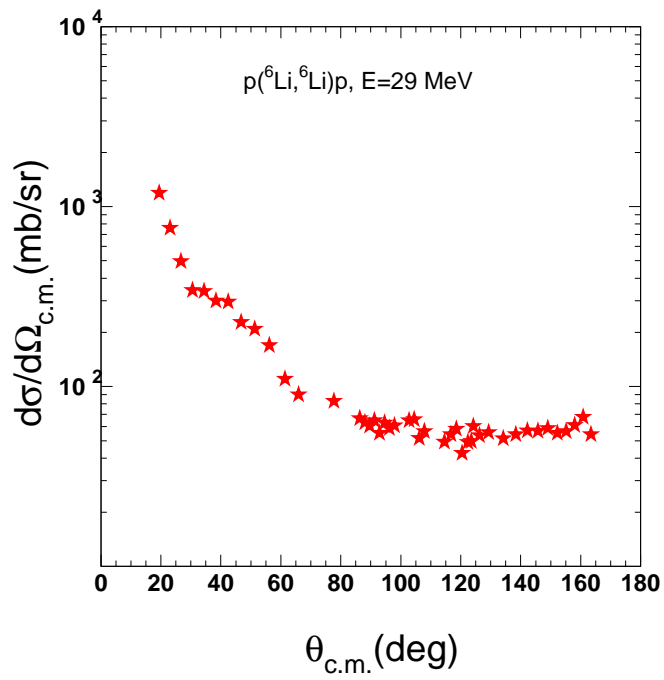


Figure 3.14: *Present elastic scattering data for $^6\text{Li}+p$ at 29 MeV (4.83 MeV/u). The data uncertainties are included in the size of the data spots and are of the order of 8%. Tabulated values of the data are given in Appendix D.*

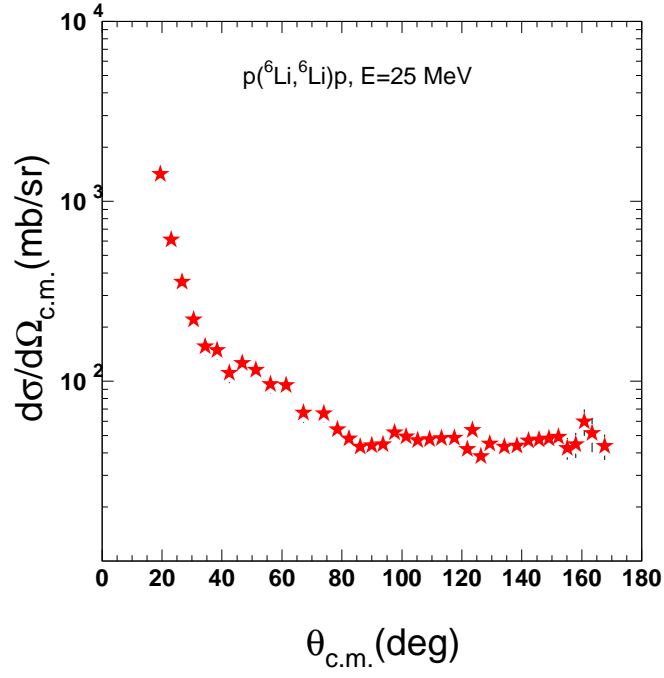


Figure 3.15: Same as in Figure 3.14 but for the energy at 25 MeV (4.17 MeV/u).

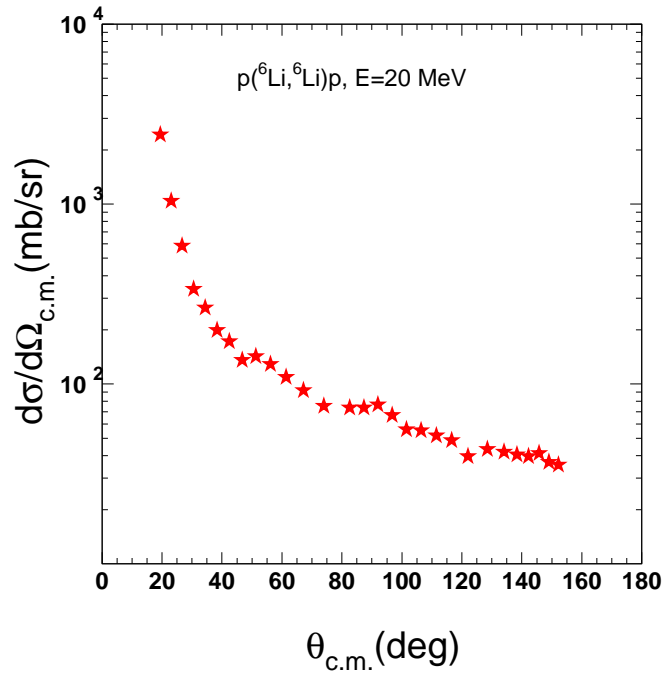


Figure 3.16: Same as in Figure 3.14 but for the energy at 20 MeV (3.33 MeV/u).

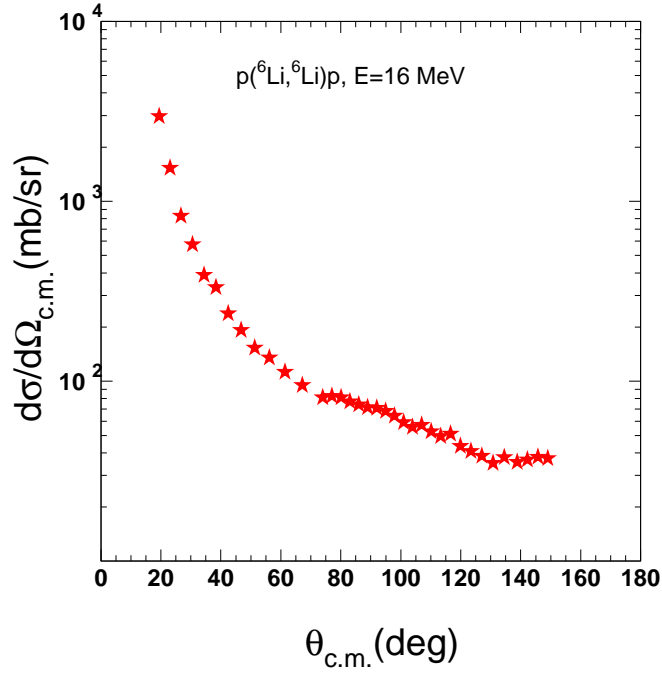


Figure 3.17: Same as in Figure 3.14 but for the energy at 16 MeV (2.67 MeV/u).

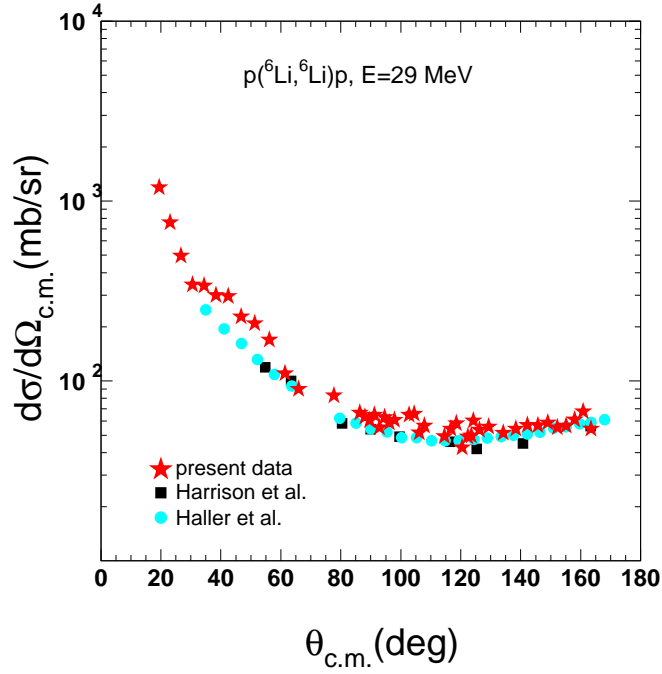


Figure 3.18: Comparison between present and previous experimental data [31, 32] at 29 MeV.

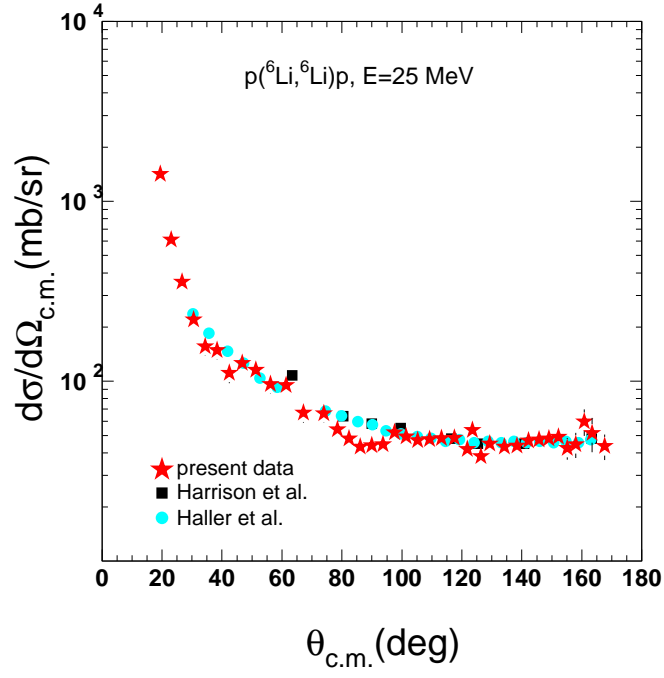


Figure 3.19: Same as in Figure 3.18 but for the energy at 25 MeV (4.17 MeV/u).

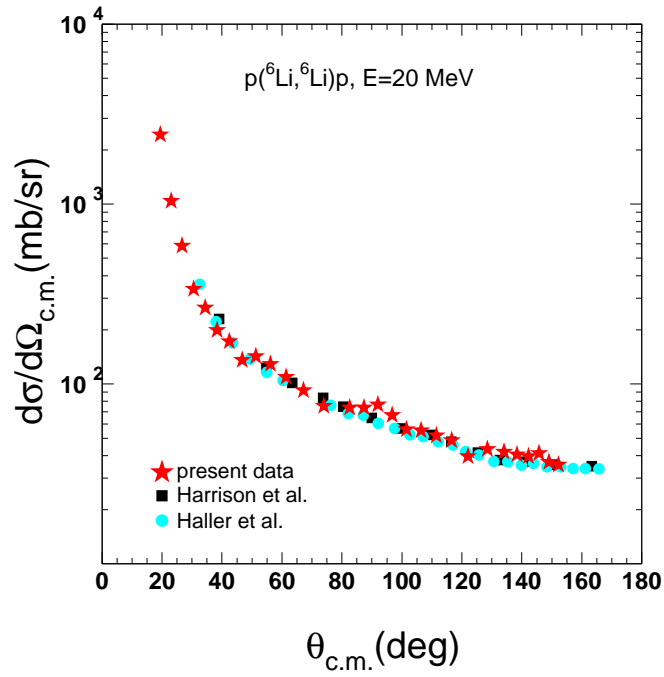


Figure 3.20: Same as in Figure 3.18 but for the energy at 20 MeV (3.33 MeV/u).

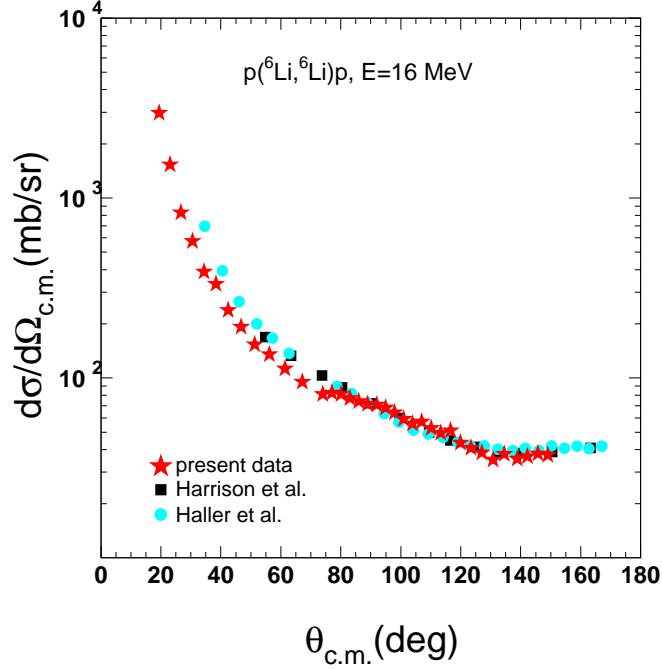


Figure 3.21: Same as in Figure 3.14 but for the energy at 16 MeV (2.67 MeV/u).

3.4 Determination of the breakup cross section

After the identification procedure of the breakup channel, the determination of the double differential cross sections in the laboratory frame is possible. In a similar way as in the elastic scattering case, breakup yields were integrated for an angular step of 0.5° , referring to the CH_2 target and the procedure was repeated for the data obtained by the carbon run in order to subtract the contribution due to carbon contamination. Since, in this case, we used reconstructed parameters in order to clean the spectra (e.g. y_i : beam dimension), the number of counts was multiplied by a correction factor to account for missing counts due to the ray-reconstruction procedure efficiency. The events obtained with the carbon run were also normalized to the scattering centers and flux of the CH_2 runs. The total detection efficiency was calculated by a simulation program while the beam flux was measured by a Faraday cup located besides the FPD. Thus, the double differential cross sections in the laboratory system were determined by the following formula:

$$\left(\frac{d^2\sigma_{bu}}{d\Omega_\alpha d\Omega_d} \right)_{lab} = \frac{a_{bu}N_{bu} - \phi a_{car}N_{car}}{T_{bu}\Phi_{bu}\varepsilon_{bu}} \quad (3.9)$$

where N_{bu} and N_{car} are the number of counts for CH_2 and carbon runs respectively while a_{bu} and a_{car} are the efficiency corrections due to reconstruction procedure for the CH_2 and ^{12}C runs respectively. The ϕ is a factor used for normalizing the events obtained with the carbon run to the flux and scattering centers of the CH_2 run. Also, T_{bu} , Φ_{bu} and ε_{bu} are the hydrogen scattering centers of the CH_2 target, the beam flux and the total detection efficiency, respectively. The uncertainty Σ_{bu} , related to the double differential cross section, was estimated via the following formula:

$$\Sigma_{bu} = \pm \left(\frac{d^2\sigma_{bu}}{d\Omega_\alpha d\Omega_d} \right)_{lab} \sqrt{\frac{a_{bu}^2 N_{bu} + a_{car}^2 \phi^2 N_{car}}{(a_{bu} N_{bu} - a_{car} \phi N_{car})^2} + \left(\frac{\Sigma_{T_{bu}}}{T_{bu}} \right)^2 + \left(\frac{\Sigma_{\Phi_{bu}}}{\Phi_{bu}} \right)^2 + \left(\frac{\Sigma_{\varepsilon_{bu}}}{\varepsilon_{bu}} \right)^2} \quad (3.10)$$

where $\Sigma_{T_{bu}}$, $\Sigma_{\Phi_{bu}}$ and $\Sigma_{\varepsilon_{bu}}$ are the uncertainties related with the scattering centers, the flux and the total efficiency respectively. The uncertainty in the determination of the breakup double differential cross section includes the statistical error, the error due to the carbon background subtraction, errors due to the target thickness, the uncertainty at the beam flux measurement as well as the efficiency determination via the simulation program. A detailed description for the deduction of the error formula (B.12) is given in the Appendix B.2. Details about both the simulation program and the extraction of the total efficiency ε_{bu} are given at the following subsection.

3.4.1 Determination of the efficiency

The total efficiency ε_{bu} of the exclusive breakup measurement was estimated via the Monte Carlo three-body simulation program MULTIP [155, 156]. The simulation takes into account the reaction $^6\text{Li}+p$ leading to an excited state of $^6\text{Li}^*$ with an angular distribution, determined in the CDCC calculations. The ^6Li ions acquire randomly an excitation energy inside the energy bin as specified in the CDCC framework. This includes either the resonance bin at $E_x=2.186$ MeV (0.706 MeV above the breakup threshold), or anyone of the continuum bins. The $^6\text{Li}^*$ breaks in two fragments in its rest frame, with the one (alpha particle) emitted randomly with a specific energy and momentum and the second (deuteron) with energy and momentum fulfilling conservation laws. The so obtained energy distributions of the fragments in the rest frame of $^6\text{Li}^*$ are transformed to the laboratory system by imposing a Galilean transformation followed by the appropriate axes rotation.

The program takes into account the experimental conditions such as the angular ranges and the energy thresholds of the detectors while the output of the program provides the energy and angular distributions for both breakup fragments as well as the correlation plots. A

selection between the two kinematical solutions is also possible. By comparing, the number of events with all the experimental conditions at a specific angle with the events without any condition, the total efficiency for the specific angle can be determined. This efficiency includes the geometrical efficiency (solid angle) as well as other efficiencies related with the detection thresholds at the detectors. As an example, we could note the cuts introduced by MAGNEX as a result of the magnetic fields settings, optimized for avoiding the elastic scattering events. The detection of the whole energy range of the breakup events would have required several measurements with different magnetic fields (like the elastic scattering measurements) and, consequently, much more time than the present measurement. Also, the 5° detector covers a limited angular range while the tantalum foils introduced an extra energy detection threshold. Using the simulation program, the efficiency was determined in a compact way minimizing the uncertainties. The total efficiency in the present experiment was of the order of $\sim 10^{-8}$ with a mean uncertainty of 14% (12 to 22%).

The MULTIP program has been used, so far, for efficiency or/and identification purposes for the following reactions:

1. ${}^6\text{Li} + {}^1\text{H} \rightarrow {}^4\text{He} + {}^2\text{H} + {}^1\text{H}$ ([74] and present work)
2. ${}^6\text{Li} + {}^1\text{H} \rightarrow {}^5\text{Li} + {}^2\text{H} \rightarrow {}^4\text{He} + {}^1\text{H} + {}^2\text{H}$ ([74] and present work)
3. ${}^7\text{Li} + {}^1\text{H} \rightarrow {}^4\text{He} + {}^3\text{H} + {}^1\text{H}$ ([78])
4. ${}^7\text{Be} + {}^{28}\text{Si} \rightarrow {}^4\text{He} + {}^3\text{He} + {}^{28}\text{Si}$ ([156])
5. ${}^7\text{Be} + {}^{28}\text{Si} \rightarrow {}^8\text{Be} + {}^{27}\text{Si} \rightarrow {}^4\text{He} + {}^4\text{He} + {}^{27}\text{Si}$ ([156, 158])
6. ${}^7\text{Be} + {}^{28}\text{Si} \rightarrow {}^6\text{Be} + {}^{29}\text{Si} \rightarrow {}^4\text{He} + {}^1\text{H} + {}^1\text{H} + {}^{29}\text{Si}$ ([156, 158])
7. ${}^8\text{B} + {}^{208}\text{Pb} \rightarrow {}^7\text{Be} + {}^1\text{H} + {}^{208}\text{Pb}$ ([159])

In all the cases the program was found to be very accurate. More technical details about the program are given in Ref. [156].

3.4.2 Deduction of the breakup angular distributions in the center of mass frame

Taking into account the efficiency of the detection system and by using Eq. (3.9), the double differential breakup cross sections were determined for all the measured α - d pairs.

These cross sections were transformed to the center of mass frame by using the appropriate Jacobians. In order to determine these factors we assumed the inelastic scattering ${}^6\text{Li} + \text{p} \rightarrow {}^6\text{Li}^* + \text{p}$ with an excitation energy E_x and an angle $\theta_{c.m.}$. The excitation energy for each angle was determined as a weighted mean between the various excitation energies corresponding to the continuum energy bins adopted in the CDCC calculations, taking as a weight function the cross section of each energy in the bin. Furthermore, for each pair of laboratory angles $(\theta_{\alpha lab}, \theta_{d lab})$, a center of mass angle $\theta_{c.m.}$ was assigned applying the Ohlsen formulas [157]. In this way, the breakup differential cross sections in the center of mass frame were calculated. The breakup angular distributions for 29 and 25 MeV are shown in Figures 3.22 and 3.23 respectively, while tabulated values of them are given in the Appendix D. Unfortunately, a problem at the normalization of the 20 MeV experimental data did not allow the extraction of a reliable angular distribution for this energy. It should be also noted that, our data are limited in the angular range between 10° and 90° since particles associated with energies corresponding to the second kinematical solution were cut out by the tantalum foils or/and the selection of the detected energy range at the spectrometer. However, this was not a major problem for the extraction of the total breakup cross section as the angular distribution of the breakup in the center of mass frame is expected to be almost flat according to our CDCC calculations. Therefore the experimental total breakup cross sections were estimated by assuming the shape of the CDCC angular distribution, for angles where data do not exist. The total breakup cross sections are presented in details in the next chapter where they are compared with theoretical calculations.

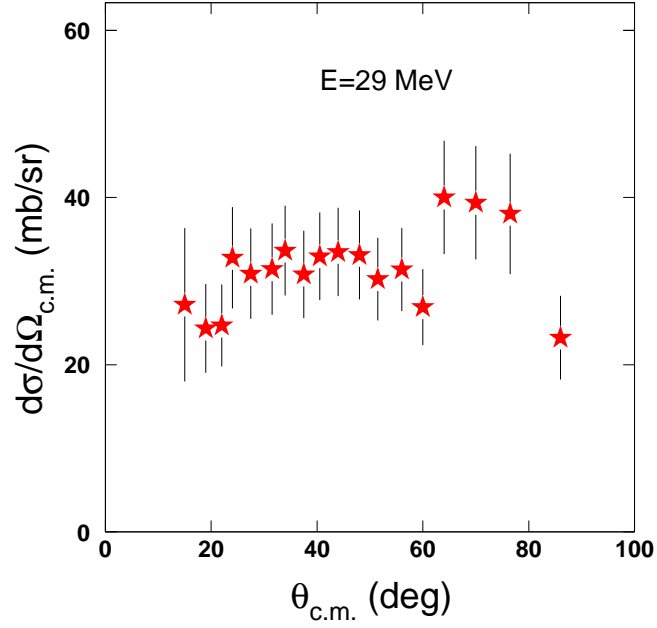


Figure 3.22: *Present breakup angular distribution for the ${}^6\text{Li}+p$ system at 29 MeV (4.83 MeV/u). Tabulated values of the data are given in the Appendix D.*

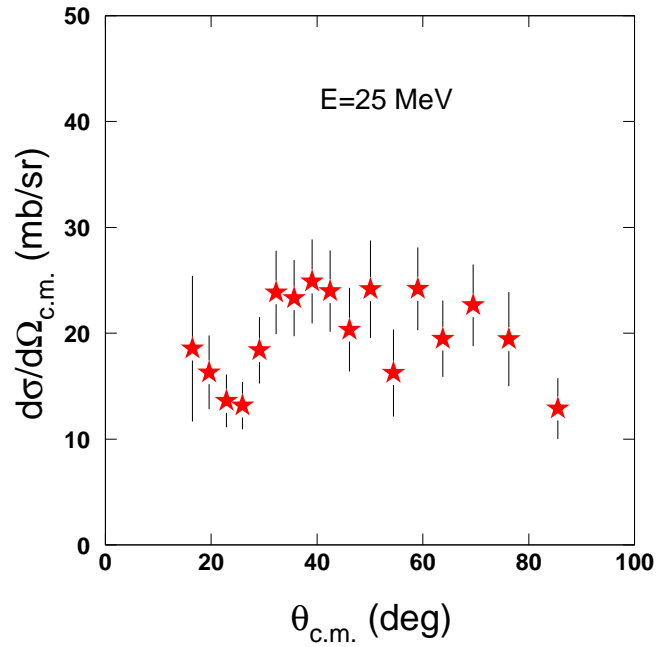


Figure 3.23: *Same as in Figure 3.22 but for the energy at 25 MeV (4.17 MeV/u).*

Chapter 4

Theoretical analysis

This chapter includes the theoretical analysis of the present elastic scattering and breakup data. The elastic scattering data are considered in the microscopic approach of the Jeukenne-Lejeune-Mahaux (JLM) potential [5], to be described in section 4.1, as well as to a Continuum Discretized Coupled Channel (CDCC) framework, to be described in section 4.2. The FRESKO code [116] adopted for the CDCC calculations provides as output angular distributions for both elastic scattering (subsection 4.2.1) and breakup (subsection 4.2.2), which can be compared with the present data. It provides also absorption cross sections, which for reasons of completeness will be presented here (subsection 4.2.2) to be compared with measurements performed simultaneously as part of an MSc thesis [75, 76].

4.1 JLM Calculations

The elastic scattering data were also considered in a microscopic JLM approach without any coupling. Into this context, the Jeukenne-Lejeune-Mahaux model [5] was adopted according to the code developed by F. S. Dietrich et al. [20] at a standard normalization ($\lambda_V=1.0$ and $\lambda_W=0.8$). The density for ${}^6\text{Li}$ was derived from K. H. Bray et al. [36]. Calculations, performed with this code [160], are compared with our elastic scattering data in Figures 4.1-4.4, where it is seen that they fail to reproduce the data. It should be noted that in the JLM model, numerical results for the real and imaginary part of the potential were parameterized for obtaining analytical forms, taking into account data of medium and heavy mass stable nuclei at the energy interval $10 \leq E \leq 160$ MeV/u. The model was successfully applied to stable nuclei inside that energy region in Refs. [17–19]. Also the calculations were performed for infinite

nuclear matter and transferred to finite nuclei by applying the local density approximation. Therefore the application of this approach outside the mass and energy interval, where the model was validated, constitutes a severe test to it. A comprehensive discussion of these points can be found in Ref. [14]. The applicability of the JLM method at lower energies ($7 \leq E \leq 24$ MeV/u) was tested in Ref. [20] and for low to high mass numbers in Refs. [18, 21]. Recently, the JLM potential without any coupling was also validated for the system $^{17}\text{F} + \text{p}$ at a rather low energy ~ 4 MeV/u [22] providing good agreement with the data. This is the first time that the model is tested for a very light weakly bound projectile as ^6Li and at very low energies $E = 2.6 - 4.8$ MeV/u.

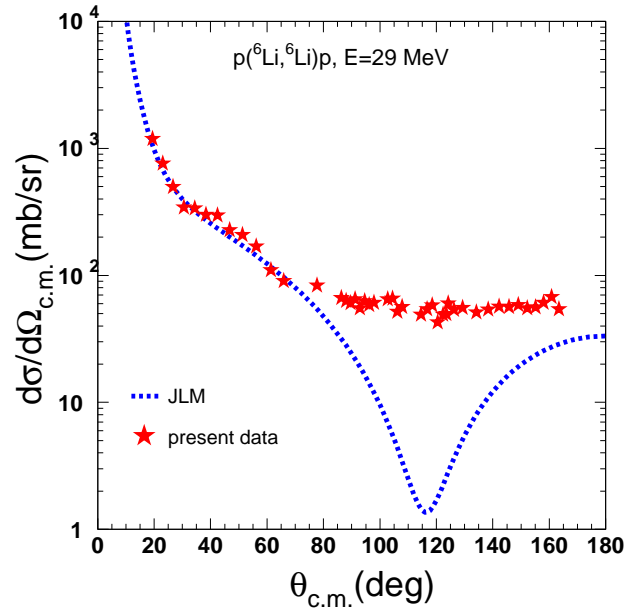


Figure 4.1: *Present elastic scattering data for $^6\text{Li} + \text{p}$ at 29 MeV (4.83 MeV/u) are compared with a JLM calculation without any coupling, denoted with the blue dashed line (see text).*

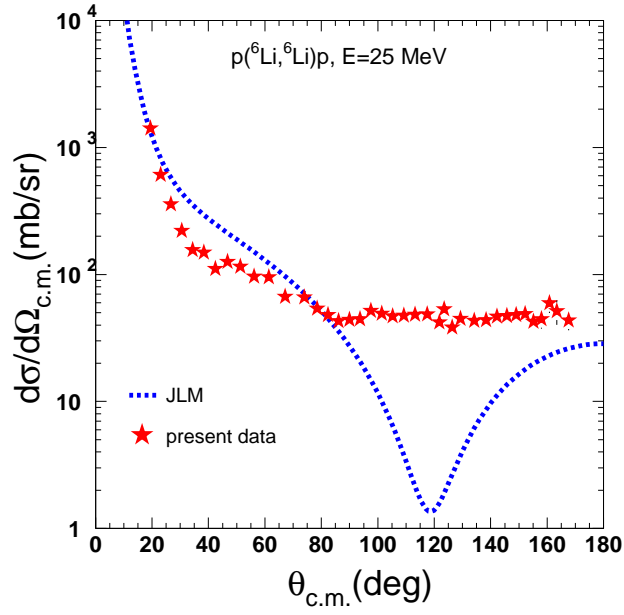


Figure 4.2: Same as in Figure 4.1 but at the energy of 25 MeV (4.17 MeV/u).

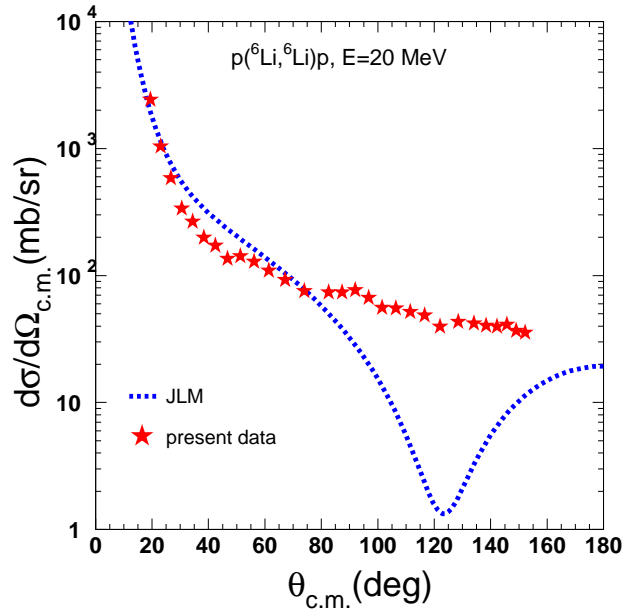


Figure 4.3: Same as in Figure 4.1 but at the energy of 20 MeV (3.33 MeV/u).

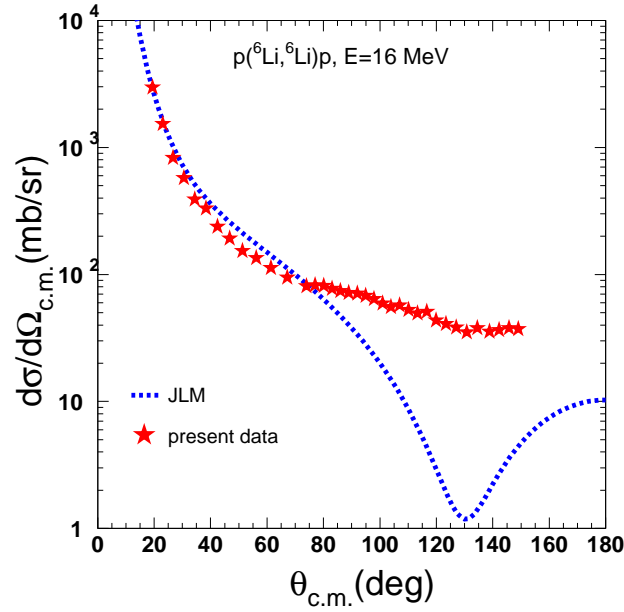


Figure 4.4: Same as in Figure 4.1 but at the energy of 16 MeV (2.67 MeV/u).

4.2 Continuum Discretized Coupled Channel Calculations (CDCC)

Continuum Discretized Coupled Channel (CDCC) calculations were performed in order to explain the present experimental data in a global framework. For these calculations we follow the same technique as in [38], where CDCC calculations were presented for the same system at 155 MeV (25.8 MeV/u).

A cluster $\alpha + d$ model of ${}^6\text{Li}$ was adopted, with all the parameters of the model including discretization and truncation described in detail in Refs. [64, 73, 74]. The relative orbital angular momentum between the α particle and the deuteron was limited to the values $L=0, 1, 2$ [63, 64, 161]. Tests with higher angular momenta did not change the result. The 3^+ resonance was taken into account and was treated as a momentum bin, with a width of 100 keV. Other resonant states were not taken into account since the available energy was such that it was not possible to excite them [162, 163].

The central part of the entrance potentials for $\alpha - p$ and $d - p$, was derived as previously [38] from empirical $p - \alpha$ and $p - d$ potentials by means of a single - folding method. The empirical potentials were obtained from $p + d$ and $p + \alpha$ elastic scattering studies at $E = 2.52$ to

5 MeV/u performed previously [164–170]. These $p + d$ and $p + \alpha$ elastic scattering data were fitted by simple Woods Saxon form factors for both real volume and imaginary volume parts for the $p + \alpha$ system and a real volume and a surface imaginary term for the $p + d$ system [160]. The optical model potential parameters for the $p + \alpha$ and $p + d$ interactions are listed in Tables 4.1 and 4.2 respectively. As it can be seen, the radii and diffusenesses remain constant for all energies, while the depths follow the formulas (4.1) and (4.2) for $\alpha - p$ and $d - p$ potentials, respectively.

$$\begin{aligned} V_{\alpha p} &= 68.528 - 3.91577E \\ W_{\alpha p} &= 0.033 + 0.0014E \end{aligned} \tag{4.1}$$

$$\begin{aligned} V_{dp} &= 92.1207 - 5.2642E \\ W_{dp} &= 0.5995 + 0.0241E \end{aligned} \tag{4.2}$$

where V and W are the depths for the real and the imaginary part of the potential respectively, while E is the reaction energy in the laboratory frame in MeV/u. A spin-orbit term was necessary for the best fit of the data but, it was not possible to be used in the CDCC calculation as a part of $p + d$ or $p + \alpha$ interaction. Instead of that, a spin-orbit potential of Thomas form with parameters $V_{so}=4.26$ MeV, $r_{so}=1.10$ fm and $\alpha_{so}=0.35$ fm was added to the diagonal ${}^6\text{Li} + p$ Watanabe folding potentials.

Further on, the potential binding the deuteron to α particle core was assumed to have a Woods - Saxon shape as described in Ref. [64]. Subsequently, all the potentials mentioned above were fed to a FRESKO calculation [116]. This calculation gives in detail angular distributions for both elastic scattering and breakup modes as well as absorption cross sections and total reaction cross sections. The first three observables were tested in the present experiment, while the first two are the subject of the present thesis.

4.2.1 Elastic Scattering

The results of the CDCC calculations described above, were compared with the elastic scattering data at all four energies in Figures 4.5-4.8. In these figures, the full CDCC calculations are denoted with the black solid line while calculations allowing coupling only to the direct excitation of the continuum, omitting coupling to the resonance, are denoted with the green dashed line. Furthermore, one-channel calculations, omitting coupling to the continuum, are depicted with the blue dotted-dashed line. Looking at the figures 4.5-4.8, we can see that,

Table 4.1: Optical model parameters for the system ${}^4\text{He} + \text{p}$, deduced by fitting previous experimental data [169, 170] adopting a Woods - Saxon potential (real and imaginary volume terms). The nuclear radius was $R=r_{V(W)}*4^{1/3}$ and the Coulomb radius was $R_C=1.25*4^{1/3}$. A spin orbit term with parameters $V_{so}=10.0$ MeV, $r_{so}=1.47$ fm and $\alpha_{so}=0.40$ fm was necessary for the best fit of the data but it was not used in the FRESCO calculation.

E (MeV)	$V_{\alpha p}$ (MeV)	r_V (fm)	α_V (fm)	$W_{\alpha p}$ (MeV)	r_W (fm)	α_W (fm)
29	49.811	1.10	0.477	0.040	1.10	0.477
25	52.278			0.039		
20	55.567			0.038		
16	58.230			0.037		

Table 4.2: Optical model parameters for the system ${}^2\text{H} + \text{p}$, deduced by fitting previous experimental data [164–168] adopting a Woods - Saxon potential (real volume and imaginary surface terms). The nuclear radius was $R=r_{V(W)}*1^{1/3}$ and the Coulomb radius was $R_C=1.30*1^{1/3}$. A spin orbit term with parameters $V_{so}=19.9$ MeV, $r_{so}=2.94$ fm and $\alpha_{so}=0.85$ fm was necessary for the best fit of the data but it was not used in the FRESCO calculation.

E (MeV)	V_{dp} (MeV)	r_V (fm)	α_V (fm)	W_{dp} (MeV)	r_W (fm)	α_W (fm)
29	66.958	1.25	0.501	0.715	1.20	0.517
25	70.274			0.700		
20	74.696			0.679		
16	78.276			0.663		

coupling to the full continuum (direct and resonant) is strong and adequate in order to describe the elastic scattering data in the most effective way. However, coupling to direct breakup makes a very slight change from the one-channel calculations, especially at the lower energies. Thus, the most important coupling at all energies is the coupling to resonant breakup while, the coupling to direct breakup has in principle a small impact, which however becomes larger at the higher energies. This behaviour of weak coupling to direct breakup and strong coupling to the resonant breakup is in accordance with similar findings of ${}^6\text{Li}$ scattering in medium and heavy mass targets [66, 67]. Another interesting point is that, at the lower energies the coupling to the resonance is very strong although, the resonant breakup cross section is quite low. In fact, at 16 MeV, the resonant breakup cross sections was only 0.03 mb out of a total breakup of 69.7 mb. A similar striking situation was recently reported for the elastic scattering

of ${}^7\text{Li} + \text{p}$ [78], where the resonant breakup was almost zero, ~ 0.5 mb, in comparison with a total breakup cross section of ~ 66 mb, but with a coupling to the resonant breakup to be dominant. This may be an example of a "virtual" coupling to continuum.

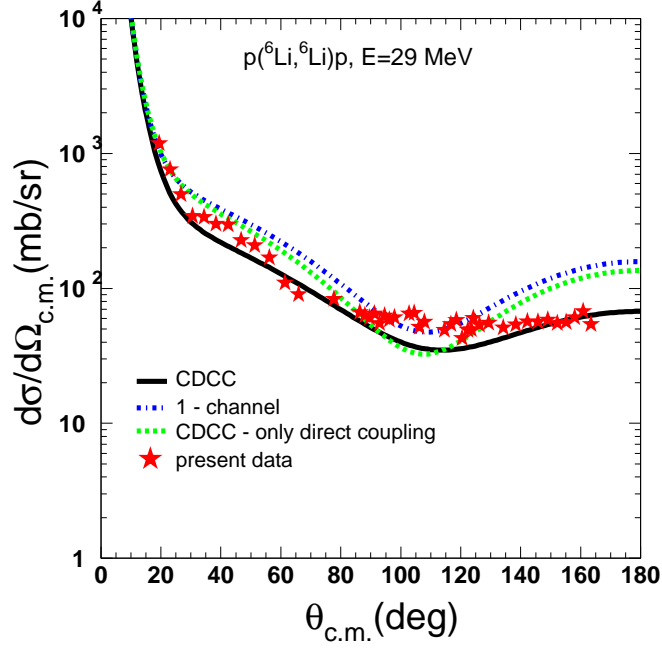


Figure 4.5: *Present elastic scattering data for ${}^6\text{Li}+p$ at 29 MeV (4.83 MeV/u). The data are compared with full CDCC calculations (solid black line), one-channel calculations (dotted-dashed blue line), and calculations with coupling only to direct breakup (dashed green line).*

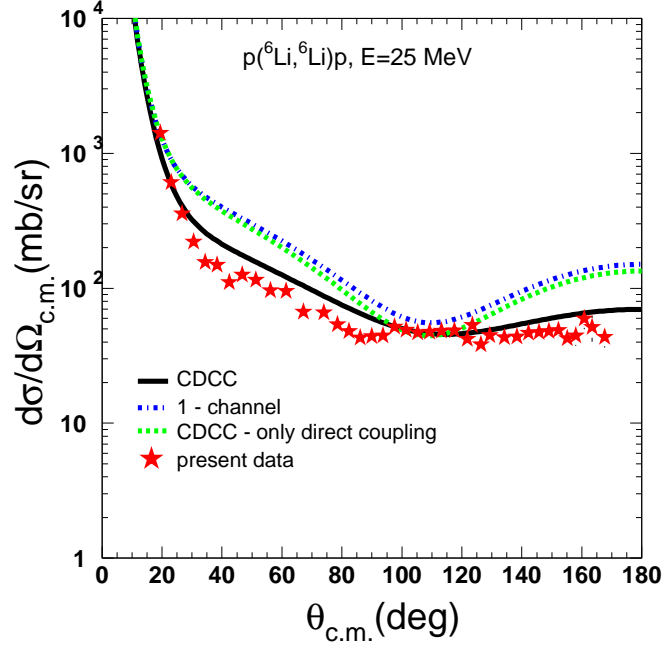


Figure 4.6: Same as in Figure 4.5 but at the energy of 25 MeV (4.17 MeV/u).

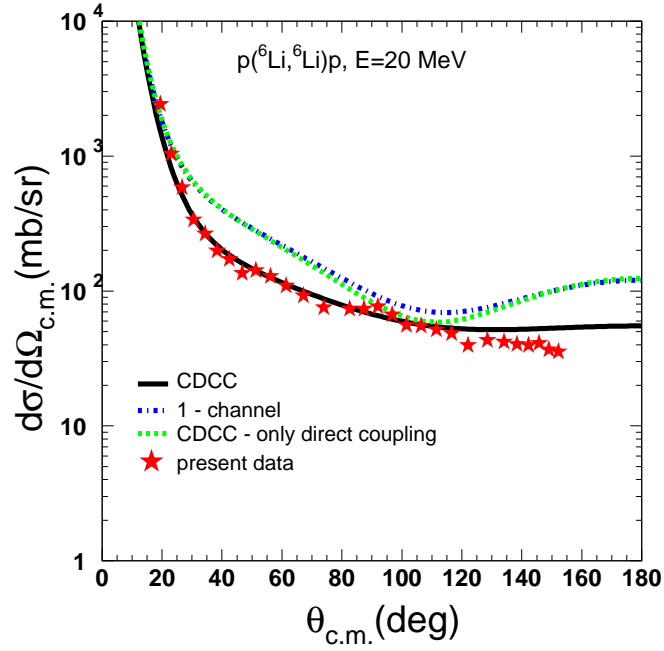


Figure 4.7: Same as in Figure 4.5 but at the energy of 20 MeV (3.33 MeV/u).

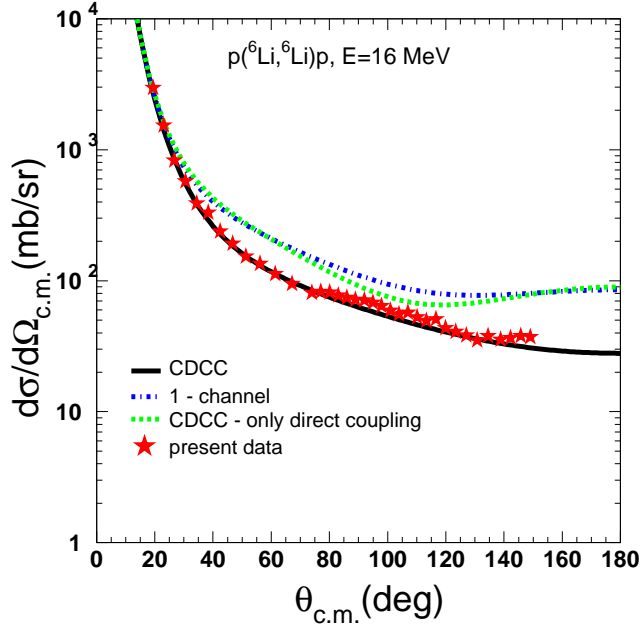


Figure 4.8: Same as in Figure 4.5 but at the energy of 16 MeV (2.67 MeV/u).

For reasons of completeness, the validity of the present elastic scattering data was checked into the global CDCC framework applied previously by Guo et al. [39] and Matsumoto et al. [40] for ${}^6\text{Li} + p$ in a wide energy range from 5 to 72 MeV/u. This was performed adopting the input potentials $\alpha - p$ and $d - p$ from Ref. [38] at the energy of 25.8 MeV/u but, scaling down the depths of the input potentials [171], according to the energy-dependent scaling procedure given in Ref. [39]. In this respect, the normalization factors for $E \leq 30$ MeV/u are given by the formula:

$$\begin{aligned}\lambda_V(E) &= 1 + 0.0035E \\ \lambda_W(E) &= 0.015E\end{aligned}\tag{4.3}$$

where E is the reaction energy in the laboratory frame in MeV/u units. The normalization factors determined for the real and the imaginary part are presented in Table 4.3. The optical model parameters for the $p - \alpha$ and $p - d$ interactions are presented in Tables 4.4 and 4.5 respectively. The calculations with this global approach (CDCC-G) are compared with the data as well as the main CDCC calculations (CDCC) in Figures 4.9-4.12. The calculation using this approach are in fair agreement with the experimental data in lower energies and larger angles while a good agreement is seen for the higher energies. Thus, the validity of Guo/Matsumoto approach seems to be extended to a lower energy region (4.0 - 4.8 MeV/u) than before (5 - 72 MeV/u).

Table 4.3: Normalization factors determined for the real and the imaginary part of the optical potential according to the energy-dependent scaling procedure given in Ref. [39].

E (MeV)	λ_V	λ_W
29	1.0168	0.0720
25	1.0145	0.0622
20	1.0116	0.0497
16	1.0092	0.0394

Table 4.4: Optical model parameters for the system $^4\text{He} + \text{p}$, adopting the potential from Ref. [38] but, scaling down the depths of the real and imaginary part of the potential, according to the energy-dependent scaling procedure given in Ref. [39]. Woods - Saxon volume form factors for both real and imaginary part were adopted. The nuclear radius was $R=r_{V(W)}*4^{1/3}$ and the Coulomb radius was $R_C=1.25*4^{1/3}$.

E (MeV)	$V_{\alpha p}$ (MeV)	r_V (fm)	α_V (fm)	$W_{\alpha p}$ (MeV)	r_W (fm)	α_W (fm)
29	49.766	1.10	0.477	0.040	1.10	0.477
25	49.659			0.035		
20	49.517			0.028		
16	49.399			0.022		

Table 4.5: Optical model parameters for the system $^2\text{H} + \text{p}$, adopting the potential from Ref. [38] but, scaling down the depths of the real and imaginary part of the potential, according to the energy-dependent scaling procedure given in Ref. [39]. Woods - Saxon volume and surface form factors were adopted for the real and imaginary part respectively. The nuclear radius was $R=r_{V(W)}*1^{1/3}$ and the Coulomb radius was $R_C=1.30*1^{1/3}$.

E (MeV)	V_{dp} (MeV)	r_V (fm)	α_V (fm)	W_{dp} (MeV)	r_W (fm)	α_W (fm)
29	66.899	1.25	0.501	0.717	1.20	0.517
25	66.754			0.623		
20	66.563			0.495		
16	66.405			0.395		

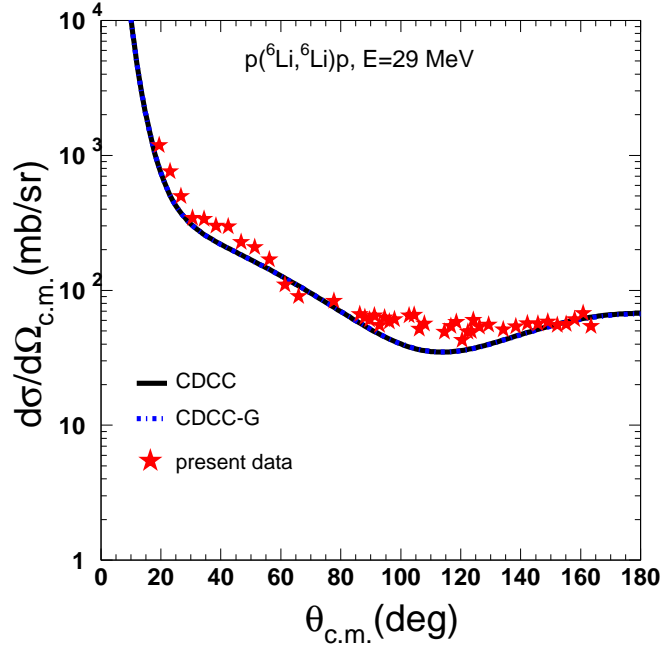


Figure 4.9: *Present elastic scattering data for ${}^6\text{Li}+p$ at 29 MeV (4.83 MeV/u) are compared with two different CDCC calculations. The calculation with the α - p and d - p potentials obtained by fitting previous data (CDCC) is denoted with the black solid line while, the calculation in the Guo framework (CDCC-G) is denoted with the blue dotted-dashed line. It should be noted that, for this energy, the calculations CDCC and CDCC-G gave almost the same results therefore lines are not distinguished from each other.*

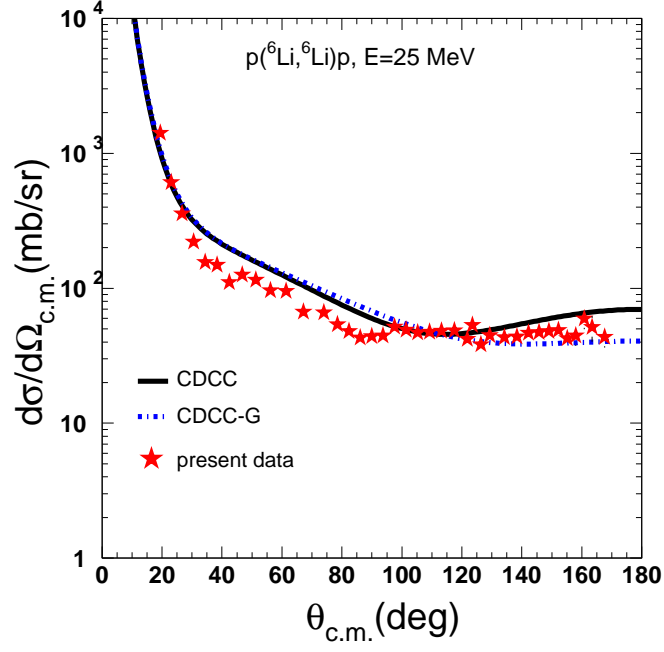


Figure 4.10: Same as in Figure 4.9 but at the energy of 25 MeV (4.17 MeV/u).

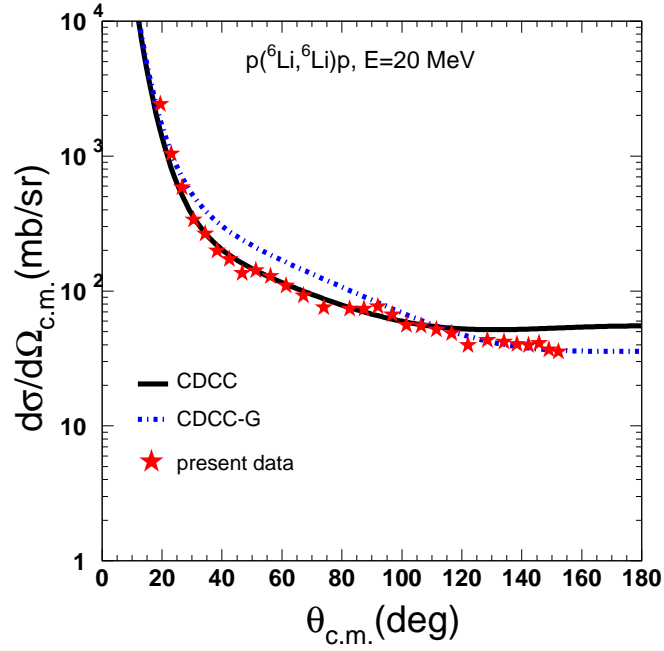


Figure 4.11: Same as in Figure 4.9 but at the energy of 20 MeV (3.33 MeV/u).

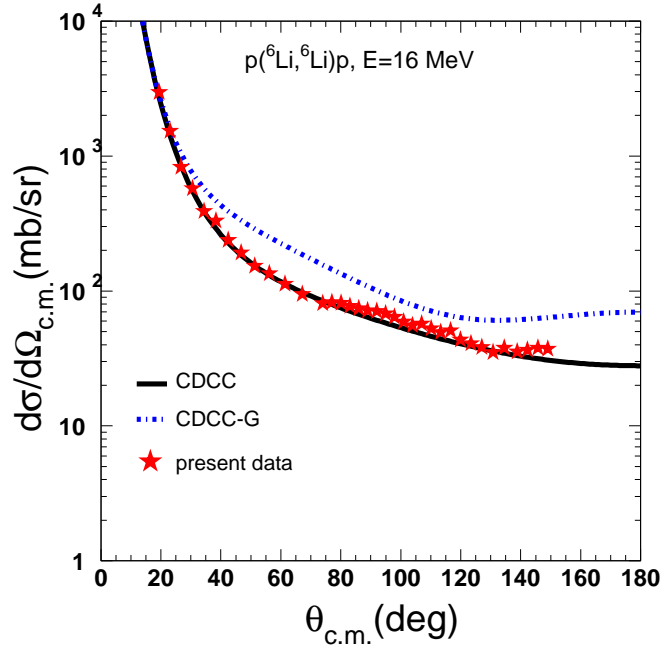


Figure 4.12: Same as in Figure 4.9 but at the energy of 16 MeV (2.67 MeV/u).

4.2.2 Breakup

Breakup data are compared with the full CDCC angular distributions, denoted with the black solid lines, in Figures 4.13 and 4.14 for the energies of 29 and 25 MeV respectively. As it can be seen, the agreement into the error is satisfactory, although the calculations suggest lower breakup cross sections. In the same figures, CDCC calculations taking into account coupling to the 3^+ resonant state only are presented with the red dotted-dashed lines. We can see that, the sequential breakup due to the first resonance state (3^+) accounts for ~ 50 - 60% of the total breakup cross section for the highest two energies. Although we have not breakup data for the lower energies at 16 and 20 MeV, but where we have data for elastic scattering, for reason of completeness we present in Figure 4.15, the energy dependence of the breakup cross sections from 16 to 29 MeV (full CDCC calculations and calculations referring only to resonant breakup). It can be seen that for the lower energies the resonant breakup comprises $\sim 38\%$ for the energy of 20 MeV and drops almost to zero at 16 MeV.

Tabulated values of total breakup as well as resonant breakup cross sections obtained by the CDCC calculations are presented in Table 4.6. The experimental breakup cross sections, presented also in Table 4.6, were obtained by assuming the shape of the CDCC angular distri-

butions (see Figure 4.16) for the angular region where experimental breakup data do not exist. The CDCC calculations seem to underestimate the total breakup cross section by $\sim 27\%$ for the energy of 29 MeV while, for the energy at 25 MeV the agreement is satisfactory at least into the error.

It should be noted here that, a third observable measured in the present experiment as a part of an MSc thesis [75] and reported in Ref. [76], is the cross section of the reaction ${}^6\text{Li} + \text{p} \rightarrow {}^4\text{He} + {}^3\text{He}$. As this reaction is the only reaction with significant cross section at the studied energies, it can be compared with the absorption cross section given as output in our FRESKO CDCC calculation. Therefore, we present additionally to the breakup cross sections in Table 4.6, absorption cross sections, obtained by the CDCC calculations to be compared with experimental values [76]. The measurement of the ${}^6\text{Li} + \text{p} \rightarrow {}^4\text{He} + {}^3\text{He}$ reaction was performed simultaneously with the breakup measurement but, with the GLORIA array [117] installed in the scattering chamber. The agreement between the experimental absorption cross section and the theoretical ones is excellent, giving further support to the global interpretation of the ${}^6\text{Li} + \text{p}$ reaction in a CDCC framework and in the validity of the experimental data.

In the same table, the reorientation cross section, which represents the flux that is lost to the 1^+ ground state of ${}^6\text{Li}$ coupling the different m sub-states, is also shown. This quantity is not possible to be measured and does not affect the energy of the outgoing ${}^6\text{Li}$ or any of the fragments. Nevertheless, it is a real effect which changes the elastic scattering angular distribution and the total reaction cross section [172]. Finally, the total reaction cross sections according to the CDCC calculations are also presented.

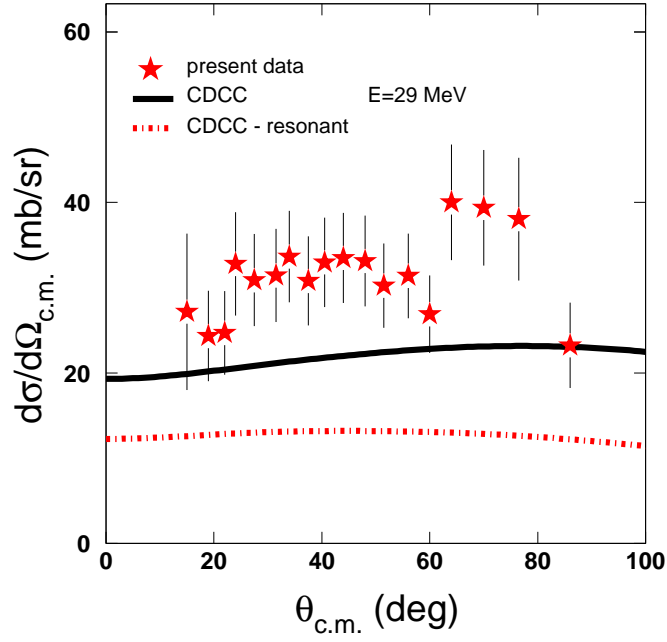


Figure 4.13: *Experimental and theoretical angular distributions in the center of mass frame, for the breakup of ${}^6\text{Li}$ on proton target at 29 MeV (4.83 MeV/u). The experimental data, referring to the first kinematical solution, are designated with red stars. The black solid line represents a full CDCC calculation while the red dotted-dashed line represents a CDCC calculation taking account coupling only to first resonance (3^+).*

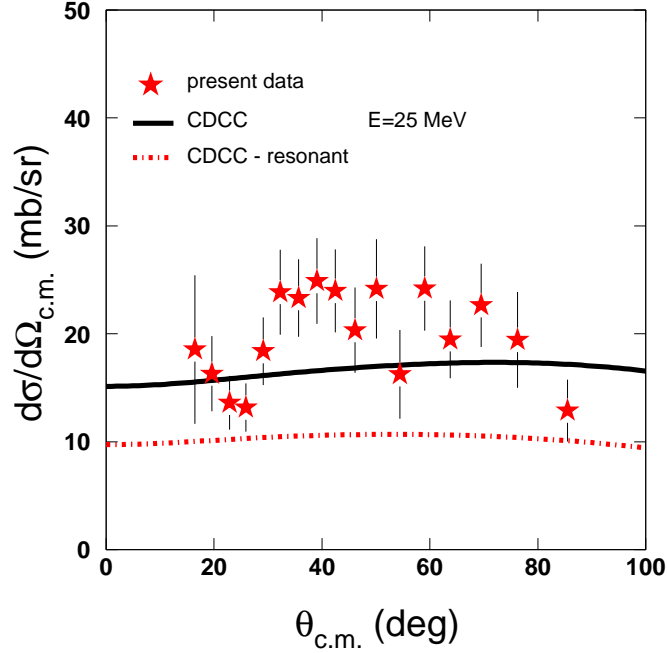


Figure 4.14: Same as in Figure 4.13 but for at energy of 25 MeV (4.17 MeV/u).

Table 4.6: Reaction cross sections for the system ${}^6\text{Li} + \text{p}$. Experimental breakup cross sections, σ_{br} and CDCC breakup cross sections, σ_{br}^{CDCC} , are presented in second and third column respectively. The numbers at the fourth column are the values of the resonant breakup according to CDCC calculations (σ_{resbr}^{CDCC}). Also, experimental absorption cross sections measured previously via the reaction ${}^6\text{Li} + \text{p} \rightarrow {}^3\text{He} + {}^4\text{He}$, σ_{abs} [76] as well as absorption cross sections according to CDCC, σ_{abs}^{CDCC} , are presented at the fifth and sixth column respectively. The reorientation cross sections due to the 1^+ ground state of ${}^6\text{Li}$, σ_{reor}^{CDCC} , and the total reaction cross sections, σ_{tot}^{CDCC} , are shown in the last two columns.

E (MeV)	σ_{br}	σ_{br}^{CDCC}	σ_{resbr}^{CDCC}	σ_{abs}	σ_{abs}^{CDCC}	σ_{reor}^{CDCC}	σ_{tot}^{CDCC}
29	370±64	269.4	143.3	95±2	109.5	72.4	451.3
25	235±46	200.0	117.0	131±6	133.0	98.7	431.7
20	-	102.9	37.5	140±8	162.0	123.4	388.3
16	-	69.7	0.03	111±2	130.7	141.5	341.9

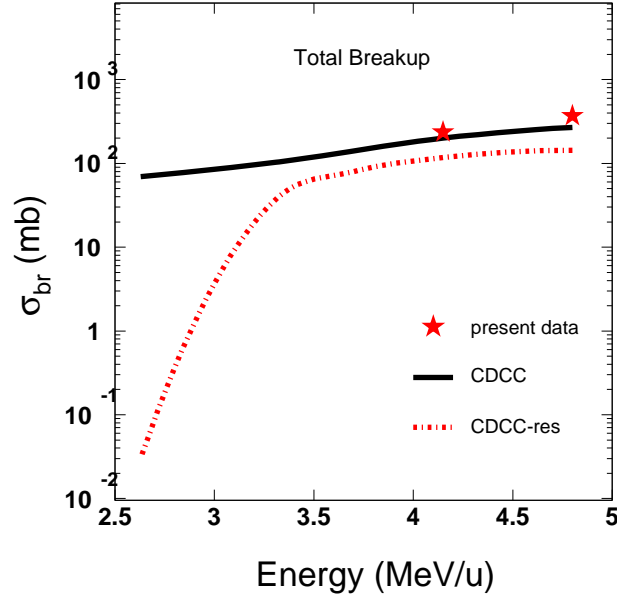


Figure 4.15: *Energy dependence of the total breakup cross sections. Experimental total breakup cross sections, designated with the red stars, are compared with the total breakup as well as the resonant breakup values obtained by the CDCC calculations.*

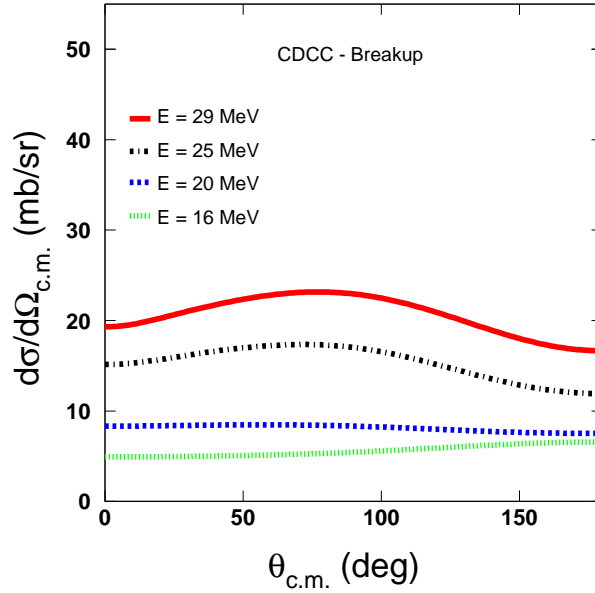


Figure 4.16: *CDCC breakup angular distributions for all the energies in the full angular range $\theta_{c.m.} = 0^\circ - 180^\circ$.*

Chapter 5

Conclusions

In the present work, elastic scattering measurements for the ${}^6\text{Li} + \text{p}$ system were performed at four near barrier energies, namely 16, 20, 25 and 29 MeV, in inverse kinematics with the MAGNEX spectrometer [80–89]. In the same experiment exclusive breakup measurements were obtained at 25 and 29 MeV. Both experimental results were considered in a CDCC framework.

From the present analysis, significant conclusions can be drawn and may be summarized as follows:

1. The present elastic scattering data in inverse kinematics are found in good consistency with previous data obtained in direct kinematics. As the present data extend to more forward angles than the previous ones, where the scattering is Rutherford, they validate (or not) their normalization.
2. The elastic scattering data are considered in the microscopic approach of the Jeukenne-Lejeune-Mahaux (JLM) potential [5] (without any coupling), which fails to reproduce the data. It should be noted that this is the first time that the JLM model is tested both for a very light weakly bound projectile as ${}^6\text{Li}$ and at very low energies $E = 2.6 - 4.8$ MeV/u.
3. Extensive Continuum Discretized Coupled Channel (CDCC) calculations were performed and compared with the elastic scattering and breakup data. The description of the elastic scattering experimental data is excellent while, the description of the breakup data is satisfactory although the trend of CDCC suggests lower breakup cross sections. Total breakup cross sections were obtained integrating the differential cross sections by

assuming the shape of the CDCC angular distributions for the angular region where experimental breakup data do not exist. According to the CDCC calculations, the contribution of breakup due to the first resonance comprises 50-60 % of the total value for the two higher energies, ~ 38 % for 20 MeV and ~ 0.04 % for the lower energy of 16 MeV.

4. Monte Carlo simulations imitating the CDCC model [155, 156] describe very well the experimental energy distributions of the breakup fragments, validating the philosophy of the continuum discretization behind the CDCC approach.
5. Comparing full CDCC calculations with one-channel calculations as well as calculations allowing coupling only to the direct excitation of the continuum, we can see that coupling to the full continuum (direct and resonant) is strong and adequate in order to describe the elastic scattering data in the most effective way. Nevertheless, the most important coupling at all energies is the coupling to resonant breakup while, the coupling to direct breakup has in principle a small influence, which becomes larger at the highest energies. This behavior of weak coupling to direct breakup and strong coupling to the resonant breakup is in accordance with similar findings of ${}^6\text{Li}$ scattering on medium and heavy mass targets such as ${}^{64}\text{Zn}$ [66] and ${}^{144}\text{Sm}$ [67].
6. At the lower energies, according to the CDCC calculations, the coupling to 3^+ resonance is very strong although, the resonant breakup cross section seems to be very low. In particular, at 16 MeV, the resonant breakup cross sections was only 0.03 mb in comparison with a total breakup of 69.7 mb. Such a striking situation was recently reported for the elastic scattering of ${}^7\text{Li} + \text{p}$ [78], where although the resonant breakup was ~ 0.5 mb out of a total breakup cross section of ~ 66 mb, the coupling to the resonant breakup was dominant. This interesting phenomenon may be an example of a "virtual" coupling to continuum.
7. The absorption cross section given as output in our CDCC calculation is compared with the experimental cross section of the reaction ${}^6\text{Li} + \text{p} \rightarrow {}^4\text{He} + {}^3\text{He}$, the only available reaction channel with significant probability. The measurement of this reaction was performed simultaneously with the present one but comprised the subject of an Msc thesis and was reported before [75, 76]. The agreement between the experimental absorption cross section and the theoretical one for all energies is excellent, giving further support to the global interpretation of the ${}^6\text{Li} + \text{p}$ reaction in a CDCC framework and the validity of the experimental data.

8. The validity of the present elastic scattering data was also checked into the global CDCC framework applied previously by Guo et al. [39] for ${}^6\text{Li} + \text{p}$ in a wide energy range from 5 to 72 MeV/u. The calculations [171] using the energy-dependence proposed in Ref. [39] are in fair agreement with the experimental data in lower energies and larger angles and in good agreement with the data at the higher energies.

Finally, we should underline that our technique, for measurements at a close to zero angle, obtained with the MAGNEX spectrometer, is well established, and it can be applied in future measurements with stable weakly bound or radioactive projectiles. It would be very interesting to perform more exclusive breakup measurements as well as elastic scattering and other involved reaction measurements in order to perform a global investigation into the CDCC framework, using similar stable weakly bound or radioactive projectiles on light targets in inverse kinematics. The MAGNEX spectrometer gives us the opportunity to perform such experiments obtaining data of rare quality. Into this plan has been proposed by Prof. A. Pakou, the study of the ${}^6\text{Li} + {}^1\text{H}$ [73, 74, 76] and ${}^7\text{Li} + {}^1\text{H}$ [77, 78] which have been already performed while, an experiment related with the study of ${}^9\text{Be} + \text{p}$ system [79] is scheduled to be performed during 2017.

In summary, exclusive breakup measurements performed for the first time at near barrier energies ($\sim 5 \times V_{C.b.}$), considered with elastic scattering and reaction cross sections measurements, performed in the same experiment, present in total a very good agreement with CDCC calculations. The sequential excitation to the first resonance (3^+) at 2.186 MeV is strong and likewise is the effect on elastic scattering due to coupling to this resonant state. The direct excitation to continuum is substantial and likewise its effect on elastic scattering but only for the highest energy. As we go lower in energy this effect is reduced and become unimportant at the lowest energy of 16 MeV (~ 2.7 MeV/u). It should be stressed out that at this low energy, although the direct breakup is substantial and the resonant breakup is negligible, the dominant coupling to breakup is the resonant one. Further on, the JLM model was tested for the first time from the point of view of a very light weakly bound projectile as ${}^6\text{Li}$ as well as at very low energies, $E = 2.6 - 4.8$ MeV/u. The model was not found adequate to describe the elastic scattering data. Finally, it should be noted that our technique is well-established both experimentally and theoretically allowing the study of similar systems with stable weakly bound or radioactive projectiles on proton/deuteron targets, with the MAGNEX spectrometer.

The results of the present work have been reported in peer-reviewed scientific journals in Refs. [73, 74] as well as to conference proceedings in Refs. [173–175].

Bibliography

- [1] N. Keeley, N. Alamanos, K. W. Kemper, K. Rusek, *Prog. Part. Nucl. Phys.* 63, 396 (2009).
- [2] N. Keeley, K. W. Kemper, and K. Rusek, *Eur. Phys. J. A* 50, 145 (2014).
- [3] L. F. Canto, P. R. S. Gomes, R. Donangelo, J. Lubian, M. S. Hussein, *Phys. Reports* 596, 1 (2015).
- [4] P. R. S. Gomes, J. Lubian, L. F. Canto, D. R. Otomar, D. R. Mendes Junior, P. N. de Faria, R. Linares, L. Sigaud, J. Rangel, J. L. Ferreira, E. Ferioli, B. Paes, E. N. Cardozo, M. R. Cortes, M. J. Ermamatov, P. Lotti, and M. S. Hussein, *Few Body Systems* 57, 165 (2016).
- [5] J. P. Jeukenne, A. Lejeune, and C. Mahaux, *Phys. Rev. C* 16, 80 (1977).
- [6] N. Alamanos, A. Pakou, A. Lagoyannis, and A. Musumarra, *Nucl. Phys. A* 660, 406 (1999).
- [7] A. Pakou, N. Alamanos, P. Roussel-Chomaz, F. Auger, D. Rosengrant, and A. de Vismes, *Nucl. Phys. A* 691, 661 (2001).
- [8] N. Alamanos, F. Auger, B. A. Brown, and A. Pakou, *J. Phys. G* 24, 1541 (1998).
- [9] A. de Vismes, P. Roussel-Chomaz, W. Mittig, A. Pakou, N. Alamanos, F. Auger, J. -C. Angelique, J. Barrette, A. V. Belozyorov, C. Borcea, W. N. Catford, M. D. Cortina-Gil, Z. Dlouhy, A. Gillibert, V. Lapoux, A. Lepine-Szily, S. M. Lukyanov, F. Marie, A. Musumarra, F. de Oliveira, N. A. Orr, S. Ottini-Hustache, Y. E. Penionzhkevich, F. Sarazin, H. Savajols, and N. Skobelev, *Phys. Lett. B* 505, 15 (2001).
- [10] V. Lapoux, N. Alamanos, F. Auger, A. Drouart, A. Gillibert, C. Jouanne, G. Lobo, L. Nalpas, A. Obertelli, E. Pollacco, R. aabe, F. Skaza, J. -L. Sida, D. Beaumel, E.

- Becheva, Y. Blumenfeld, F. Delaunay, L. Giot, E. Khan, A. Lagoyannis, A. Musumarra, P. Navratil, A. Pakou, P. Roussel-Chomaz, H. Savajols, J. -A. Scarpaci, S. Stepantsov, R. Wolski, and T. Zerguerras, Nucl. Phys. A 722, 49c (2003).
- [11] F. Skaza, N. Keeley, V. Lapoux, N. Alamanos, F. Auger, D. Beaumel, E. Becheva, Y. Blumenfeld, F. Delaunay, A. Drouart, A. Gillibert, L. Giot, K. W. Kemper, R. S. Mackintosh, L. Nalpas, A. Pakou, E. C. Pollacco, R. Raabe, P. Roussel-Chomaz, J. -A. Scarpaci, J. -L. Sida, S. Stepantsov, and R. Wolski, Phys. Lett. B 619, 82 (2005).
- [12] C. Jouanne, V. Lapoux, F. Auger, N. Alamanos, A. Drouart, A. Gillibert, G. Lobo, A. Musumarra, L. Nalpas, E. Pollacco, J. -L. Sida, M. Trotta, Y. Blumenfeld, E. Khan, T. Suomijarvi, T. Zerguerras, P. Roussel-Chomaz, H. Savajols, A. Lagoyannis, and A. Pakou, Phys. Rev. C 72, 014308 (2005).
- [13] A. Gillibert, N. Alamanos, M. Alvarez, F. Auger, D. Beaumel, E. Becheva, Y. Blumenfeld, R. Dayras, F. Delaunay, A. Drouart, G. de France, L. Giot, B. Jurado, N. Keeley, K. W. Kemper, V. Lapoux, W. Mittig, X. Mougeot, L. Nalpas, A. Obertelli, N. Patronis, A. Pakou, E. C. Pollacco, R. Raabe, P. Roussel-Chomaz, F. Rejmund, M. Rejmund, H. Savajols, J. A. Scarpaci, J. L. Sida, F. Skaza, S. Stepantsov, Ch. Theisen and R. Wolski, Nucl. Phys. A 787, 423c (2007).
- [14] N. Alamanos and P. Roussel-Chomaz, Ann. Phys. (Paris, Fr.) 21, 601 (1996).
- [15] V. Lapoux and N. Alamanos Eur. Phys. J. A 51, 91 (2015).
- [16] A. Lagoyannis, Ph.D. thesis - University of Ioannina (2001).
- [17] S. Mellema, R. W. Finlay, F. S. Dietrich, and F. Petrovich, Phys. Rev. C 28, 2267 (1983).
- [18] L. F. Hansen, F. S. Dietrich, B. A. Pohl, C. H. Poppe, and C. Wong, Phys. Rev. C 31, 111 (1985).
- [19] J. S. Petler, M. S. Islam, R. W. Finlay, and F. S. Dietrich, Phys. Rev. C 32, 673 (1985).
- [20] F. S. Dietrich, R. W. Finlay, S. Mellema, G. Randers-Pehrson, and F. Petrovich, Phys. Rev. Lett. 51, 1629 (1983).
- [21] F. Petrovich, S. K. Yoon, M. J. Threapleton, R. J. Philpott, J. A. Carr, F. S. Dietrich, and L. F. Hansen, Nucl. Phys. A 563, 387 (1993).

- [22] N. Patronis, A. Pakou, D. Pierroutsakou, A. M. Sanchez-Benitez, L. Acosta, N. Alamanos, A. Boiano, G. Inglis, D. Filipescu, T. Glodariu, A. Guglielmetti, M. La Commar, G. Lalazissis, I. Martel, C. Mazzocchi, M. Mazzocco, P. Molini, C. Parascandolo, M. Sandoli, C. Signorini, R. Silvestri, F. Soramel, E. Stiliaris, M. Romoli, A. Trzcinska, K. Zerva, E. Vardaci and A. Vitturi, *Phys. Rev. C* 85, 024609 (2012).
- [23] J. N. Bahcall, W. F. Huebner, S. H. Lubow, P. D. Parker, and R. K. Ulrich, *Rev. Mod. Phys.* 54, 767 (1982).
- [24] J. Cruz, H. Luis, M. Fonseca, Z. Fulop, G. Gyurky, F. Raiola, M. Aliotta, K. U. Kettner, A. P. Jesus, J. P. Ribeiro, F. C. Barker, and C. Rolfs, *Journal of Phys. G* 35, 014004 (2008).
- [25] L. Lamia, C. Spitaleri, R. G. Pizzone, E. Tognelli, A. Tumino, S. Degl Innocenti, P. G. Prada Moroni, M. La Cognata, L. Pappalardo, and M. L. Sergi, *Astrophys. Journ.*, 768, 65 (2013).
- [26] R. E. Tribble, C. A. Bertulani, M. La Cognata, A. M. Mukhamedzhanov, and C. Spitaleri, *Rep. Prog. Phys.* 77, 106901 (2014).
- [27] J. R. MacNally, *Nuclear Fusion* 11, 187 (1971).
- [28] D. Ichinkhorloo, T. Matsumoto, Y. Hirabayashi, K. Kato, and S. Chiba, *Journal of Nuclear Science and Technology* 48, 1357 (2011).
- [29] G. Casini, *Engineering Aspects of Thermonuclear Fusion Reactors*, Harwood Academic Publishers GmbH (1981).
- [30] M. Skill, R. Baumann, G. Keil, N. Kniest, E. Pfaff, M. Preiss, G. Reiter, G. Clausnitzer, M. Haller, and W. Kretschmer, *Nucl. Phys. A* 581, 93 (1995).
- [31] W. D. Harrison and A. B. Whitehead, *Phys. Rev.* 132, 2607 (1963).
- [32] M. Haller, M. Betz, W. Kretschmer, A. Rauscher, R. Schmitt, and W. Schuster, *Nucl. Phys. A* 496, 189 (1989).
- [33] C. Petitjean, L. Brown, and R. G. Seyler, *Nucl. Phys. A* 129, 209 (1969)
- [34] M. Haller, W. Kretschmer, A. Rauscher, R. Schmitt, and W. Schuster, *Nucl. Phys. A* 496, 205 (1989).
- [35] J. A. McCray, *Phys. Rev.* 130, 2034 (1963).

- [36] K. H. Bray, M. Jain, K. S. Jayaraman, G. Lobianco, G. A. Moss, W. T. H. Van Oers, D. O. Wells, and F. Petrovich, Nucl. Phys. A 189, 35 (1972).
- [37] B. A. Mughrabi, Z. El Itaoui, P. J. Ellis, and Y. C. Tang, Phys. Rev C 29, 29 (1984).
- [38] K. Rusek, K. W. Kemper, and R. Wolski, Phys. Rev. C 64, 044602 (2001).
- [39] H. Guo, Y. Watanabe, T. Matsumoto, K. Ogata, and M. Yahiro, Phys. Rev C 87, 024610 (2013).
- [40] T. Matsumoto, D. Ichinkhorloo, Y. Hirabayashi, K. Kato, and S. Chiba, Phys. Rev C 83, 064611 (2011).
- [41] M. Y. H. Farag, E. H. Esmael, and H. M. Maridi, Phys. Rev. C 88, 064602 (2013).
- [42] A. Pakou, N. Alamanos, N. M. Clarke, N. J. Davis, G. Doukelis, G. Kalyva, M. Kokkoris, A. Lagoyannis, T. J. Mertzimekis, A. Musumarra, N. G. Nicolis, C. Papachristodoulou, N. Patronis, G. Perdikakis, D. Pierroutsakou, D. Roubos, K. Rusek, S. Spyrou, and Ch. Zarkadas, Phys. Lett. B 633, 691 (2006).
- [43] A. Cunsolo, A. Foti, G. Imme, G. Pappalardo, G. Raciti, F. Rizzo, and N. Saunier, Nuovo Cimento 85, 343 (1985).
- [44] F. A. Souza, N. Carlin, C. Beck, N. Keeley, A. Diaz-Torres, R. Liguori Neto, C. Siqueira-Mello, M. M. de Moura, M. G. Munhoz, R. A. N. Oliveira, M. G. Del Santo, A. A. P. Suaide, E. M. Szanto, and A. Szanto de Toledo, Eur. Phys. Jour. A 44, 181 (2010).
- [45] F. A. Souza, C. Beck, N. Carlin, N. Keeley, R. Liguori Neto, M. M. de Moura, M. G. Munhoz, M. G. Del Santo, A. A. P. Suaide, E. M. Szanto, and A. Szanto de Toledo, Nucl. Phys. A 821, 36 (2009).
- [46] F. A. Souza, N. Carlin, C. Beck, N. Keeley, A. Diaz-Torres, R. Liguori Neto, C. Siqueira-Mello, M. M. de Moura, M. G. Munhoz, R. A. N. Oliveira, M. G. Del Santo, A. A. P. Suaide, E. M. Szanto, and A. Szanto de Toledo, Nucl. Phys. A 834, 420c (2010).
- [47] A. Shrivastava, A. Navin, N. Keeley, K. Mahata, K. Ramachandran, V. Nanal, V. V. Parkar, A. Chatterjee, S. Kailas, Phys. Lett. B 633, 463 (2006).
- [48] D. Chattopadhyay, S. Santra, A. Pal, A. Kundu, K. Ramachandran, R. Tripathi, D. Sarkar, S. Sodaye, B. K. Nayak, A. Saxena, and S. Kailas, Phys. Rev. C 94, 061602(R) (2016).

- [49] D. Scholz, H. Gemmeke, L. Lassen, R. Ost, and K. Bethge, Nucl. Phys. A 288, 351 (1977).
- [50] H. Gemmeke, B. Deluigi, D. Scholz and L. Lassen, Phys. Lett. B 96, 47 (1980).
- [51] D. Scholz, H. Gemmeke, L. Lassen, R. Ost, and K. Bethge, Nucl. Phys. A 288, 351 (1977).
- [52] D. Martinez Heimann, A. J. Pacheco, O. A. Capurro, A. Arazi, C. Balpardo, M. A. Cardona, P. F. F. Carnelli, E. de Barbara, J. O. Fernandez Niello, J. M. Figueira, D. Hojman, G. V. Marti, A. E. Negri, and D. Rodríguez, Phys. Rev. C 89, 014615 (2014).
- [53] R. Kanungo, T. Sinha, C. Samanta, S. Roy, A. Chatterjee, B. J. Roy, and S. Ray, Nucl. Phys. A 599, 579 (1996).
- [54] C. M. Castaneda, H. A. Smith Jr., P. P. Singh, and H. Karwowski, Phys. Rev. C 21, 179 (1980).
- [55] D. H. Luong, M. Dasgupta, D. J. Hinde, R. du Rietz, R. Rafiei, C. J. Lin, M. Evers, and A. Diaz-Torres, Phys. Rev. C 88, 034609 (2013).
- [56] D. H. Luong, M. Dasgupta, D. J. Hinde, R. du Rietz, R. Rafiei, C. J. Lin, M. Evers, and A. Diaz-Torres, Phys. Lett. B 695, 105 (2011).
- [57] R. Ost, K. Bethge, H. Gemmeke, L. Lassen, and D. Scholz, Z. Physik 266, 369 (1974).
- [58] C. Signorini, A. Edifizi, M. Mazzocco, M. Lunardon, D. Fabris, A. Vitturi, P. Scopel, F. Soramel, L. Stroe, G. Prete, E. Fioretto, M. Cinausero, M. Trotta, A. Brondi, R. Moro, G. La Rana, E. Vardaci, A. Ordine, G. Inglima, M. La Commara, D. Pierroutsakou, M. Romoli, M. Sandoli, A. Diaz-Torres, I. J. Thompson, and Z. H. Liu, Phys. Rev. C 67, 044607 (2003).
- [59] N. Heide, D. K. Srivastava and H. Rebel, Phys. Rev. Lett. 63, 601 (1989).
- [60] N. Heide, H. Rebel, V. Corcalciuc, H. J. Gils, H. Jelitto, J. Kiener, J. Wentz, S. Zagromski, and D. K. Srivastava, Nucl. Phys. A 504, 374 (1989).
- [61] S. Santra, V. V. Parkar, K. Ramachandran, U. K. Pal, A. Shrivastava, B. J. Roy, B. K. Nayak, A. Chatterjee, R. K. Choudhury, S. Kailas, Phys. Lett. B 677, 139 (2009).
- [62] Y. Sakuragi, M. Yahiro, and M. Kamimura, Prog. Theor. Phys. Suppl. 89, 136 (1986).

- [63] K. Rusek, N. M. Clarke, and R. P. Ward, *Phys. Rev. C* 50, 2010 (1994).
- [64] K. Rusek, P. V. Green, P. L. Kerr, and K. W. Kemper, *Phys. Rev. C* 56, 1895 (1997).
- [65] Y. Hirabayashi and Y. Sakuragi, *Nucl. Phys. A* 536, 375 (1992).
- [66] J. P. Fernandez-Garcia, M. Zadro, A. Di Pietro, P. Figuera, M. Fisichella, O. Goryunov, M. Lattuada, C. Marchetta, A. M. Moro, A. Musumarra, V. Ostashko, M. G. Pellegriti, V. Scuderi, E. Strano, and D. Torresi, *Phys. Rev. C* 92, 054602 (2015).
- [67] A. Gomez Camacho, A. Diaz-Torres, P. R. S. Gomes, and J. Lubian, *Phys. Rev. C* 93, 024604 (2016).
- [68] A. Gomez Camacho, A. Diaz-Torres, P. R. S. Gomes, and J. Lubian, *Phys. Rev. C* 91, 014607 (2015).
- [69] V. Valcovic, C. Joseph, S. T. Emerson, and G. C. Philips, *Nucl. Phys. A* 106, 138 (1968).
- [70] <https://www.lns.infn.it/en/>
- [71] <http://npl.physics.uoi.gr/>
- [72] A. Lagoyannis, F. Auger, A. Musumarra, N. Alamanos, E. C. Pollacco, A. Pakou, Y. Blumenfeld, F. Braga, M. La Commara, A. Drouart, G. Fioni, A. Gillibert, E. Khan, V. Lapoux, W. Mittig, S. Ottini-Hustache, D. Pierroutsakou, M. Romoli, P. Roussel-Chomaz, M. Sandoli, D. Santonocito, J. A. Scarpaci, J. L. Sida, T. Suomijarvi, S. Karataglidis, and K. Amos, *Phys. Lett. B* 518, 27 (2001).
- [73] V. Soukeras, A. Pakou, F. Cappuzzello, L. Acosta, C. Agodi, N. Alamanos, M. Bondi, D. Carbone, M. Cavallaro, A. Cunsolo, M. De Napoli, A. Di Pietro, J. P. Fernandez-Garcia, P. Figuera, M. Fisichella, A. Foti, N. Keeley, G. Marquinez-Duran, I. Martel, M. Mazzocco, D. Nicolosi, D. Pierroutsakou, K. Rusek, O. Sgouros, E. Stiliaris, E. Strano, and D. Torresi, *Phys. Rev. C* 91, 057601 (2015).
- [74] V. Soukeras, A. Pakou, F. Cappuzzello, L. Acosta, C. Agodi, N. Alamanos, S. Calabrese, D. Carbone, M. Cavallaro, A. Cunsolo, A. Di Pietro, J. P. Fernandez-Garcia, P. Figuera, M. Fisichella, A. Foti, N. Keeley, G. Marquinez-Duran, I. Martel, M. Mazzocco, D. Pierroutsakou, K. Rusek, G. Santagati, O. Sgouros, E. Stiliaris, E. Strano, D. Torresi, and K. Zerva, accepted for publication in *Phys. Rev. C*.
- [75] Ch. Betsou, M.Sc. thesis - University of Ioannina (2015).

- [76] Ch. Betsou, A. Pakou, F. Cappuzzello, L. Acosta, C. Agodi, X. Aslanoglou, D. Carbone, M. Cavallaro, A. Di Pietro, J. P. Fernandez-Garcia, P. Figuera, M. Fisichella, A. Foti, N. Keeley, G. Marquinez-Duran, I. Martel, M. Mazzocco, N. G. Nicolis, D. Pierroutsakou, K. Rusek, O. Sgouros, V. Soukeras, E. Stiliaris, E. Strano, and D. Torresi, *Eur. Phys. J. A* 51, 86 (2015).
- [77] A. Pakou, V. Soukeras, F. Cappuzzello, L. Acosta, C. Agodi, X. Aslanoglou, S. Calabrese, D. Carbone, M. Cavallaro, A. Foti, N. Keeley, G. Marquinez-Duran, I. Martel, M. Mazzocco, C. Parascandolo, D. Pierroutsakou, K. Rusek, O. Sgouros, E. Strano, and V. A. B. Zagatto, *Phys. Rev. C* 94, 014604 (2016).
- [78] A. Pakou, O. Sgouros, V. Soukeras, F. Cappuzzello, N. Keeley, L. Acosta, C. Agodi, X. Aslanoglou, S. Calabrese, D. Carbone, M. Cavallaro, A. Foti, G. Marquinez-Duran, I. Martel, M. Mazzocco, C. Parascandolo, D. Pierroutsakou, K. Rusek, E. Strano, V. A. B. Zagatto, and K. Zerva, *Phys. Rev. C* 95, 044615 (2017).
- [79] A. Pakou, Elastic scattering, breakup and clustering modes for ${}^9\text{Be}+p$ at above barrier energies, accepted proposal by INFN-LNS PAC, to be performed in 2017.
- [80] F. Cappuzzello, C. Agodi, D. Carbone and M. Cavallaro, *Eur. Phys. J. A* 52, 167 (2016).
- [81] F. Cappuzzello, D. Carbone, M. Cavallaro, and A. Cunsolo, MAGNEX: An innovative large acceptance spectrometer for nuclear reaction studies, Chapter in edited collection: Magnets: Types, Uses and Safety, pp. 1-63, Ed.: Takashiro Akitsu, Nova Science Publishers, Inc, ISBN: 978-1-61470-251-1 (2011).
- [82] A. Cunsolo, F. Cappuzzello, M. Cavallaro, A. Foti, A. Khouaja, S. E. A. Orrigo, J. S. Winfield, L. Gasparini, G. Longo, T. Borello-Lewin, M. R. D. Rodrigues, M. D. L. Barbosa, C. Nociforo, and H. Petrascu, *Eur. Phys. J. Special Topics* 150, 343 (2007).
- [83] F. Cappuzzello, M. Cavallaro, A. Cunsolo, A. Foti, D. Carbone, S. E. A. Orrigo, and M. R. D. Rodrigues, *Nucl. Instrum. Methods Phys. Res., Sect. A* 621, 419 (2010).
- [84] M. Cavallaro, F. Cappuzzello, D. Carbone, A. Cunsolo, A. Foti, A. Khouaja, M. R. D. Rodrigues, J. S. Winfield, and M. Bondi, *Eur. Phys. J. A* 48, 59 (2012).
- [85] D. Carbone, F. Cappuzzello, and M. Cavallaro, *Eur. Phys. J. A* 48, 60 (2012).
- [86] A. Cunsolo, F. Cappuzzello, A. Foti, A. Lazzaro, A. L. Melita, C. Nociforo, V. Shchepunov, and J. S. Winfield, *Nucl. Instrum. Methods Phys. Res., Sect. A* 484, 56 (2002).

- [87] A. Cunsolo, F. Cappuzzello, A. Foti, A. Lazzaro, A. L. Melita, C. Nociforo, V. Shchepunov, and J. S. Winfield, Nucl. Instrum. Methods Phys. Res., Sect. A 481, 48 (2002).
- [88] M. Cavallaro, Ph.D. thesis - University of Catania (2008).
- [89] D. Carbone, Ph.D. thesis - University of Catania (2012).
- [90] K. S. Krane, Introductory Nuclear Physics, John Wiley and Sons, 2nd ed. (1988).
- [91] S. S. M. Wong, Introductory Nuclear Physics, Wiley-VCH Verlag GmbH, 2nd ed. (1998).
- [92] P. E. Hodgson, E. Gadioli, and E. Gadioli Ebra, Introductory Nuclear Physics, Oxford Science Publications (1997).
- [93] R. G. Newton, Scattering Theory of Waves and Particles, McGraw-Hill, Inc. (1966)
- [94] G. R. Satchler, Introduction to nuclear reactions, MacMillan Education LTD, 2nd ed. (1990).
- [95] P. E. Hodgson, Rep. Prog. Phys. 34, 765 (1971).
- [96] R. R. Roy and B. P. Nigam, Nuclear Physics Theory and Experiment, John Wiley and Sons, Inc. (1967).
- [97] V. Soukeras, M.Sc. dissertation - University of Ioannina (2013).
- [98] H. Feshbach, C. E. Porter, and V. F. Weisskopf, Phys. Rev. 96, 448 (1954).
- [99] A. G. Sitenko, Theory of Nuclear Reactions, World Scientific (1990).
- [100] K. Zerva, PhD thesis - University of Ioannina (2013).
- [101] D. Roubos, A. Pakou, N. Alamanos, and K. Rusek, Phys. Rev. C 73, 051603(R) (2006).
- [102] M. E. Cage, A. J. Cole, and G. J. Pyle, Nucl. Phys. A 201, 418 (1973).
- [103] C. Tenreiro, J. C. Acquadro, P. A. B. Freitas, R. Liguori Neto, G. Ramirez, N. Cuevas, P. R. S. Gomes, R. Cabezas, R. M. Anjos, and J. Copnell, Phys. Rev. C 53, 2870 (1996).
- [104] A. Zerwekh, R. Liguori Neto, N. Added, J. C. Acquadro, N. Carlin, M. Frizzarini, F. Malandrino, J. Lubian, R. Cabezas, P. R. S. Gomes, R. M. Anjos, G. M. Santos, A. M. M. Maciel, C. Muri, S. B. Moraes, G. Ramirez, and C. Tenreiro, Phys. Rev. C 58, 3445 (1998).

- [105] J. G. Cramer and R. M. DeVries, Phys. Rev. C 22, 91 (1980).
- [106] K. Rusek, Z. Moroz, R. Caplar, P. Egelhof, K.-H. Mobius, E. Steffens, I.K. Oenig, A. Weller, and D. Fick, Nucl. Phys. A 407, 208 (1983).
- [107] N. Alamanos and A. Gillibert, Selected Topics in Reaction Studies with Exotic Nuclei, Lect. Notes Phys. 651, 295 (2004).
- [108] G. R. Satchler and W. G. Love, Phys. Rep. 55, 183 (1979).
- [109] D. T. Khoa and W. von Oertzen, Phys. Lett. B 304, 8 (1993).
- [110] E. Bauge, J. P. Delaroche, and M. Girod, Phys. Rev. C 58, 1118 (1998).
- [111] R. J. de Meijer and R. Kamermans, Rev. Mod. Phys. 57, 147 (1985).
- [112] A. M. Moro, J. Lei, M. Gomez-Ramos, J. M. Arias, R. de Diego, J. Gomez-Camacho, and J. A. Lay, Acta Physica Polonica B 47, 821 (2015).
- [113] R. C. Johnson and R. J. R. Soper, Phys. Rev. C 1, 976 (1970).
- [114] G. Rawitscher, Phys. Rev. C 9, 2210 (1974).
- [115] F. Nunes, Continuum-Discretised Coupled Channels methods, Scholarpedia, 6(9), 10497 (2011) (<http://dx.doi.org/10.4249/scholarpedia.10497>).
- [116] I. J. Thompson, Comput. Phys. Rep. 7, 167 (1988).
- [117] G. Marquinez-Duran, L. Acosta, R. Berjillos, J. A. Duenas, J. A. Labrador, K. Rusek, A. M. Sanchez-Benitez, and I. Martel, Nucl. Instrum. Methods Phys. Res., Sect. A 755, 69 (2014).
- [118] W. W. Buechner, R. J. Van de Graaff, E. N. Strait, C. G. Stergiopoulos, and A. Sperduto, Phys. Rev. 74, 1226 (1948).
- [119] W. W. Buechner, E. N. Strait, C. G. Stergiopoulos, and A. Sperduto, Phys. Rev. 74, 1569 (1948).
- [120] J. D. Cockcroft, J. Sci. Instrum. 10, 71 (1933).
- [121] Lord Rutherford, C. E. Wynn-Williams, W. B. Lewis, and B. V. Bowden, Roy. Soc. Proc. A 139, 617 (1933).

- [122] C. W. Snyder, C. C. Lauritsen, W. A. Fowler, and S. Rubin, *Phys. Rev.* 74, 1564 (1948).
- [123] H. A. Enge, *Nucl. Instrum. Methods* 162, 161 (1979).
- [124] C. P. Browne and W. W. Buechner, *Rev. Sci. Instrum.* 27, 899 (1956).
- [125] J. Borggreen, B. Elbek, and L. Perch Nielsen, *Nucl. Instrum. Methods* 24, 1 (1963).
- [126] J. E. Spencer and H. A. Enge, *Nucl. Instrum. Methods* 49, 181 (1967).
- [127] D. L. Hendrie, J. R. Meriwether, F. Selph, D. Morris, and C. Glasshausser, *Bull. Am. Phys. Soc.* 15, 650 (1970).
- [128] H. Savajols (for the VAMOS Collaboration), *Nucl. Instrum. Methods Phys. Res., Sect. A* 204, 146 (2003).
- [129] S. Shimoura, *Nucl. Instrum. Methods Phys. Res., Sect. B* 266, 4131 (2008).
- [130] K. Yoneda, N. Iwasa, T. Kawabata, T. Kobayashi, T. Kubo, K. Kusaka, T. Motobayashi, T. Murakami, Y. Nakai, T. Nakamura, J. Ohnishi, H. Okuno, H. Otsu, H. Sakurai, H. Sato, Y. Satou, K. Sekiguchi, and Y. Togano, *RIKEN Accel. Prog. Rep.* 42, 26 (2009).
- [131] A. M. Stefanini, L. Corradi, G. Maron, A. Pisent, M. Trotta, A.M. Vinodkumar, S. Beghini, G. Montagnoli, F. Scarlassara, G. F. Segato, A. De Rosa, G. Inghima, D. Pierroutsakou, M. Romoli, M. Sandoli, G. Pollarolo, and A. Latina, *Nucl. Phys. A* 701, 217c (2002).
- [132] A. Lazzaro, F. Cappuzzello, A. Cunsolo, M. Cavallaro, A. Foti, S. E. A. Orrigo, M. R. D. Rodrigues, and J. S. Winfield, *Nucl. Instrum. Methods Phys. Res., Sect. A* 591, 394 (2008).
- [133] A. Lazzaro, F. Cappuzzello, A. Cunsolo, M. Cavallaro, A. Foti, S. E. A. Orrigo, M. R. D. Rodrigues, and J. S. Winfield, *Nucl. Instrum. Methods Phys. Res., Sect. A* 585, 136 (2008).
- [134] F. Cappuzzello, M. Cavallaro, C. Agodi, M. Bondi, D. Carbone, A. Cunsolo, and A. Foti, *Eur. Phys. J. A* 51, 145 (2015).
- [135] F. Cappuzzello, C. Agodi, E. Aciksoz, L. Acosta, X. Aslanoglou, N. Auerbach, R. Bijker, D. Bonanno, D. Bongiovanni, T. Borello, S. Boudhaim, M.L. Bouhssa, I. Boztosun, L. Calabretta, A. Calanna, D. Carbone, M. Cavallaro, D. Calvo, E. R. Chávez Lomelí,

- M. Colonna, G. D'Agostino, N. Deshmukh, P. N. de Faria, A. Ferrero, A. Foti, P. Finocchiario, P. R. S. Gomes, V. Greco, A. Hacisalihoglu, Z. Housni, A. Khouaja, J. Inchaou, G. Lanzalone, F. La Via, J. A. Lay, H. Lenske, R. Linares, J. Lubian, F. Iazzi, R. Introzzi, A. Lavagno, D. Lo Presti, N. Medina, D. R. Mendes, A. Muoio, J. R. B. Oliveira, A. Pakou, L. Pandola, D. Rifuggiato, M. R. D. Rodrigues, G. Santagati, E. Santopinto, L. Scaltrito, O. Sgouros, S. O. Solakci, V. Soukeras, S. Tudisco, R. I. M. Vsevolodovna, and V. Zagatto, *Journal of Physics: Conference Series* 730, 012006 (2016).
- [136] C. Agodi, F. Cappuzzello, F. Balestra, R. Bijker, D. Bonanno, D. Bongiovanni, V. Branchina, L. Calabretta, A. Calanna, D. Calvo, D. Carbone, M. Cavallaro, M. Colonna, N. Deshmukh, S. Ferrero, A. Foti, P. Finocchiario, G. Giraudo, V. Greco, F. Iazzi, R. Introzzi, A. Lavagno, D. Lo Presti, F. Longhitano, A. Muoio, L. Pandola, D. Rifuggiato, M. V. Ruslan, G. Santagati, E. Santopinto, L. Scaltrito, S. Tudisco, V. Zagatto, P. R. Gomes, R. Linares, J. Lubian, N. H. Medina, J. R. B. Oliveira, M. R. D. Rodrigues, T. Borello-Lewin, D. R. Mendes Junior, P. N. de Faria, X. Aslanoglou, A. Pakou, O. Sgouros, and V. Soukeras, *Proceedings of the 14th International Conference on Nuclear Reaction Mechanisms, NRM 2015*, 239 (2015).
- [137] A. Lazzaro, Ph.D. thesis - University of Catania (2003).
- [138] A. Cunsolo, F. Cappuzzello, A. Foti, P. Gangnant, A. Lazzaro, J. F. Libin, A. L. Melita, W. Mittag, C. Nociforo, S. Orrigo, P. Roussel-Chomaz, C. Spitaels, and J. S. Winfield, *Nucl. Instrum. Methods Phys. Res., Sect. A* 495, 216 (2002)
- [139] M. Cavallaro, private communication.
- [140] F. Cappuzzello, D. Carbone, and M. Cavallaro, *Nucl. Instrum. Methods Phys. Res., Sect. A* 638, 74 (2011).
- [141] M. Berz, K. Joh, J. A. Nolen, B. M. Sherrill, and A. F. Zeller, *Phys. Rev. C* 47, 537 (2012).
- [142] K. Makino, and M. Berz, *Nucl. Instrum. Methods Phys. Res., Sect. A* 558, 346 (2006).
- [143] A. Lazzaro, F. Cappuzzello, A. Cunsolo, M. Cavallaro, A. Foti, S. E. A. Orrigo, M. R. D. Rodrigues, J. S. Winfield, and M. Berz, *Nucl. Instrum. Methods Phys. Res., Sect. A* 602, 494 (2009).
- [144] A. Lazzaro, F. Cappuzzello, A. Cunsolo, M. Cavallaro, A. Foti, A. Khouaja, S. E. A. Orrigo, and J. S. Winfield, *Nucl. Instrum. Methods Phys. Res., Sect. A* 570, 192 (2007).

- [145] PAW - Physics Analysis Workstation, Application software group, Computer and Networks Division, CERN, Geneva (1995).
- [146] ROOT - Data Analysis Framework, Application software group (<https://root.cern.ch/>).
- [147] R. Brun and F. Rademakers, Nucl. Instrum. Methods Phys. Res., Sect. A 389, 81 (1997).
- [148] W. R. Leo, Techniques for Nuclear and Particle Physics Experiments, Springer-Verlag, 2nd ed. (1994).
- [149] G. F. Knoll, Radiation Detection and Measurement, John Wiley and Sons, Inc., 3rd ed. (1999).
- [150] K. Kleinknecht, Detectors for particle radiation, Cambridge University Press, 2nd ed. (1998).
- [151] O. B. Tarasov and D. Bazin, Nucl. Instrum. Methods Phys. Res., Sect. B 266, 4657 (2008).
- [152] <http://lise.nsl.msui.edu/lise.html>
- [153] D. Nicolosi, Ph.D. thesis - University of Catania (2013).
- [154] V. I. Zagrebaev, A. S. Denikin, A. V. Karpov, A. P. Alekseev, M. A. Naumenko, V. A. Rachkov, V. V. Samarin, and V. V. Saiko, NRV web knowledge base on low-energy nuclear physics (<http://nrv.jinr.ru/>)
- [155] O. Sgouros, V. Soukeras, and A. Pakou, MULTIP: MULTI-Purpose Monte Carlo simulation code for three and four body kinematics, to be published.
- [156] O. Sgouros, Ph.D. thesis - University of Ioannina (2017).
- [157] G. G. Ohlsen, Nucl. Instrum. Methods 37, 240 (1965).
- [158] O. Sgouros, A. Pakou, D. Pierrotsakou, M. Mazzocco, L. Acosta, X. Aslanoglou, Ch. Betsou, A. Boiano, C. Boiano, D. Carbone, M. Cavallaro, J. Grebosz, N. Keeley, M. La Commara, C. Manea, G. Marquez-Duran, I. Martel, N. G. Nicolis, C. Parascandolo, K. Rusek, A. M. Sanchez-Benitez, C. Signorini, F. Soramel, V. Soukeras, C. Stefanini, E. Stiliaris, E. Strano, I. Strojek and D. Torresi, Phys. Rev. C 94, 044623 (2016).
- [159] A. Pakou, Elastic scattering and breakup of $8\text{B} + 208\text{Pb}$ below barrier, accepted proposal by INFN-LNL PAC, to be performed.

- [160] A. Pakou, personal communication
- [161] Y. Hirabayashi, Phys. Rev. C 44, 1581 (1991).
- [162] D. R. Tilley, C. M. Cheves, J. L. Godwin, G. M. Haled, H. M. Hofmann, J. H. Kelley, C. G. Sheu, H. R. Weller, Nucl. Phys. A 708, 3 (2002).
- [163] <http://www.nndc.bnl.gov/chart>.
- [164] R. Sherr, J. M. Blair, H. R. Kratz, C. L. Bailey, and R. F. Taschek, Phys. Rev. 72, 662 (1947).
- [165] F. Lahlou, R. J. Slobodrian, P. Bricault, S. S. Dasgupta, R. Roy, and C. Rioux, J. Phys. France 41, 485 (1980).
- [166] D. C. Kocher and T. B. Clegg, Nucl. Phys. A 132, 455 (1969).
- [167] A. S. Wilson, M. C. Taylor, J. C. Legg, and G. C. Phillips, Nucl. Phys. 130, 624 (1969).
- [168] K. Sagara, H. Oguri, S. Shimizu, K. Maeda, H. Nakamura, T. Nakashima, and S. Morinobu, Phys. Rev. C 50, 576 (1994).
- [169] G. Freier, E. Lampi, W. Sleator and J. H. Williams, Phys. Rev. 75, 1345 (1949).
- [170] P. D. Miller and G. C. Phillips, Phys. Rev. 112, 2043 (1958).
- [171] K. Rusek, private communication.
- [172] N. Keeley, private communication.
- [173] V. Soukeras, A. Pakou, F. Cappuzzello, L. Acosta, C. Agodi, N. Alamanos, M. Bondi, D. Carbone, M. Cavallaro, A. Cunsolo, M. De Napoli, A. Di Pietro, J. P. Fernandez-Garcia, P. Figuera, M. Fisichella, A. Foti, N. Keeley, G. Marquinez-Duran, I. Martel, M. Mazzocco, D. Nicolosi, D. Pierroutsakou, K. Rusek, O. Sgouros, E. Stiliaris, E. Strano, and D. Torresi, AIP Conf. Proc. 1645 (2015) 406.
- [174] V. Soukeras, A. Pakou, F. Cappuzzello, L. Acosta, C. Agodi, N. Alamanos, D. Carbone, M. Cavallaro, A. Di Pietro, J.P. Fernandez-Garcia, P. Figuera, M. Fisichella, A. Foti, N. Keeley, G. Marquinez-Duran, I. Martel, M. Mazzocco, D. Pierroutsakou, K. Rusek, O. Sgouros, E. Strano, and D. Torresi, Proceeding of the 3rd one-day Workshop on New Aspects and Perspectives in Nuclear Physics, Pages 61-66 (2016).

- [175] V. Soukeras, A. Pakou, F. Cappuzzello, L. Acosta, C. Agodi, N. Alamanos, M. Bondi, D. Carbone, M. Cavallaro, A. Cunsolo, M. De Napoli, A. Di Pietro, J. P. Fernandez-Garcia, P. Figuera, M. Fisichella, A. Foti, N. Keeley, G. Marquinez-Duran, I. Martel, M. Mazzocco, D. Nicolosi, D. Pierroutsakou, K. Rusek, O. Sgouros, E. Stiliaris, E. Strano, and D. Torresi, Proceeding of the 2nd one-day Workshop on New Aspects and Perspectives in Nuclear Physics, Pages 43-51 (2014).
- [176] J. B. Ball, Kinematics II: A nonrelativistic kinematics FORTRAN program to aid analysis of nuclear reaction angular distribution data, Oak Ridge National Laboratory (1962).

Appendix A

Determination of the effective beam energy

As it was already stated in Chapter 3, the reconstruction procedure does not take into account the energy loss inside the target [89, 153]. Thus, it is necessary to calculate an effective beam energy (E_{beam}^{eff}) which corresponds to a zero-thickness target. The first step in order to do that is the calculation of the reaction energy (E_{react}) assuming that the reaction take place at the middle of the target. Subsequently, the ejectile energy after the target (E_{eject}) should be calculated for each scattering angle. For the sake of simplicity, we assume as scattering angle the angle of the MAGNEX optical axis (θ_{opt}) which is an average between the scattering angles. Finally, the effective beam energy (E_{beam}^{eff}) was determined as the beam energy corresponding to ejectile energy E_{eject} at scattering angle θ_{opt} assuming a zero-thickness target. The determination of the effective beam energy was performed by using the NRV kinematical program [154] as well as the LISE++ program [151, 152] for the calculation of the energy loss. Apparently, due to the use of thin targets, the effective beam energy was slightly different from the projectile beam energy. The procedure is also displayed in Figure A.1.

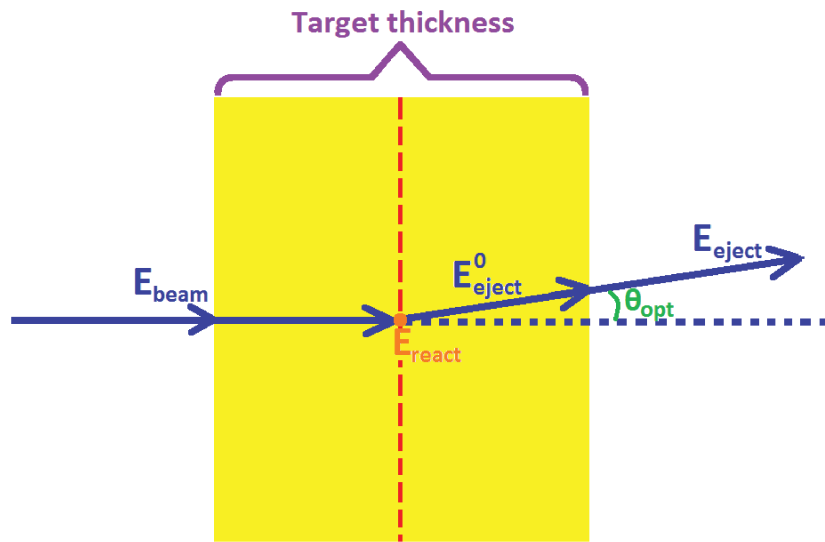


Figure A.1: *Description of the effective beam energy determination.*

Appendix B

Error calculation

B.1 Error calculation for elastic scattering data

As it was already mentioned in Chapter 3, the elastic scattering differential cross section in the laboratory frame was determined by the following formula:

$$\left(\frac{d\sigma_{el}}{d\Omega}\right)_{lab} = \frac{N_{el-net}}{T_{el}\Phi_{el}\Omega_{el}\epsilon} = \frac{N_{el-tot} - N_{el-backg}}{T_{el}\Phi_{el}\Omega_{el}\epsilon} \quad (B.1)$$

where N_{el-net} is the number of counts for a specific laboratory angle after subtracting the background counts $N_{el-backg}$ from the total counts N_{el-tot} , T_{el} and Φ_{el} are the scattering centers and the beam flux respectively, Ω_{el} is the solid angle during the elastic scattering measurement and ϵ is the efficiency of the FPD.

Using the error propagation formula [149], the uncertainty Σ related to the elastic scattering differential cross section is calculated as follows:

$$\Sigma = \pm \sqrt{\left(\frac{\partial\left(\frac{d\sigma}{d\Omega}\right)}{\partial N_{tot}}\Sigma_{N_{tot}}\right)^2 + \left(\frac{\partial\left(\frac{d\sigma}{d\Omega}\right)}{\partial N_{backg}}\Sigma_{N_{backg}}\right)^2 + \left(\frac{\partial\left(\frac{d\sigma}{d\Omega}\right)}{\partial T}\Sigma_T\right)^2 + \left(\frac{\partial\left(\frac{d\sigma}{d\Omega}\right)}{\partial \Phi}\Sigma_{\Phi}\right)^2 + \left(\frac{\partial\left(\frac{d\sigma}{d\Omega}\right)}{\partial \Omega}\Sigma_{\Omega}\right)^2} \quad (B.2)$$

$$\Sigma = \pm \sqrt{\left(\frac{\sqrt{N_{tot}}}{T\Phi\Omega\epsilon}\right)^2 + \left(\frac{\sqrt{N_{backg}}}{T\Phi\Omega\epsilon}\right)^2 + \left(\frac{N_{net}}{T^2\Phi\Omega\epsilon}\Sigma_T\right)^2 + \left(\frac{N_{net}}{T\Phi^2\Omega\epsilon}\Sigma_{\Phi}\right)^2 + \left(\frac{N_{net}}{T\Phi\Omega^2\epsilon}\Sigma_{\Omega}\right)^2} \quad (B.3)$$

$$\Sigma = \pm \sqrt{\frac{N_{tot} + N_{backg}}{(T\Phi\Omega\epsilon)^2} + \left(\frac{d\sigma}{d\Omega}\right)^2 \left(\frac{\Sigma_T^2}{T^2} + \frac{\Sigma_{\Phi}^2}{\Phi^2} + \frac{\Sigma_{\Omega}^2}{\Omega^2}\right)} \quad (B.4)$$

$$\Sigma = \pm \sqrt{\left(\frac{d\sigma}{d\Omega}\right)^2 \left(\frac{N_{tot} + N_{backg}}{N_{net}^2} + \frac{\Sigma_T^2}{T^2} + \frac{\Sigma_\Phi^2}{\Phi^2} + \frac{\Sigma_\Omega^2}{\Omega^2}\right)} \quad (\text{B.5})$$

Thus, the uncertainty Σ_{el} related to the elastic scattering differential cross section was estimated via the following formula:

$$\Sigma_{el} = \pm \left(\frac{d\sigma_{el}}{d\Omega}\right)_{lab} \sqrt{\frac{N_{el-tot} + N_{el-backg}}{(N_{el-net})^2} + \left(\frac{\Sigma_{T_{el}}}{T_{el}}\right)^2 + \left(\frac{\Sigma_{\Phi_{el}}}{\Phi_{el}}\right)^2 + \left(\frac{\Sigma_{\Omega_{el}}}{\Omega_{el}}\right)^2} \quad (\text{B.6})$$

where $\Sigma_{T_{el}}$, $\Sigma_{\Phi_{el}}$ and $\Sigma_{\Omega_{el}}$ are the uncertainties related with the scattering centers, the flux of the beam and the solid angle respectively.

B.2 Error calculation for breakup data

Regarding the breakup process, the double differential cross section in the laboratory system was determined by the following formula:

$$\left(\frac{d^2\sigma_{bu}}{d\Omega_\alpha d\Omega_d}\right)_{lab} = \frac{a_{bu}N_{bu} - \phi a_{car}N_{car}}{T_{bu}\Phi_{bu}\varepsilon_{bu}} \quad (\text{B.7})$$

where N_{bu} and N_{car} are the number of counts for CH_2 and carbon runs respectively while a_{bu} and a_{car} are the efficiency corrections due to reconstruction procedure for the CH_2 and ^{12}C runs respectively. The ϕ is a factor used for normalizing the events obtained with the carbon run to the flux and scattering centers of the CH_2 run. Also, T_{bu} , Φ_{bu} and ε_{bu} are the hydrogen scattering centers of the CH_2 target, the beam flux and the total detection efficiency, respectively.

Defining a parameter B as:

$$B = \left(\frac{d^2\sigma_{bu}}{d\Omega_\alpha d\Omega_d}\right)_{lab} \quad (\text{B.8})$$

and by using the error propagation formula, the uncertainty Σ_B related to the breakup double differential cross section is calculated as follows:

$$\Sigma_B = \pm \sqrt{\left(\frac{\partial B}{\partial N_{bu}}\Sigma_{N_{bu}}\right)^2 + \left(\frac{\partial B}{\partial N_{car}}\Sigma_{N_{car}}\right)^2 + \left(\frac{\partial B}{\partial T_{bu}}\Sigma_{T_{bu}}\right)^2 + \left(\frac{\partial B}{\partial \Phi_{bu}}\Sigma_{\Phi_{bu}}\right)^2 + \left(\frac{\partial B}{\partial \varepsilon_{bu}}\Sigma_{\varepsilon_{bu}}\right)^2} \quad (\text{B.9})$$

$$\Sigma_B = \pm \sqrt{\frac{a_{bu}^2 N_{bu} + \phi^2 a_{car}^2 N_{car}}{(T_{bu} \Phi_{bu} \varepsilon_{bu})^2} + \frac{(a_{bu} N_{bu} - \phi a_{car} N_{car})^2}{(T_{bu} \Phi_{bu} \varepsilon_{bu})^2} \left(\left(\frac{\Sigma_{T_{bu}}}{T_{bu}} \right)^2 + \left(\frac{\Sigma_{\Phi_{bu}}}{\Phi_{bu}} \right)^2 + \left(\frac{\Sigma_{\varepsilon_{bu}}}{\varepsilon_{bu}} \right)^2 \right)} \quad (\text{B.10})$$

$$\Sigma_B = \pm B \sqrt{\frac{a_{bu}^2 N_{bu} + \phi^2 a_{car}^2 N_{car}}{(a_{bu} N_{bu} - \phi a_{car} N_{car})^2} + \left(\frac{\Sigma_{T_{bu}}}{T_{bu}} \right)^2 + \left(\frac{\Sigma_{\Phi_{bu}}}{\Phi_{bu}} \right)^2 + \left(\frac{\Sigma_{\varepsilon_{bu}}}{\varepsilon_{bu}} \right)^2} \quad (\text{B.11})$$

So, the uncertainty Σ_{bu} , related to the double differential cross section, was estimated via the following formula:

$$\Sigma_{bu} = \pm \left(\frac{d^2 \sigma_{bu}}{d\Omega_\alpha d\Omega_d} \right)_{lab} \sqrt{\frac{a_{bu}^2 N_{bu} + a_{car}^2 \phi^2 N_{car}}{(a_{bu} N_{bu} - a_{car} \phi N_{car})^2} + \left(\frac{\Sigma_{T_{bu}}}{T_{bu}} \right)^2 + \left(\frac{\Sigma_{\Phi_{bu}}}{\Phi_{bu}} \right)^2 + \left(\frac{\Sigma_{\varepsilon_{bu}}}{\varepsilon_{bu}} \right)^2} \quad (\text{B.12})$$

where $\Sigma_{T_{bu}}$, $\Sigma_{\Phi_{bu}}$ and $\Sigma_{\varepsilon_{bu}}$ are the uncertainties related with the scattering centers, the flux and the total efficiency respectively. The error at the determination of the breakup double differential cross section includes the statistical error, the error due to the carbon background subtraction, errors due to the target thickness, the uncertainty at the beam flux measurement as well as the efficiency determination via the simulation program.

Appendix C

Computer codes

C.1 Routines in C language: C.M. to Lab converter

The following programs, in C language, were used in the data analysis in order to convert the differential cross sections from the center of mass frame to the laboratory frame. The first code was used for the data associated with the first solution while the second one for the data associated with the second solution. The programs follow the prescription of Ref. [176].

1st solution

```
# include<stdio.h>
# include<stdlib.h>
# include<math.h>
int main(void){
    int i; // Definition of an integer number required in the "For" loop.//
    float b[16],y[16],E[16];
    double thetalab[16],sigmalab[16],thetalabrad[16];
    double thetacm,sigmacm,M1,M2,M3,M4,Q,ET,E1;
    double A,B,C,D,M,m1,m2,m3,m4,e3;
    double gamma,Ecm,VCM,u,tantheta[16];

    printf("\n");
    printf("\n");
    printf("*****\n");
```

```

printf("*****\n");
printf("*_Ioannina_2013,*****\n");
printf("*_CM2Lab_converter*****\n");
printf("*****\n");
printf("*****\n");
printf("\n");
printf("\n");

printf("Please enter the mass of the projectile in amu:\n");
scanf("%lf", &m1); //Read the number and store it in the variable m1.
printf("\n");
printf("Please enter the mass of the target in amu:\n");
scanf("%lf", &m2); //Read the number and store it in the variable m2.
printf("\n");
printf("Please enter the mass of the light product in amu:\n");
scanf("%lf", &m3); //Read the number and store it in the variable m3.
printf("\n");
printf("Please enter the mass of the heavy product in amu:\n");
scanf("%lf", &m4); //Read the number and store it in the variable m4.
printf("\n");
printf("Please enter the energy of the reaction in MeV:\n");
scanf("%lf", &E1); //Read the number and store it in the variable E1.

M1=931.478*m1; //Convert the mass from amu to MeV/c^2.
M2=931.478*m2; //Convert the mass from amu to MeV/c^2.
M3=931.478*m3; //Convert the mass from amu to MeV/c^2.
M4=931.478*m4; //Convert the mass from amu to MeV/c^2.
Q=M1+M2-M3-M4; //Calculate the Q-value of the reaction.
//Q=0.00;
ET=E1+Q;
M=(M1+M2)*(M3+M4);
A=(M1*M4*(E1/ET))/M;
B=(M1*M3*(E1/ET))/M;

```

```

C=(M2*M3*(1+(M1*Q/(M2*ET))))/M;
D=(M2*M4*(1+(M1*Q/(M2*ET))))/M;

printf("\n");
printf("\n");

struct data{// Definition of a structure called data.//
    float thetacm;
    float sigmacm;
    }list[16];
// Each component of the structure is a (1x16) matrix. //

FILE *fp;// Definition of a pointer.//
fp=fopen("input.txt","r");

/*
Open the input.txt file and read it.
This file contains two columns corresponding
to thetacm and sigmacm.
*/

printf("\n");
printf("\n");
printf("\n");
printf("\n");
printf("\n");
    printf("%f\n",Q);

Ecm=(M2/(M1+M2))*E1;

VCM=(sqrt(2*M1*E1))/(M1+M2);

u=sqrt((2/(M3+M4))*(M4/M3)*(Ecm+Q));

gamma=(VCM/u);

```

```

printf("thetaLAB.....thetaCM.....sigmaLAB.....sigmaCM\n");

for(i=0;i<16;i++){
// Definition of a "For" loop which is repeated 16 times. //

fscanf(fp,"%f%f",&list[i].thetacm,&list[i].sigmacm);
// Scan the txt file and fill the matrices. //

b[i]=list[i].thetacm;
// Store each value of list.thetacm matrix to the b matrix. //

y[i]=(3.14159*b[i])/(180.);
// Convert thetacm from degrees to rad. //

E[i]=B+D+(2*(sqrt(A*C))*cos(y[i]));

printf("\n");

tantheta[i]=sin(y[i])/(cos(y[i])+gamma);
thetalabrad[i]=atan(tantheta[i]);
// Calculate thetalab in rad. //

thetalab[i]=(thetalabrad[i]*180)/3.14159;
// Convert the thetalab from rad to degrees.//

printf("\n");
if(thetalab[i]<0){
sigmalab[i]=list[i].sigmacm*(gamma*(cos(thetalabrad[i]))+
(sqrt(1-(gamma*gamma*(pow(sin(thetalabrad[i]),2.))))))*
(gamma*(cos(thetalabrad[i]))+
(sqrt(1-(gamma*gamma*(pow(sin(thetalabrad[i]),2.)))))))/
(sqrt(1-(gamma*gamma*(pow(sin(thetalabrad[i]),2.)))));
// Evaluate the cross section in the lab system. //

```

```

printf(" %4.2f_ %15.2f_ %15.4f_ %15.6f\n",
(180+thetalab[i]), list[i].thetacm, sigmalab[i], list[i].sigmacm);
// Print the thetalab, thetacm, sigmalab and sigmacm values respectively.//
}

else{
sigmalab[i]=list[i].sigmacm*(gamma*(cos(thetalabrad[i]))+
(sqrt(1-(gamma*gamma*(pow(sin(thetalabrad[i]),2.)))))))*
(gamma*(cos(thetalabrad[i]))+
(sqrt(1-(gamma*gamma*(pow(sin(thetalabrad[i]),2.)))))))/
(sqrt(1-(gamma*gamma*(pow(sin(thetalabrad[i]),2.))))));
// Evaluate the cross section in the lab system. //
printf(" %4.2f_ %15.2f_ %15.4f_ %15.6f\n",
thetalab[i], list[i].thetacm, sigmalab[i], list[i].sigmacm);
// Print the thetalab, thetacm, sigmalab and sigmacm values respectively.//
}

} // End of the "For" loop. //

fclose(fp);
return 0;
}

```

2nd solution

```

# include<stdio.h>
# include<stdlib.h>
# include<math.h>
int main(void){
    int i; // Definition of an integer number required in the "For" loop.//
    float b[16],y[16],E[16];
    double thetalab[16],sigmalab[16],thetalabrad[16];
    double thetacm,sigmacm,M1,M2,M3,M4,Q,ET,E1;
    double A,B,C,D,M,m1,m2,m3,m4,e3;
    double gamma,Ecm,VCM,u,tantheta[16];

```

```

printf("\n");
printf("\n");
printf("*****\n");
printf("*\n");
printf("*Ioannina 2013,\n");
printf("*CM2Lab converter\n");
printf("*\n");
printf("*****\n");
printf("\n");
printf("\n");

printf("Please enter the mass of the projectile in amu:\n");
scanf("%lf", &m1); //Read the number and store it in the variable m1.//
printf("\n");
printf("Please enter the mass of the target in amu:\n");
scanf("%lf", &m2); //Read the number and store it in the variable m2.//
printf("\n");
printf("Please enter the mass of the light product in amu:\n");
scanf("%lf", &m3); //Read the number and store it in the variable m3.//
printf("\n");
printf("Please enter the mass of the heavy product in amu:\n");
scanf("%lf", &m4); //Read the number and store it in the variable m4.//
printf("\n");
printf("Please enter the energy of the reaction in MeV: \n");
scanf("%lf", &E1); //Read the number and store it in the variable E1.//

M1=931.478*m1; //Convert the mass from amu to MeV/c^2.//
M2=931.478*m2; //Convert the mass from amu to MeV/c^2.//
M3=931.478*m3; //Convert the mass from amu to MeV/c^2.//
M4=931.478*m4; //Convert the mass from amu to MeV/c^2.//
Q=M1+M2-M3-M4; //Calculate the Q-value of the reaction.//
//Q=0.00;

```

```

ET=E1+Q;
M=(M1+M2)*(M3+M4);
A=(M1*M4*(E1/ET))/M;
B=(M1*M3*(E1/ET))/M;
C=(M2*M3*(1+(M1*Q/(M2*ET))))/M;
D=(M2*M4*(1+(M1*Q/(M2*ET))))/M;

printf("\n");
printf("\n");

struct data{// Definition of a structure called data.//
    float thetacm;
    float sigmacm;
    }list[16];
// Each component of the structure is a (1x16) matrix. //

FILE *fp;// Definition of a pointer.//
fp=fopen("input.txt","r");

/*
Open the input.txt file and read it.
This file contains two columns corresponding
to thetacm and sigmacm.
*/

printf("\n");
printf("\n");
printf("\n");
printf("\n");
printf("\n");
printf("%f\n",Q);

Ecm=(M2/(M1+M2))*E1;

VCM=(sqrt(2*M1*E1))/(M1+M2);

```

```

u=sqrt (( 2 / (M3+M4) ) * (M4/M3) * (Ecm+Q) );

gamma=(VCM/u);

printf("thetaLAB_____thetaCM_____sigmaLAB_____sigmaCM\n" );

    for (i=0;i<16;i++){
//  Definition of a "For" loop which is repeated 16 times.      //

        fscanf(fp,"%f%f", &list[i].thetacm, &list[i].sigmacm);
//  Scan the txt file and fill the matrices.                      //

        b[i]=list[i].thetacm;
//  Store each value of list.thetacm matrix to the b matrix. //

        y[i]=(3.14159*b[i])/(180.);
//  Convert thetacm from degrees to rad.                          //

        E[i]=B+D+(2*(sqrt(A*C))*cos(y[i]));

        printf("\n");

        tantheta[i]=sin(y[i])/(cos(y[i])+gamma);
        thetalabrad[i]=atan(tantheta[i]);
//  Calculate thetalab in rad. //

        thetalab[i]=(thetalabrad[i]*180)/3.14159;
//  Convert the thetalab from rad to degrees.//

        printf("\n");
        if(thetalab[i]<0){
signalab[i]=list[i].sigmacm*(gamma*(cos(thetalabrad[i]))-
(sqrt(1-(gamma*gamma*(pow(sin(thetalabrad[i]),2.))))))*
(gamma*(cos(thetalabrad[i]))-

```



```

(sqrt(1-(gamma*gamma*(pow(sin(thetalabrad[i]),2.))))) /
(sqrt(1-(gamma*gamma*(pow(sin(thetalabrad[i]),2.))))) ;
// Evaluate the cross section in the lab system. //

printf("%4.2f_ %15.2f_ %15.4f_ %15.6f\n",
(180+thetalab[i]), list[i].thetacm, sigmalab[i], list[i].sigmacm);
//Print the thetalab, thetacm, sigmalab and sigmacm values respectively.//
}

else{
sigmalab[i]=list[i].sigmacm*(gamma*(cos(thetalabrad[i]))-
(sqrt(1-(gamma*gamma*(pow(sin(thetalabrad[i]),2.))))) *
(gamma*(cos(thetalabrad[i]))-
(sqrt(1-(gamma*gamma*(pow(sin(thetalabrad[i]),2.))))) /
(sqrt(1-(gamma*gamma*(pow(sin(thetalabrad[i]),2.))))) );
// Evaluate the cross section in the lab system. //

printf("%4.2f_ %15.2f_ %15.4f_ %15.6f\n",
thetalab[i], list[i].thetacm, sigmalab[i], list[i].sigmacm);
// Print the thetalab, thetacm, sigmalab and sigmacm values respectively.//
}

} // End of the "For" loop. //

fclose(fp);
return 0;
}

```

C.2 Routines in C language: Lab to C.M. converter

The following programs, in C language, were used in the data analysis in order to convert the differential cross sections from the laboratory to the center of mass frame. The first code was used for the data associated with the first solution while the second one for the data

associated with the second solution. The programs follow the prescription of Ref. [176].

1st solution

```
# include<stdio.h>
# include<stdlib.h>
# include<math.h>
int main(void){
int i; //Definition of an integer number required in the "For" loop.//
float b[16],y[16],E[16];
double thetalab,sigmalab,thetalabrad[16],thetacmdeg[16];
double thetacm[16],sigmacm[16],M1,M2,M3,M4,Q,ET,E1;
double A,B,C,D,M,m1,m2,m3,m4,e3;
double gamma,Ecm,VCM,u,tantheta[16];

printf("\n");
printf("\n");
printf("*****\n");
printf("*\n");
printf("*_Ioannina_2013,\n");
printf("*_Lab2CM_converter_\n");
printf("*\n");
printf("*****\n");
printf("\n");
printf("\n");

printf("_Please_enter_the_mass_of_the_projectile_in_amu:\n");
scanf("%lf",&m1); //Read the number and store it in the variable m1.//
printf("\n");
printf("_Please_enter_the_mass_of_the_target_in_amu:\n");
scanf("%lf",&m2); //Read the number and store it in the variable m2.//
printf("\n");
printf("_Please_enter_the_mass_of_the_light_product_in_amu:\n");
scanf("%lf",&m3); //Read the number and store it in the variable m3.//
```

```

printf("\n");
printf("Please enter the mass of the heavy product in amu:\n");
scanf("%lf", &m4); //Read the number and store it in the variable m4.//
printf("\n");
printf("Please enter the energy of the reaction in MeV:\n");
scanf("%lf", &E1); //Read the number and store it in the variable E1.//

M1=931.478*m1; //Convert the mass from amu to MeV/c^2.//
M2=931.478*m2; //Convert the mass from amu to MeV/c^2.//
M3=931.478*m3; //Convert the mass from amu to MeV/c^2.//
M4=931.478*m4; //Convert the mass from amu to MeV/c^2.//
Q=M1+M2-M3-M4; //Calculate the Q-value of the reaction.//
//Q=0.0;
ET=E1+Q;
M=(M1+M2)*(M3+M4);
A=(M1*M4*(E1/ET))/M;
B=(M1*M3*(E1/ET))/M;
C=(M2*M3*(1+(M1*Q/(M2*ET))))/M;
D=(M2*M4*(1+(M1*Q/(M2*ET))))/M;

printf("\n");
printf("\n");

struct data{ // Definition of a structure called data.//
    float thetalab;
    float sigmalab;
}list[16]; //Each component of the structure is a (1x16) matrix.//

FILE *fp; // Definition of a pointer.//
fp=fopen("input.txt","r"); // Open the input file and read it.//
/*
The input file contains two columns corresponding
to thetalab and sigmalab

```

```

*/

printf("\n");
printf("\n");
printf("\n");
printf("\n");
printf("\n");
    printf("%f\n",Q);

Ecm=(M2/(M1+M2))*E1;

VCM=(sqrt(2*M1*E1))/(M1+M2);

u=sqrt((2/(M3+M4))*(M4/M3)*(Ecm+Q));

gamma=(VCM/u);

printf("thetaLAB_____thetaCM_____sigmaLAB_____sigmaCM\n");

    for(i=0;i<16;i++){
//Definition of a "For" loop which is repeated 16 times.//

        fscanf(fp,"%f%f", &list[i].thetalab, &list[i].sigmalab);
//Scan the input file and fill the matrices.//

        b[i]=list[i].thetalab;
//Store each value of list.thetalab matrix to the b matrix. //

        y[i]=(3.14159*b[i])/(180.);
//    Convert thetalab from degrees to radians.//

        thetacm[i]=y[i]+asin(gamma*sin(y[i]));

        thetacmdeg[i]=(180.*thetacm[i])/(3.14159);

```

```

        printf("\n");
        if(b[i]<0){

sigmacm[i]=list[i].sigmalab/((gamma*(cos(y[i]))+
(sqrt(1-(gamma*gamma*(pow(sin(y[i]),2.)))))*(gamma*(cos(y[i]))+
(sqrt(1-(gamma*gamma*(pow(sin(y[i]),2.)))))/
(sqrt(1-(gamma*gamma*(pow(sin(y[i]),2.)))))
// Evaluate the cross section in the C.M. system.//

printf("%4.2f_ %15.2f_ %15.4f_ %15.6f\n",
(180+b[i]), thetacmdeg[i], list[i].sigmalab, sigmacm[i]);
//Print the thetalab, thetacm, sigmalab and sigmacm values respectively.//
        }

        else{

sigmacm[i]=list[i].sigmalab/((gamma*(cos(y[i]))+
(sqrt(1-(gamma*gamma*(pow(sin(y[i]),2.)))))*(gamma*(cos(y[i]))+
(sqrt(1-(gamma*gamma*(pow(sin(y[i]),2.)))))/
(sqrt(1-(gamma*gamma*(pow(sin(y[i]),2.)))))
// Evaluate the cross section in the C.M. system. //

printf("%4.2f_ %15.2f_ %15.4f_ %15.6f\n",
b[i], thetacmdeg[i], list[i].sigmalab, sigmacm[i]);
//Print the thetalab, thetacm, sigmalab and sigmacm values respectively.//
        }

    }
// End of the "For" loop. //

    fclose(fp);
    return 0;
}

```

2nd solution

```

# include<stdio.h>
# include<stdlib.h>
# include<math.h>
int main(void){
int i; // Definition of an integer number required in the "For" loop. //
float b[16],y[16],E[16];
double thetalab,sigmalab,thetalabrad[16],thetacmdeg[16];
double thetacm[16],sigmacm[16],M1,M2,M3,M4,Q,ET,E1;
double A,B,C,D,M,m1,m2,m3,m4,e3;
double gamma,Ecm,VCM,u,tantheta[16];

printf("\n");
printf("\n");
printf("*****\n");
printf("*_____*\n");
printf("*_Ioannina_2013,_____*\n");
printf("*_Lab2CM_converter_____*\n");
printf("*_____*\n");
printf("*****\n");
printf("\n");
printf("\n");

printf("_Please_enter_the_mass_of_the_projectile_in_amu:\n");
scanf("%lf",&m1); //Read the number and store it in the variable m1.//
printf("\n");
printf("_Please_enter_the_mass_of_the_target_in_amu:\n");
scanf("%lf",&m2); //Read the number and store it in the variable m2.//
printf("\n");
printf("_Please_enter_the_mass_of_the_light_product_in_amu:\n");
scanf("%lf",&m3); //Read the number and store it in the variable m3.//
printf("\n");
printf("_Please_enter_the_mass_of_the_heavy_product_in_amu:\n");
scanf("%lf",&m4); //Read the number and store it in the variable m4.//
printf("\n");
printf("_Please_enter_the_energy_of_the_reaction_in_MeV: \n");

```

```

scanf("%lf", &E1); //Read the number and store it in the variable E1. //

M1=931.478*m1; //Convert the mass from amu to MeV/c^2.//
M2=931.478*m2; //Convert the mass from amu to MeV/c^2.//
M3=931.478*m3; //Convert the mass from amu to MeV/c^2.//
M4=931.478*m4; //Convert the mass from amu to MeV/c^2.//
Q=M1+M2-M3-M4; //Calculate the Q-value of the reaction.//
// Q=0.0;
    ET=E1+Q;
    M=(M1+M2)*(M3+M4);
    A=(M1*M4*(E1/ET))/M;
    B=(M1*M3*(E1/ET))/M;
    C=(M2*M3*(1+(M1*Q/(M2*ET))))/M;
    D=(M2*M4*(1+(M1*Q/(M2*ET))))/M;

printf("\n");
printf("\n");

struct data{ // Definition of a structure called data.//
    float thetalab;
    float sigmalab;
    }list[16];
// Each component of the structure is a (1x16) matrix. //

FILE *fp; // Definition of a pointer.//
fp=fopen("input.txt", "r");

/*
Open the input file and read it.
This file contains two columns corresponding
to thetalab and sigmalab.
*/

printf("\n");
printf("\n");
printf("\n");

```

```

printf("\n");
printf("\n");
printf("%f\n",Q);

Ecm=(M2/(M1+M2))*E1;

VCM=(sqrt(2*M1*E1))/(M1+M2);

u=sqrt((2/(M3+M4))*(M4/M3)*(Ecm+Q));

gamma=(VCM/u);

printf("thetaLAB_____thetaCM_____sigmaLAB_____sigmaCM\n");

for(i=0;i<16;i++){
// Definition of a "For" loop which is repeated 16 times. //

fscanf(fp,"%f%f",&list[i].thetalab,&list[i].sigmalab);
// Scan the txt file and fill the matrices. //

b[i]=list[i].thetalab;
// Store each value of list.thetalab matrix to the b matrix. //

y[i]=(3.14159*b[i])/(180.);
// Convert thetalab from degrees to radians. //

thetacm[i]=3.14159+y[i]-asin(gamma*sin(y[i]));

thetacmdeg[i]=(180.*thetacm[i])/(3.14159);

printf("\n");
if(b[i]<0){

sigmacm[i]=list[i].sigmalab/((gamma*(cos(y[i]))-
(sqrt(1-(gamma*gamma*(pow(sin(y[i]),2.))))))*(gamma*(cos(y[i]))-

```



```

(sqrt(1-(gamma*gamma*(pow(sin(y[i]),2.))))) /
(sqrt(1-(gamma*gamma*(pow(sin(y[i]),2.))))) ;
// Evaluate the cross section in the C.M. system. //

printf("%4.2f_ %15.2f_ %15.4f_ %15.6f\n",
(180+b[i]), thetacmdeg[i], list[i].signalab, sigmacm[i]);
//Print the thetalab, thetacm, signalab and sigmacm values respectively.//
}

else{
sigmacm[i]=list[i].signalab / ((gamma*(cos(y[i])) -
(sqrt(1-(gamma*gamma*(pow(sin(y[i]),2.))))) * (gamma*(cos(y[i])) -
(sqrt(1-(gamma*gamma*(pow(sin(y[i]),2.))))) /
(sqrt(1-(gamma*gamma*(pow(sin(y[i]),2.))))) );
//Evaluate the cross section in the C.M. system. //

printf("%4.2f_ %15.2f_ %15.4f_ %15.6f\n",
b[i], thetacmdeg[i], list[i].signalab, sigmacm[i]);
//Print the thetalab, thetacm, signalab and sigmacm values respectively.//
}

} // End of the "For" loop. //

fclose(fp);
return 0;
}

```


Appendix D

Tabulated cross sections

D.1 Elastic scattering data

Table D.1: *Elastic scattering differential cross sections in the center of mass frame $(d\sigma/d\Omega)_{c.m.}$ for ${}^6\text{Li} + p$ at 29 MeV (4.83 MeV/u).*

$\theta_{c.m.}$ (deg)	$(d\sigma/d\Omega)_{c.m.}$ (mb/sr)	Error (mb/sr)
19.39	1188.40	94.12
23.03	759.73	61.75
26.73	497.18	41.75
30.50	342.40	29.81
34.37	338.13	29.13
38.35	299.95	25.98
42.47	296.25	25.45
46.77	227.92	20.13
51.30	208.59	18.48
56.12	169.15	15.34
61.35	110.06	10.68
65.94	90.29	9.00
77.67	83.13	6.42
86.35	66.45	5.43
88.05	63.03	5.18
89.65	60.51	5.01
91.25	64.86	5.33

92.90	55.25	4.61
94.55	62.72	5.17
96.15	58.56	4.87
97.85	60.81	5.02
102.80	64.89	5.34
104.45	65.68	5.39
106.15	51.68	4.35
107.85	56.43	4.70
114.61	49.15	3.71
116.70	54.22	4.51
118.55	58.20	4.80
120.45	42.73	3.65
122.35	49.13	4.13
123.53	49.70	3.84
124.25	60.16	4.94
126.25	53.49	4.42
129.33	55.53	3.01
134.15	51.33	2.81
138.38	54.09	2.96
142.20	56.94	3.13
145.73	56.59	3.12
149.03	58.52	3.26
152.15	55.16	3.07
155.13	56.32	4.34
158.00	61.06	4.73
160.77	67.75	5.28
163.47	54.12	4.31

Table D.2: *Elastic scattering differential cross sections in the center of mass frame $(d\sigma/d\Omega)_{c.m.}$ for ${}^6\text{Li} + p$ at 25 MeV (4.17 MeV/u).*

$\theta_{c.m.}$ (deg)	$(d\sigma/d\Omega)_{c.m.}$ (mb/sr)	Error (mb/sr)
19.39	1414.56	114.49
23.03	611.18	54.37

26.73	357.24	34.94
30.50	220.32	23.95
34.37	156.11	18.27
38.35	148.55	17.05
42.47	111.05	13.40
46.77	126.17	14.11
51.30	115.65	12.85
56.12	96.23	10.97
61.35	95.16	10.60
67.17	66.76	8.00
73.97	66.23	7.50
78.55	54.05	5.16
82.35	48.03	4.73
86.15	43.13	4.36
89.95	44.04	4.45
93.75	44.59	4.50
97.55	51.91	5.08
101.35	49.20	4.82
105.25	46.99	4.66
109.25	47.48	4.71
113.25	48.21	4.75
117.45	48.46	4.73
121.85	41.91	4.21
126.35	38.31	3.89
123.53	53.39	5.07
129.33	44.86	3.14
134.15	43.23	3.18
138.38	43.72	3.30
142.20	46.72	3.56
145.73	47.28	3.68
149.03	48.00	3.78
152.15	48.95	4.19
155.13	42.51	5.84
158.00	44.55	7.14
160.77	59.62	9.98

163.47	51.37	11.14
167.67	43.53	7.10

Table D.3: *Elastic scattering differential cross sections in the center of mass frame $(d\sigma/d\Omega)_{c.m.}$ for ${}^6\text{Li} + p$ at 20 MeV (3.33 MeV/u).*

$\theta_{c.m.}$ (deg)	$(d\sigma/d\Omega)_{c.m.}$ (mb/sr)	Error (mb/sr)
19.39	2426.84	181.31
23.03	1039.97	79.47
26.73	585.96	46.10
30.50	337.03	27.70
34.37	265.53	22.32
38.35	199.14	17.26
42.47	172.11	15.10
46.77	135.76	12.22
51.30	142.14	12.54
56.12	129.00	11.39
61.35	109.32	9.75
67.17	92.31	8.29
73.97	75.33	6.80
82.55	73.82	5.62
87.35	73.95	5.64
92.05	76.68	5.84
96.75	67.01	5.14
101.55	55.88	4.30
106.45	55.09	4.25
111.45	51.69	4.00
116.60	48.69	3.77
122.00	39.59	3.10
128.54	43.32	3.16
134.08	41.98	2.94
138.38	40.45	2.40
142.20	39.60	2.40
145.73	41.15	2.53

149.03	36.86	3.27
152.15	35.49	3.31

Table D.4: *Elastic scattering differential cross sections in the center of mass frame $(d\sigma/d\Omega)_{c.m.}$ for ${}^6\text{Li} + p$ at 16 MeV (2.67 MeV/u).*

$\theta_{c.m.}$ (deg)	$(d\sigma/d\Omega)_{c.m.}$ (mb/sr)	Error (mb/sr)
19.39	2965.09	222.35
23.03	1533.34	117.22
26.73	828.83	65.29
30.50	575.61	46.42
34.37	388.97	32.39
38.35	332.13	27.93
42.47	237.80	20.74
46.77	192.31	17.17
51.30	153.59	14.02
56.12	135.09	12.45
61.35	112.44	10.54
67.17	94.85	8.97
73.97	81.05	7.61
77.00	82.60	6.25
80.05	81.27	6.14
83.05	77.20	5.84
86.00	74.13	5.63
88.95	71.49	5.45
91.95	71.00	5.41
94.90	68.16	5.20
97.90	64.34	4.92
100.90	59.04	4.52
103.90	55.69	4.27
107.00	57.10	4.38
110.10	52.66	4.06
113.30	49.54	3.83
116.60	51.03	3.94

119.90	43.51	3.38
123.40	40.92	3.19
127.00	38.36	2.30
130.80	35.07	2.74
134.53	37.81	3.14
138.79	35.54	3.04
142.20	36.57	2.92
145.73	37.97	3.03
149.03	37.23	2.98

D.2 Breakup data

Table D.5: *Breakup differential cross sections in the center of mass frame $(d\sigma/d\Omega)_{c.m.}$ for ${}^6\text{Li} + p$ at 29 MeV (4.83 MeV/u).*

$\theta_{c.m.}$ (deg)	$(d\sigma/d\Omega)_{c.m.}$ (mb/sr)	Error (mb/sr)
15.0	27.18	9.18
19.0	24.33	5.31
22.0	24.70	4.89
24.0	32.79	6.07
27.5	30.88	5.40
31.5	31.43	5.45
34.0	33.64	5.37
37.5	30.78	5.22
40.5	32.97	5.24
44.0	33.49	5.30
48.0	33.12	5.31
51.5	30.23	4.93
56.0	31.39	4.97
60.0	26.89	4.54
64.0	40.00	6.77
70.0	39.38	6.79
76.5	38.03	7.20

86.0 23.24 5.00

Table D.6: *Breakup differential cross sections in the center of mass frame $(d\sigma/d\Omega)_{c.m.}$ for ${}^6\text{Li} + p$ at 25 MeV (4.17 MeV/u).*

$\theta_{c.m.}$ (deg)	$(d\sigma/d\Omega)_{c.m.}$ (mb/sr)	Error (mb/sr)
16.5	18.55	6.88
19.6	16.31	3.48
22.9	13.61	2.48
25.9	13.18	2.24
29.1	18.39	3.14
32.3	23.86	3.94
35.7	23.31	3.58
39.1	24.90	3.96
42.5	23.98	3.85
46.1	20.33	3.95
50.1	24.17	4.60
54.4	16.26	4.11
59.0	24.20	3.91
63.8	19.49	3.60
69.5	22.65	3.86
76.3	19.44	4.43
85.5	12.89	2.87